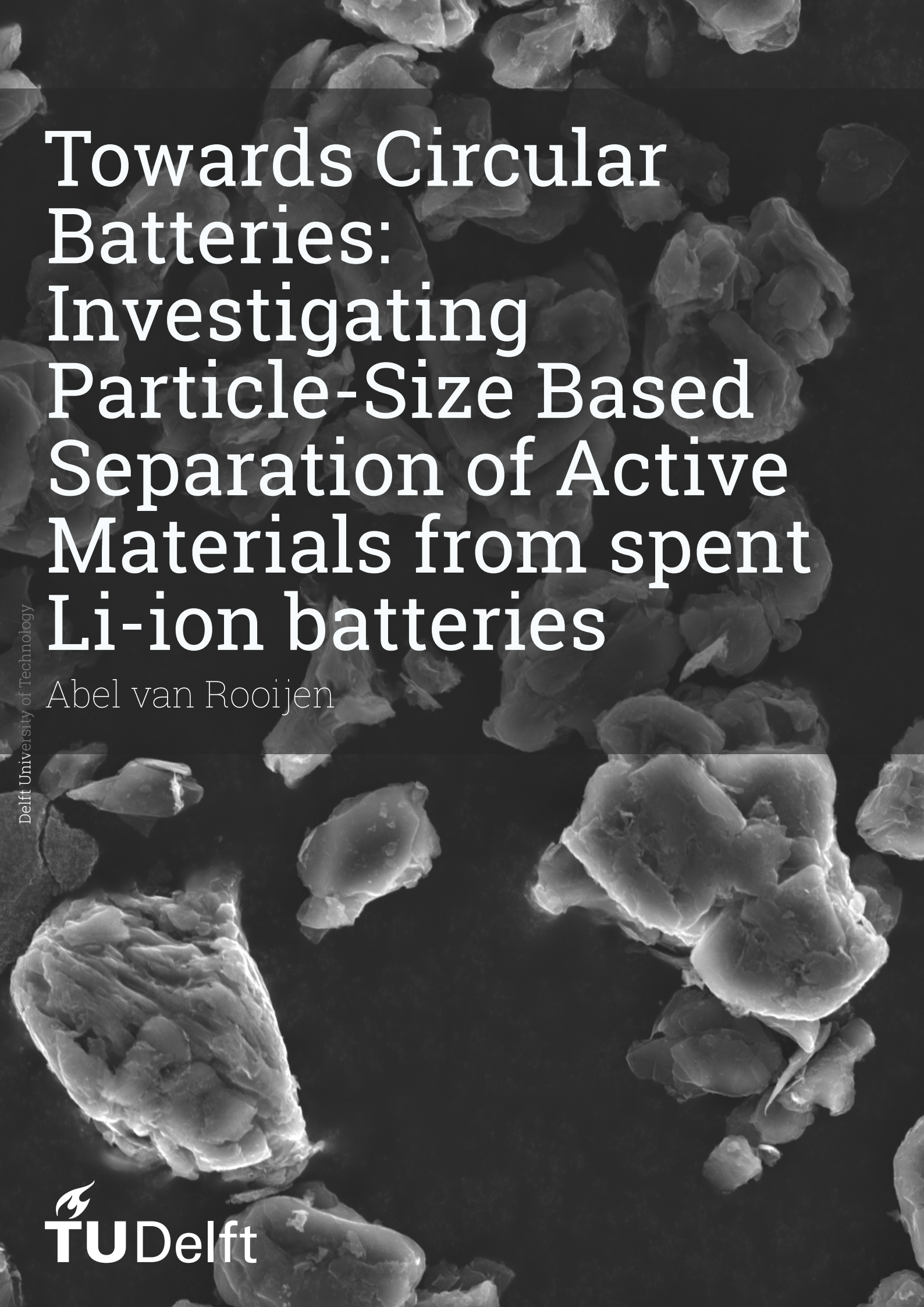

Towards Circular Batteries: Investigating Particle-Size Based Separation of Active Materials from spent Li-ion batteries

Abel van Rooijen

Delft University of Technology

TU Delft

Towards Circular Batteries: Investigating Particle-Size Based Separation of Active Materials from spent Li-ion batteries

by

Abel van Rooijen

to obtain the degree of Master of Science
at the Delft University of Technology,
to be defended publicly on Thursday March 7, 2024 at 13:30 PM.

Student number:	4712390
Project Duration:	February, 2023 - March, 2024
Faculty:	Faculty of Mechanical, Maritime and Materials Engineering, Delft
Thesis Committee:	Lorenzo Botto, TU Delft, supervisor
	Shoshan Abrahami, TU Delft
	Wiebren de Jong, TU Delft

Cover:	SEM image of Graphite from a commercial Li-ion battery
Style:	TU Delft Report Style

TU Delft

Acknowledgement

For a year, I dipped myself into the world of battery recycling, a completely unknown topic for me at the start of the project. I would like to thank Lorenzo Botto, my daily supervisor, who gave me the chance to work on this exciting project and the freedom to be creative and come up with new ideas. I am grateful for his valuable advice and the insightful discussions we shared. Lorenzo connected me to many people, all experts on their projects and essential for different parts of my research. By inviting me to meetings of the e4Batteryplatform of TU Delft, he allowed me to discuss the hot topical issues of battery recycling with many people from diverse academic disciplines. Thanks to these talks and discussions, I felt really involved in this project, which motivated me for this thesis.

From Lorenzo's research group, I want to thank Heng. He helped me understand the theory of sedimentation and was always ready to help me with questions and give feedback on my work. I have to thank Suriya for his practical help in the lab. He gave me good advice for my experimental setup and taught me how to do experimental research. I also want to thank Joep from Materials Science Engineering for conducting the most exciting part of the experiments, disassembling a real battery; performing these experiments brightened my view of all that I had read about the months before about batteries and gave me a better practical understanding of the project. I want to thank Luis, who helped me conduct exciting research by doing TGA experiments. He was always very interested in my work.

I want to thank the 'EFPT Legends' Jap, Dieter, and Jeroen for creating the most memorable moments throughout my Master's program. Together, we shared coffee and lunch breaks and unwound with our own 'Vrijmibo's' after challenging weeks of thesis work. Lastly, I want to thank my parents and my girlfriend for their never-ending support: this applies not only to the thesis before you but to my entire study at the TU Delft.

Abel van Rooijen
Delft, February 2024

Abstract

With the enormous growth of portable electronics and the market expansion of electric vehicles, the demand for lithium-ion batteries is increasing enormously. To meet this demand, efficient recovery of battery components becomes crucial. Graphite, the material of choice for lithium-ion battery anodes, faces significant supply risks as current recycling technologies primarily focus on recovering economically valuable metal components like cobalt and nickel. Therefore, the effective separation of graphite from lithium-ion batteries is essential for recycling and reusing anode materials. The key to the direct recycling of graphite is the separation of the finest material fractions of Li-ion batteries: the anode and cathode. This work tests a circular battery manufacturing principle based on the idea that the anode and cathode could be designed to have a difference in particle size to allow easy separation by centrifugation.

We analysed the particle sizes of anode and cathode material obtained from a spent Li-ion battery. A shift in particle size distributions is observed by grinding the materials, significantly reducing the particle sizes. We calculated the velocity distributions using Stokes' formula for the settling velocity of spherical particles in dilute suspensions from these size distributions. Combining the velocity distributions for the anode and cathode showed the overlap of the velocities. A combination of milled and unmilled material shows the smallest overlap between the velocity distributions and, therefore, the largest difference in sedimentation velocity and the highest theoretical separation.

We measured the sedimentation of anode and cathode particles in water optically using a light source. A camera tracks the moving front of the dilute suspensions over time. Experiments of different milled samples for various concentrations show insights into the anode and cathode sedimentation behaviour. Results show that increasing concentration significantly reduces sedimentation velocities for the anode material. These results deviate from what would be expected from the hindered settling of dilute suspension. A significant velocity reduction is measured for the milled anode and cathode, therefore showing the potential for separation if the materials have a marked difference in size.

In this thesis, a novel method is developed for characterising the sediment structure of the mixed active materials. By freezing sedimented suspensions, sample layers are horizontally cut off to look for the spreading of the different material components through the sediment. A combination of characterisation methods offers information about the anode and cathode fractions through the sediment layers. Significant differences between the sediment's top and bottom layers regarding morphology, elemental components and thermal stability are observed.

The results show the potential for circular batteries in the future, where centrifugation can play a vital role in separating the electrode materials if they have a marked size difference.

Contents

List of Figures

List of Tables

Nomenclature

Abbreviations

Abbreviation	Definition
Al	Aluminum
BM	Black mass
CB	Carbon black
CMC	Carboxymethylcellulose
Co	Cobalt
Cu	Copper
DMC	Dimethyl carbonate
EC	Ethylene carbonate
EG	Ethylene Glycol
EU	European Union
EV	Electric vehicle
ICP	Inductively Coupled Plasma
LCO	Lithium cobalt oxides ($LiCoO_2$)
LFP	Lithium iron phosphate ($LiFePO_4$)
LIB	Lithium-ion battery
Li	Lithium
LMO	Lithium Metal Oxides: collective term for different chemistries at the cathode of battery
MLB	Masliyah-Lockett-Bassoon (equation used for sedimentation modeling)
Ni	Nickel
NMC	Lithium nickel manganese cobalt oxides ($LiNiMnCoO_2$)
NMP	N-methylpyrrolidon
PE	Polyethylene
PP	Polypropylene
PSD	Particle Size Distribution
PVDF	Polyvinylidene fluoride
RZ	Richardson-Zaki (equation used for sedimentation modelling)
SEI	Solid Electrolyte Interface
SBR	Styrene Butadiene Rubber
SEM	Scanning Electron Microscopy
TGA	Thermogravimetric Analysis
US	United States

Symbols

Symbol	Definition	Unit
d	Diameter of spherical particle	[m]
g	Gravitational acceleration	[m/s^2]
H_{sep}	Separation height	[m]
$T_{Cathode}$	Separation efficiency Cathode in supernatant	[-]
t_{thres}	Threshold particle sedimentation time	[s]
v_{cut}	Cut-off velocity	[m/s]

Symbol	Definition	Unit
v_p	Particle velocity	[m/s]
v_{thres}	Threshold particle velocity	[m/s]
v_f	Fluid velocity	[m/s]
μ	Dynamic viscosity of the fluid	[Pa · s]
ρ_p	Particle density	[kg/m^3]
ρ_f	Fluid density	[kg/m^3]
ρ_{susp}	Suspension density	[kg/m^3]
ϕ	Particle volume fraction	[-]
ϕ_f	Fluid volume fraction	[-]

1

Introduction

1.1. Motivation

With its significant potential to mitigate emissions and decarbonise energy supply chains, electrification has become a crucial strategy for achieving net-zero goals. Consequently, the number of battery-powered devices, particularly in the electric vehicle (EV) market, is experiencing rapid growth. Among the various battery types available, lithium-ion batteries (LIBs) have emerged as the preferred choice for most applications due to their high power and energy density.

The escalating global demand for the raw materials used in LIBs has further strained the already limited supply in recent years. Critical raw materials such as cobalt (Co), nickel (Ni), lithium (Li), and graphite have been included in the EU's list of critical raw materials, highlighting their high supply risks and economic significance [16]. Effective recycling strategies for lithium-ion batteries are essential to address the need for raw material reduction and promote environmental protection.

Graphite, which constitutes approximately 15-25 wt% of the total mass of LIBs, is one of the critical raw materials facing a significant supply risk. However, it may not receive the same media attention as lithium and metals like cobalt and nickel [67]. However, graphite remains the material of choice for the anode and will continue to be an essential component of LIBs in the foreseeable future [3].

Forecasts indicate that the demand for anode materials in LIBs is expected to grow exponentially by over 500% between 2018 and 2050 [34]. Without sufficient resources, this trajectory would lead to a nearly 2 million tons natural flake graphite deficit by 2030. Furthermore, the concentration of graphite production and processing in China, where almost 90% of worldwide anodic spherical graphite is produced, renders the EU and the US particularly vulnerable to supply chain disruptions.

Although efforts are being made by the EU and the US to establish their own graphite supply chains, there are currently no industrial processes in place to recover graphite from end-of-life LIBs [67].

1.2. Literature Review

1.2.1. Design and Composition of a Lithium-ion battery

A typical commercial lithium-ion battery nowadays comprises pouch cells in a package of modules covered by a metallic casing. The cell is tightly packed and consists of two electrodes, separated by a separator to prevent direct contact and electrolytes, as seen in more detail in Figure 1.1.

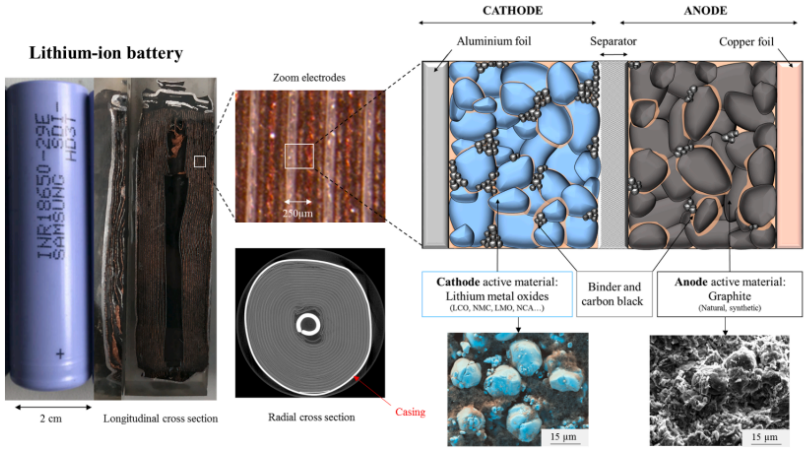

Figure 1.1: Schematic overview of the details of a cylindrical lithium-ion battery. On the left is an image of an 18.650 type LIB. On the right are SEM images of LCO with binder from the cathode and natural spheroidized graphite from the anode. Reproduced from Van der Bruggen et al., (2021) [63].

Electrolytes in a cell are mostly liquids that allow movement of the lithium ions between the electrodes. Lithium salts, $LiPF_6$, are dissolved in organic solvents, mostly carbonates like dimethyl carbonate (DMC) and ethylene carbonate (EC). The separator material that is commonly used is organic polymers, such as polyethylene (PE) and polypropylene (PP), to have a high ionic flow and mechanical stability.

The electrodes consist of a conductive foil coated with active particles. The conductive foils function as the current collectors to conduct the electrons between the electrodes [36, 38, 39]. The positive electrode, the cathode, comprises particles of lithium metal oxides (LMOs) deposited on an aluminium foil. Unlike the anode material, a wide range of cathode chemistries are used in commercial LIBs, depending on the battery application [61]. For example, $LiCoO_2$ (LCO) is primarily used in mobile applications, $LiFePO_4$ (LFP) for large, big scale storage applications and variable stoichiometry of $LiNiMnCoO_2$ (NMC) is applied in most EVs nowadays. These are the most used cathode chemistries for lithium-ion batteries nowadays.

Graphite is the active material for the anode, the negative electrode in lithium-ion batteries and is typically coated on a copper foil. In producing LIBs, spheroidized natural graphite or synthetic graphite particles, or a combination of both, are commonly utilised [3]. Graphite is the preferred active material for the anode in Li-ion batteries due to its excellent mechanical and thermal stability and favourable conductivity. Additionally, graphite offers advantages such as relatively low production costs, high energy density, and high power density [78].

An organic binder is used for proper adhesion of the active particles to the current collector and to hold together the active material particles. This binder acts as a glue between the active particles. In most commercialised batteries, polyvinylidene fluoride (PVDF) is the binder material of choice for both cathodes. However, in recent years, more aqueous-based binders have been processed as these have a lot of advantages over the use of PVDF [3, 12, 71]. The use of water as a solvent for the electrode material is environmentally more friendly, safer and cheaper in manufacturing the battery [12, 39, 71]. Aqueous-based binders already commercially used for the anode are Carboxymethylcellulose (CMC) and Styrene Butadiene Rubber (SBR). Conductive carbon black (CB) additives are often added to the electrodes and mixed with the active material before coating the electrode slurry on the foil. These small flakes function as a coating for the active material and enhance the electrical conductivity [36, 69]

The composition of a typical Li-ion battery varies depending on its shape and chemistry. Extensive analysis of different types of lithium-ion batteries (LIBs) from literature reveals that the active materials, lithium metal oxides (LMOs) and graphite, account for approximately 50 wt.% of the total mass of the battery, as shown in table 1.1 [9, 60, 68]. These numbers highlight the importance of active materials in the recycling process.

Material	Wt.%
External Casing	14-16
Graphite	17-22
LMOs	24-30
Cu foil	6-13
Al foil	3-13
Electrolytes	10-15
Separator	9-12

Table 1.1: Composition of a typical lithium-ion battery, showing the components with their respective weight fraction. The percentages may vary depending on the shape and chemistry of the battery.

1.2.2. Current recycling routes for Lithium-ion batteries

Due to its heterogeneous nature, recycling lithium-ion batteries is not a standardised process. Three recycling methods have been developed mainly for end-of-life Li-ion batteries, namely, pyrometallurgical, hydrometallurgical, and direct recycling.

The most common methods employed on large-scale, pyro- and hydrometallurgical processes are designed to recover valuable metals such as cobalt, nickel and copper. Although very robust, these processes have several drawbacks, like high energy requirements, chemical intensity and the inability to recover organic and carbon-based materials, like anodic graphite [68, 5, 70]. The efficiency of metallurgical processing depends on the concentration of anode and cathode material in the feed [63]. This feed needs to be controlled to minimise losses in recovering valuable metals.

Direct recycling is a recovery strategy that involves recovering the active materials (graphite and lithium-metal-oxides) of LIBs while preserving their morphology and chemical properties. This method makes up only 5% of the battery recycling market nowadays [1]. Physical and physico-chemical separation methods like froth flotation and centrifugation are gaining interest due to their advantages over well-known metallurgical processes. These methods aim to retrieve the separated active materials for reuse in battery electrodes or further downstream metallurgical processing by exploiting differences in physical/chemical properties between graphite (anode) and lithium metal oxides (cathode). This literature focuses on these direct recycling methods. Their state-of-the-art working principle and technical challenges are discussed later in this section.

Separating the finest material fraction before direct recycling and most metallurgical processing is necessary. This so-called *black mass* (BM) consists of a heterogeneous mixture of anode and cathode active materials. This black powder consists of micro-sized grains of mostly graphite and lithium metal oxides. To achieve higher material recovery rates, pre-treatment steps are necessary to separate other components and obtain the black mass of active materials. These steps are followed by methods for recycling the different battery materials.

Pre-tratment of batteries

The liberation of the different LIB components is necessary to enable efficient separation processes. Batteries can be treated in several subsequent pre-treatment steps to obtain liberated components. Figure 1.2. As shown, there are various ways to obtain the black mass (BM), and it consists of multiple steps to separate plastics, metallic foils and the binder material to end up with the finest material fraction, consisting of a powder anode/cathode material.

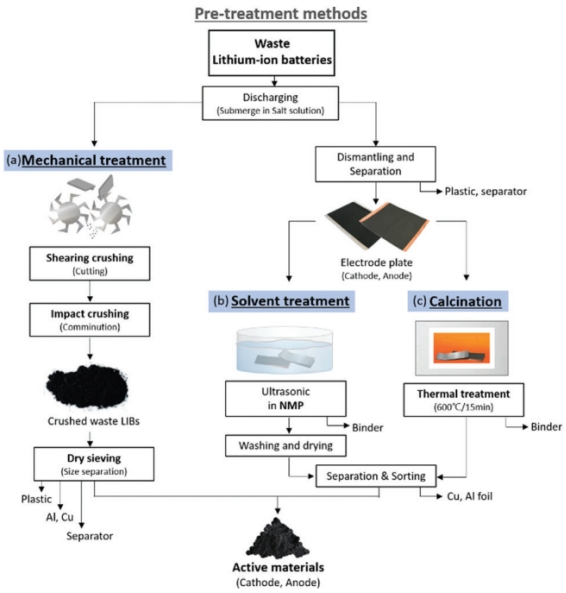

Figure 1.2: Overview of direct recycling routes to obtain different components of LIB and the black mass of cathode and anode material. Reproduced from Bae et al., (2021) [5].

Firstly, a spent battery must be discharged to dissipate all the remaining energy. This can be done by submerging the battery in a salt solution in water. A systematic approach, albeit time-consuming, involves dismantling the battery to segregate its various components, as illustrated on the right side of Figure 1.2. However, this process presents significant challenges when implemented on a large scale due to the labour-intensive nature of battery disassembly, which is also highly dependent on the specific battery shape and chemistry.

The binder must be eliminated from the electrode structure to facilitate the complete liberation of the active material from the electrodes. This can be achieved through the dissolution of the binder or by thermal treatment to decompose the material. Dissolving the binder is one way to liberate the active material from the electrode. Depending on the nature of the binder, this is done in N-methyl pyrrolidone (NMP), an organic and highly toxic solvent to dissolve PVDF binder material [6].

Another approach for the removal of the binder is thermal treatment. It represents a highly efficient approach, facilitating the separation of foils from the active material. Extensive studies documented in the literature [30, 42, 66] showed that the PVDF binder decomposes at temperatures ranging from 500 to 550 °C. CMC/SBR binder decomposes at temperatures around 350 °C by performing vacuum pyrolysis in an oxygen-free environment. Consequently, the binder transforms into low molecular weight species, enabling facile detachment of the active material from the foil.

In the case of incineration (in the presence of air), the evaporation of organic components such as electrolytes, separators, and binder gives rise to the release of toxic gases, including hydrogen fluoride (HF), hydrocarbons, nitrogen oxides, CO, and CO_2 [42]. To address this concern, an absorption mechanism is necessary to capture and eliminate these gases during electrode treatment in an air environment.

Instead of dismantling a battery, a more straightforward and scalable way is to perform mechanical treatment on the discharged batteries, shown as the left-side route of Figure 1.2. Comminution followed by size sieving of the LIB components separates the active particles of the anode and cathode (LMOs and graphite) from the coarser fractions (casing, foils and plastics). Mechanical processing uses cutting, hammer, or impact mills to induce impact and shear forces to remove the active particles from the foils [30].

Van der Bruggen et al., [65] showed that mechanical treatment and size sieving give a very high purity of active particles without residual Al and Cu foils, as seen in Figure 1.3. Due to the more ductile nature of these foils, they are rather deformed than comminuted in the crusher. However, due to the presence of the binder, only a small portion (5.1 wt.%) of the black mass is found in the finest fraction (< 63 μm), consisting of the liberated active material grains [64].

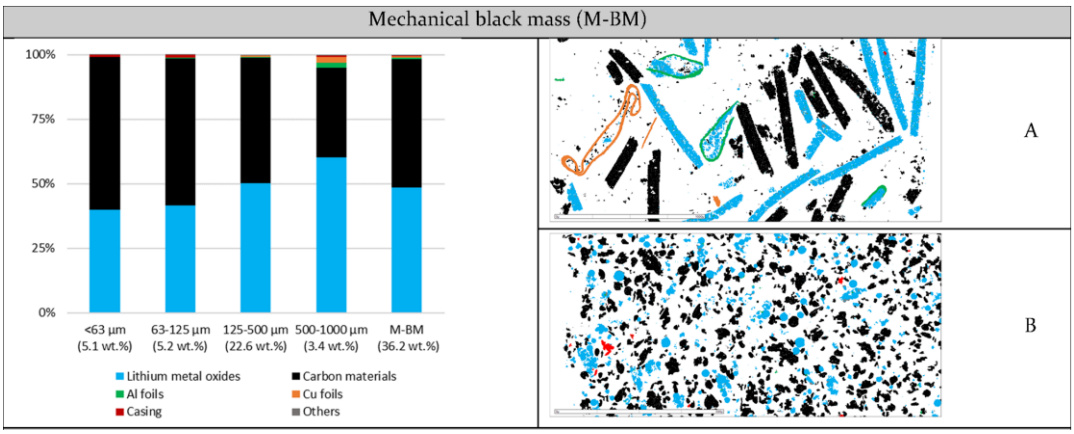

Figure 1.3: On the left: The black mass composition after mechanical treatment and size sieving, showing the material compounds in each size fraction. On the right: Processed Scanning Electron Images (SEM) of two sieved fractions. Picture A shows the 500 - 1000 μm fraction, and B shows the finest fraction (< 63 μm). Reproduced from Van der Bruggen et al., (2022) [65].

Combining mechanical- and thermal treatment techniques has demonstrated a high fraction of liberated active material in the black mass [30, 66]. Thermo-mechanical treatment on a LIB effectively liberates the anode and cathode material due to the effective decomposition of the binder by performing vacuum pyrolysis. Mechanical stressing and sieving resulted in 21 wt.% of the initial battery found in the smallest size fraction (<63 μm). Figure 1.4 shows that this fraction predominantly consists of the liberated graphite and lithium-metal-oxides.

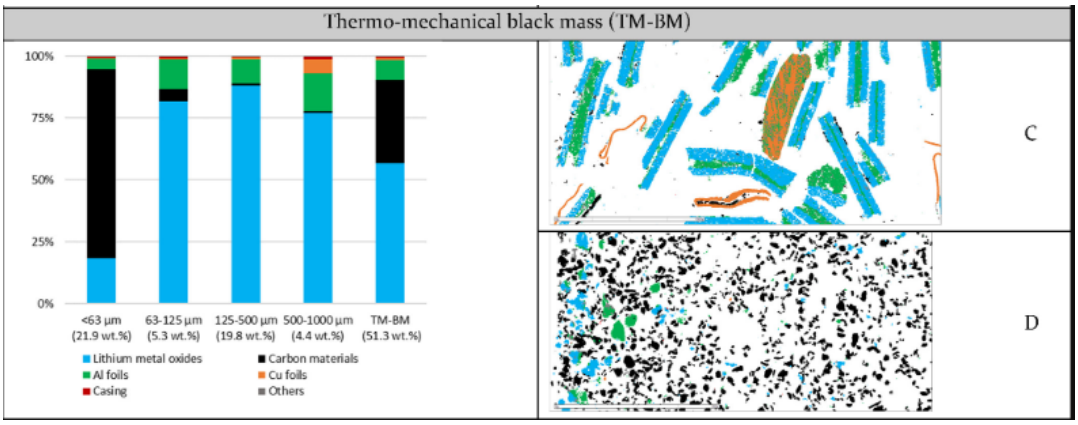

Figure 1.4: On the left: The black mass composition after thermal- and mechanical treatment, showing the material compounds in each size fraction. On the right: Processed Scanning Electron Images (SEM) of two sieved fractions. Picture A shows the 500 - 1000 μm fraction, and B shows the finest fraction (< 63 μm). Reproduced from Van der Bruggen et al., (2022) [65].

1.2.3. Froth flotation: separating the anode from the cathode

Ideally, the resulting black mass after pre-treatment consists of a mixture of liberated anode and cathode particles that can be recycled further. By separating the anode from the cathode, they can be directly reused for new battery electrodes, or the materials can be fed into further downstream metallurgical processes to recover the metals and the lithium.

Froth flotation is a promising method for separating graphite from the lithium metal oxides. It is a widely employed physicochemical separation method in various industries based on the differences in the wettability of particle surfaces. It has long been recognised as an effective technique for separating coal particles from coal waste impurities [44]. In recent years, froth flotation has also been utilised for obtaining high-grade metal products from lithium-ion batteries before undergoing further metallurgical separation processes [56, 76]. Another advantage of this approach is the simultaneous recovery of graphite particles as a product. It is a scalable method with relatively low energy consumption.

Froth flotation is based on wettability differences between two materials to separate them. Figure 1.5 shows the working principle. A mix of anode and cathode materials is suspended in a flotation tank containing water [56]. By dispensing air bubbles from the bottom of the tank, the rising air bubbles collect the hydrophobic material, while the hydrophilic particles remain dispersed in the water. In this way, the hydrophobic particles are collected at the top of the tank with the air bubbles, called the froth phase product. In contrast, the hydrophilic particles are collected at the bottom of the tank, the underflow product. As the lithium metal oxides are mostly hydrophilic and the graphite is hydrophobic, separating the two is theoretically possible.

Experimental studies on froth flotation showed remarkable recovery rates of 97 % graphite in the froth phase and 93 % lithium metal oxides in the underflow product [63].

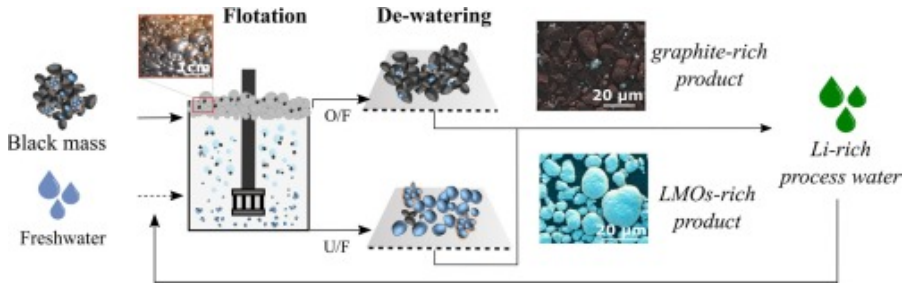

Figure 1.5: Simplified sketch of a froth flotation process. A water tank is used to mix the black mass feed. The hydrophobic particles will separate from the hydrophilic ones, ending in the overflow (O/F) and underflow (U/F) products, respectively. Scraping off the froth and draining the underflow product separates the two products. Reproduced from Salces et al., (2022) [53].

Technical challenges on Froth flotation
The effectiveness of froth flotation is influenced by multiple factors, which are the technical challenges when performing froth flotation:

1. **The pre-treatment performed to obtain the black mass**: Residual binder in the black mass influences the wettability characteristics of both the anode and cathode active material [63, 76]. Therefore, the pre-treatment process affects the performance of the froth flotation process. A shift in the wettability of the materials with the presence of the binder likely promotes the recovery of LMO at the froth phase by true flotation. It results in a lower grade of graphite recovery from the froth.
2. **The use of reagents**: Frothers and collectors are utilised to enhance the separation process during forth flotation. The selection and optimisation of these reagents pose significant technical challenges in froth flotation. Frothers play a crucial role in achieving high separation efficiency by stabilising air bubbles and collectors by facilitating the attachment of hydrophobic particles to these bubbles [25, 63, 48]. The challenge lies in finding a balance between maximising graphite recovery and minimising the recovery of LMO particles in the froth phase. Collectors used in the process interact strongly with both graphite and LMO particles. As a result, LMO particles exhibit some frothability, leading to their unintentional collection in the froth phase. This unintended attachment of LMOs reduces the purity and grade of the froth product.
3. **Non-selective flotation mechanisms**: Entrainment and entrapment are common challenges in froth flotation processes. Both mechanisms reduce the selectivity and overall efficiency of the froth flotation process, making separating anode and cathode material challenging. To mitigate the entrapment of small LMO particles within large graphite agglomerates, it is crucial to ensure good dispersion throughout the flotation stage to prevent the formation of agglomerates in the pulp and the froth [63]. Another approach involves incorporating an additional pre-treatment step, such as attrition, to break down the agglomerates and achieve better particle dispersion during flotation [65]. Wetting agents and dispersants can also be employed to disrupt these agglomerates and improve dispersion [48]. A potential solution to mitigate entrainment is the implementation of selective flocculation for the LMO particles. This process involves high-density flocculates that selectively aggregate the LMOs, thereby reducing their susceptibility to entrainment [58].
4. **Processability in water**: Froth flotation requires the active materials fed into the flotation tank to be compatible with water, meaning their structure and morphology should not be affected by water. Studies have shown that separating LCO and graphite through froth flotation and recovering them for use in new electrodes results in a minimal decrease in electrochemical performance. However, Nickel-based active materials like NMC are susceptible to water-related issues [40]. To enable aqueous processing, battery manufacturers are exploring modified Nickel-based materials with protective coatings [57]. This consideration is significant for electrode production, including the choice of binder material, and for recycling strategies such as flotation.

Addressing these technical challenges is crucial for successfully implementing froth flotation in separating graphite from the black mass.

1.2.4. Gravitational/centrifugal based sedimentation

Another promising physical separation method for separating the cathode and anode material from the black mass is gravitational and centrifugal-based sedimentation. Separation by sedimentation is based on the difference in particle size. Like froth flotation, this method can be essential in circular battery recycling. As explained, the black mass of spent Lithium-ion batteries is mainly composed of graphite and lithium metal oxide particles. Table A.1 shown in Appendix A provides an overview of the typical grain types present in the finest fraction of the black mass, along with their average size and density. Advantages can be taken from these differences in size and density of the particles using the principle of sedimentation.

This method of separation is shown to be very promising. In literature, research conducting centrifuge experiments has shown successful separation of LFP cathode material from Carbon Black particles using a Tubular Bowl centrifuge [71, 45]. Figure 1.6 shows a schematic of the centrifuge. As seen from the machine's dimensions, it is a small, compact tube where the separation occurs, with a tube height of around 19 centimetres and a width of only 2.15 centimetres. Black mass dispersed in water is pumped through the bottom of a rotating cylinder. Centrifugal forces are applied to the accelerated particles due to the high rotational speeds of the tube. Generally, the bigger and denser particles are separated in the cylinder and will build up at the side walls of the tube, the so-called sediment. The smaller, less dense particles are pushed through the outlet at the top and end up in the centrate.

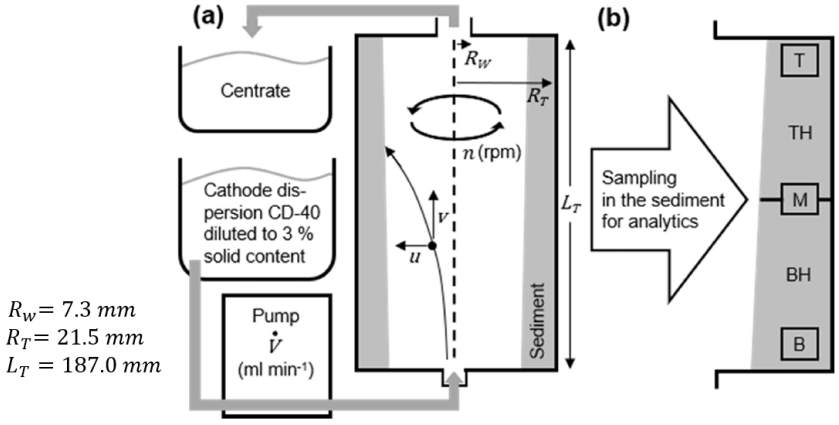

Figure 1.6: (a) Schematic experimental setup of tubular centrifuge including a pump that determines the volumetric flow rate $\dot{V}$ and the centrifuge tube with the rotational speed n. The most important centrifuge dimensions are the weir radius R_w, the tube radius R_t and the tube length L_T. The pathways through the tube of incoming particles are determined by their sedimentation speed u and their percolation speed v. (b) Illustration of sampling the sediment of bottom (B), middle (M) and top (T) of the build-up and further top half (TH) and bottom half (BH) where samples are taken to be analysed by SEM analysis. Reproduced and modified from Wolf et al., (2021) [71].

1.2.5. Theoretical Estimates for particle separation by sedimentation

In this section, some theoretical results are reported, which are useful to interpret the sedimentation experiments described in this thesis.

Sedimentation Principle and Stokes' Law

When solid particles are suspended in a tube filled with a fluid, having a smaller density than the particles, the particles will settle and accumulate at the bottom under external forces (for example, gravity or centrifugal forces). Their size, shape, and density influence the settling rate at which they settle to the bottom [28]. Therefore, particles with different sizes and densities will settle at different rates, where bigger and denser particles will settle faster than smaller and less dense ones. This difference in the settling rate between particles can be exploited for separation.

Stokes' law can be applied to model the settling rate of small spherical particles in a fluid [28]. Based on the size and density information for typical grains from Li-ion batteries provided in Appendix A, the Reynolds numbers (Re) for these grains in water and air are presented. The Re numbers are well below 1 for these micro-sized particles, indicating that Stokes' Law can be employed to model the settling velocities of these grains in both water and air [13]. The settling rate for a particle with a diameter d_p and density ρ_p in a fluid with density ρ_f and dynamic viscosity μ, according to Stokes' law is given by:

$$v_s = \frac{g}{18\mu}(\rho_p - \rho_f)d_p^2 \tag{1.1}$$

This equation is derived in Appendix B.1 from a simple force balance on a spherical-shaped particle in a Newtonian fluid in the regime of low Reynolds numbers. The equation reasonably estimates the fall speed of a roughly spherically shaped particle [28], like the typical grains from Li-ion battery materials.

Hindered-settling effect

The Stokes settling rate (equation 1.1) is strictly valid only for a single particle and is, therefore, only a good approximation for extremely dilute suspensions. Considering a concentration with a volume fraction of particles (ϕ) in a fixed container, the behaviour of the particles suspended in the fluid differs from that of a single particle. The dynamics of the particles is determined by the hydrodynamic interactions between the particles and the fluid [28]. Due to the upward fluid flow caused by the movement of falling particles, the average sedimentation speed for multiple particles is lower than the single particle Stokes' velocity.

This upward flow follows from mass continuity. The average mixture velocity is equal to zero:

$$\langle v \rangle = \phi\langle v_p \rangle + (1-\phi)\langle v_f \rangle = 0 \tag{1.2}$$

Therefore, as $\langle v_p \rangle > 0$, the fluid moves upwards with average velocity $\langle v_f \rangle < 0$ to compensate for the settling particles. This is the dominant effect, leading to a mean particle sedimentation velocity less than the Stokes velocity [28].

This speed reduction is called the hindered settling effect. The mean settling velocity for a suspension of particles with volume fraction ϕ can be written as:

$$\langle v_p \rangle = v_s f(\phi) \tag{1.3}$$

Here, v_s is the Stokes velocity for a single particle (equation (1.1). The hindered settling function $f(\phi)$ is a decreasing function of ϕ, having a value between 0 and 1.

An empirical formula can be used to model the hindered settling. A widely used empirical correlation for the hindered settling function is the Richardson-Zaki (R-Z) correlation:

$$f(\phi) = (1-\phi)^n \tag{1.4}$$

The value of n depends mainly on the Reynolds number, and a value of $n = 5$ most accurately represents the experimental data for small Reynolds numbers [2, 28]. This Richardson-Zaki correlation holds for monodisperse solutions, with particles having all the same size and density.

Regions in Polydisperse suspensions

While most literature has traditionally focused on the sedimentation process for monodisperse suspensions, polydisperse suspensions are far more common in practice. In most practical cases where a mixture of materials is used, the suspension contains all types of particles with different sizes and densities. The liberated black mass from Li-ion batteries is a powder containing particles with a distribution of sizes.

When these are suspended in a fluid, the bigger and denser ones will fall faster and move away from the smaller and lighter ones. Besides that, the relative positions of suspended particles continually change, which causes the particle velocities to fluctuate during the sedimentation process [18]. The velocity fluctuations of individual particles and the size, shape, and density differences will create different regions in the suspension after the particles are homogeneously well-mixed.

Considering a bidisperse suspension of two-particle classes with different sizes and densities, regions will be formed after dispersing the mixture in the fluid. For a well-mixed bidisperse suspension, two different regions will be formed in the supernatant during the sedimentation process, as shown in figure 1.7a [2, 18, 33]. A lower region, denoted as 1, contains both particle species at their initial bulk concentrations, and an upper region, indicated as 2, has only the slower-settling species. By this, two interfaces are created: one that separates the upper region from the clear fluid above it and the other that separates the upper and lower regions. A growing sediment layer containing stationary particles is found at the bottom.

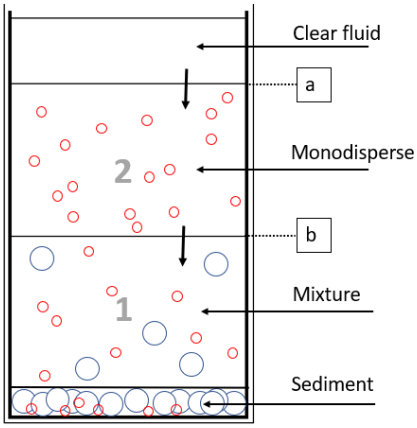

(a) Schematic of regions in bidisperse suspension

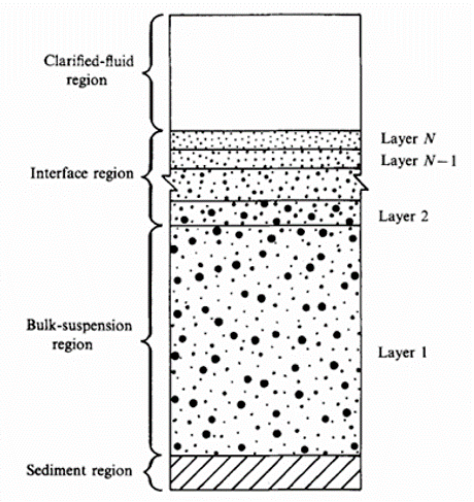

(b) Schematic of regions in discretised polydisperse suspension Reproduced from Davis et al., (1988) [19]

Figure 1.7: (a) Sketch of the different regions during sedimentation of a suspension of bidisperse species in a tank with fixed bottom and vertical side walls. Two regions, 1 and 2, can be observed after the dispersion of the particles. Region 1 contains a mixture of particle classes, and Region 2 contains only the lighter particles. Therefore, two interfaces, a and b, are created, moving downwards through the sedimentation process. (b) Schematic of the different regions formed during sedimentation of a polydisperse suspension in a tank with a fixed bottom and vertical side walls. In practice, the interface that separates the clear fluid region ($\phi = 0$ from the bulk suspension (ϕ_0) is a region on its own that can be defined by different layers.

In a polydisperse suspension with multiple species exhibiting a distribution of particle sizes, it is found that the upper interface separating the clear fluid from the bulk suspension region is not one sharp line. Regions 1 and 2 of the bidisperse case in Figure a can be divided into N smaller regions (denoted as N discrete layers), as shown in Figure 1.7. For particles that exhibit a size distribution with N size range intervals, the suspension can be divided into N layers during sedimentation. Layer 1 represents the bulk suspension, containing all particles at their original concentration. Starting from layer 2, each successive layer is devoid of the fastest-settling particles from the layer below, up to the top layer N containing only the slowest-settling particles of the smallest size range.

In practice, this interface proceeds during sedimentation as a region on itself, as shown in the Schematic of Figure 1.7, and its width changes throughout the sedimentation process. The shape of the interface region is a combined effect of three physical phenomena: As mentioned in the earlier subsection, the concentration of particles in a suspension causes a hindered settling effect: the sedimentation rate of particles is reduced for increasing concentration due to the hindered settling effect. The consequence of the hindered settling for the interface is a so-called self-sharpening effect: the spreading of the interface is reduced (= sharpened) as the particle concentration increases. The size distributions of the particles cause the second effect and lead to the distribution of sedimentation velocities and, therefore, the broadening of the interface. The third effect is the velocity fluctuations due to the constant change of the relative positions of particles causing the spreading and diffusion of this same interface, even if the particles are monodisperse and no local gradient of volume fraction is present [37].

Settling rates in polydisperse systems

We introduce a model for suspensions containing particles that differ in size, used for comparing with measurements of sedimentation of Li-ion battery material, described in Chapter 3. Only a few analytical models are available for polydisperse suspensions, as it seems rather difficult to account for the hydrodynamic interactions between particles that differ in size and density. It was shown empirically for very dilute polydisperse suspensions only, $\phi < 0.05$, that the Richardson-Zaki equation (1.4) approximates the settling velocities [8].

A relatively straightforward model developed from the basic balance equations of continuum mechanics is the Masliyah-Lockett-Basoon (MLB) equation [33]. This equation is a generalisation of the Richardson-Zaki equation, extended for multiple species having different sizes and densities. The central assumption is that the interaction force between fluid and the ith species is given by a concentration-dependent factor, multiplying the so-called slip velocity $v_i - v_f$, which is the relative solid-fluid velocity.

We can analyse the bidisperse case, as it is easier to analyse the mathematical structure in this case. According to the MLB model, for a bidisperse suspension with component 1 and component 2, the slip velocity can be written as:

$$v_1 - v_f = \frac{g d_1^2 (\rho_1 - \rho_{\text{susp}}) \phi_f^{2.7}}{18 \mu_f} \tag{1.5}$$

and

$$v_2 - v_f = \frac{g d_2^2 (\rho_2 - \rho_{\text{susp}}) \phi_f^{2.7}}{18 \mu_f} \tag{1.6}$$

Here, ρ_{susp} is the suspension density, defined as the sum of the components density-weighted by their volume fraction in the suspension. So, for a bidisperse suspension, the density is written as:

$$\rho_{\text{susp}} = \rho_1 \phi_1 + \rho_2 \phi_2 + \rho_f \phi_f \tag{1.7}$$

Combining equations (1.5), (1.6) with the mass balance equation for a closed water tank (1.2), gives:

$$v_1 = \frac{g \phi_f^{2.7}}{18 \mu_f} [d_1^2 (1 - \phi_1)(\rho_1 - \rho_{\text{susp}}) - d_2^2 \phi_2 (\rho_2 - \rho_{\text{susp}})] \tag{1.8}$$

$$v_2 = \frac{g \phi_f^{2.7}}{18 \mu_f} [d_2^2 (1 - \phi_2)(\rho_2 - \rho_{\text{susp}}) - d_1^2 \phi_1 (\rho_1 - \rho_{\text{susp}})] \tag{1.9}$$

These equations show that their velocities depend on particle sizes, densities, and volume fractions. They reduce to the Richardson-Zaki correlation when only one species exists. The advantage of the MLB model over others (e.g. Stokes and R-Z correlation) is that it can also be used for higher particle concentrations of polydisperse systems. Also, an inherent advantage of the MLB model is the use of slip velocity. From mass continuity, equation 1.2, it follows that for higher values of ϕ, the upward flow of the fluid is substantial.

Regarding the different regions in the suspensions, one must carefully look at where the introduced equations of Stokes, MLB and R-Z can be used to say something about the velocity of the different fronts in the suspension considering different volume fractions, as shown in Figure 1.7a. The MLB equations assume that the region where both species exist is uniform, the mixture region (region 1 in figure 1.7a). For region 2, the MLB model for monodisperse suspension is needed as only one species is present, which then reduces to the R-Z equation.

Stokes' law, together with R-Z and the MLB model, can be used to estimate the attainable size ratios that facilitate separation through sedimentation for the Li-ion battery particle classes. Appendix H introduces a simple model for determining the size ratios for effectively separating anode and cathode material based on the literature findings.

1.2.6. Technical challenges on Sedimentation of Active materials from Li-ion Batteries

Based on the literature review of the previous sections, we can identify the following challenges related to centrifugation to separate the active materials from Li-ion batteries:

1. **Particle Size Distribution**: The effectiveness of sedimentation relies on the size and density differences between particles. As shown in Table A.1 from Appendix A, the materials all have a size distribution, as they are powders. When comparing different grain types such as LCO, NMC, and graphite, it is observed that these powders have similar size distributions within the range of 10 - 40 µm, resulting in comparable settling velocities. Consequently, separation by sedimentation alone may not be feasible. By manipulating the particle size distribution, it is possible to achieve a substantial difference in settling velocity, enabling effective separation of the anode and cathode materials. Therefore, a marked difference in the size of the anode and cathode grains would contribute to the circularity of Li-ion batteries.
2. **Aggregates in the sediment** As aggregates of particles are present in the centrifuge, the smaller particles also have a chance to reach the sediment. Aggregates of smaller particles have a higher likelihood of settling faster even before the forces in the centrifuge have broken those agglomerates. Thereby, the separation efficiency is reduced.
3. **Optimisation of Centrifuge Parameters**: Selecting the appropriate centrifuge parameters, such as rotational speed, tube radius, weir radius, and tube length, presents a challenge. The optimal combination of these parameters must be determined to achieve efficient sedimentation and separation of particles. This requires considering the specific characteristics of the feed and the desired separation outcome.
4. **Processability in the fluid** Centrifugation requires the active materials from the feed to be compatible with the fluid in which the particles are suspended, meaning their structure and morphology should not be affected by the fluid. For example, it has been shown that nickel-based cathode chemistries like NMC are susceptible to water-related issues. Nickel and lithium ions might dissolve in water [40, 4].
5. **Margin Particle Diameter estimation** Estimating the margin particle diameter, which determines the particles' distribution between the sediment and centrate, is crucial for process optimisation. Developing an accurate model and testing this hypothesis with experimental techniques for specific particle types and centrifuge configurations is a technical challenge.

Understanding these technical hurdles would contribute to more efficient and effective sedimentation processes in centrifugation, enabling improved separation of graphite from the black mass.

1.3. Research Objectives

This thesis aims to show that sedimentation is a viable method to separate the anode and cathode materials from Li-ion batteries if the battery grain size is designed appropriately. To bring evidence that this circularity principle could be applied, this thesis aims to answer 3 research questions:

1. **Are there differences in morphology between anode and cathode material from opened batteries, and what happens to their morphology after milling them? How does that affect their size distribution, and what would it mean for separation by sedimentation?**

   A commercial Li-ion battery is dismantled to obtain the individual electrode materials, anode and cathode, that are analysed using Scanning Electron Microscopy (SEM) and Inductively Coupled Plasma - Optical Emission Spectroscopy (ICP-OES). The materials are ground using a ball miller and also examined. The size- and velocity distributions of these samples are calculated to show insights into their theoretical separation efficiency.

2. **What are the differences in sedimentation behaviour between anode and cathode material, and what is the influence of concentration and grinding the material? Can we quantify the sedimentation rate of the materials?**

   The sedimentation process of the individual materials in water is tracked by using a camera to make subsequent images of the process to find settling rates as a function of milling time and concentration. The results from the experiments are compared with an analytical model for sedimentation based on the particle size distributions of the samples.

3. **What techniques can be used to assess whether separation occurred after water sedimentation? Additionally, does processing in water affect the morphology of the electrode materials?**

   A new method based on freezing is proposed for this project. Suspensions containing NMC and graphite are frozen after sedimentation, and the horizontal layers are cut off and separated. Those layers are dried and analysed using SEM and ICP-OES to look for differences in size, shape, and elemental composition throughout the sediment. Thermogravimetric Analysis (TGA) is performed on frozen suspensions of $LiFePO_4$ and graphite to get an understanding of the thermal stability of the materials

2

Analysis of anode and cathode grains

In this chapter, we present the typical materials from the black mass of a Li-ion battery by analysing the anode and cathode grains. Therefore, we opened a spent battery and obtained the electrode materials separately. The samples are milled to alter their sizes. By creating size distributions, we look for the potential of sedimentation to separate the particles by size. Therefore, we calculate their velocity distributions to get an overview of anode-cathode sample combinations for which they could be easily separated.

2.1. Disassembling a commercial Li-ion Battery

A commercial powerbank (Xiaomi MI PLM06ZM), equipped with a Li-ion battery cell, was disassembled to obtain the anode and cathode materials. The disassembling process requires specific safety measures, detailed in Appendix C, along with a detailed, step-by-step description of the actions taken.

The outer plastic casing of the powerbank was removed, revealing the pouch cells. These cells were discharged by immersing the pouch cells in a salt solution bath containing 10 wt.% Potassium Carbonate for at least 48 hours to ensure their voltage dropped below 2 V, making it safe to open them.

To separate the active anode and cathode material from the current collectors, the binder material was dissolved using N-Methyl-2-Pyrrolidone (NMP). The unrolled electrode sheets were separately cut into small pieces of approximately 5x5 cm and placed in a sieve. This sieve, which was positioned in a well-fitting beaker, was filled with NMP, completely submerging the electrode pieces. The beaker was placed in an ultrasonic bath filled with water to enhance the dissolving process, as depicted in Figure 2.1c. Ultrasonification was conducted for about two hours at 70 °C. After dissolving the binder, the current collector foils in the sieve were removed. The resulting emulsion was left for at least 24 hours to ensure the precipitation of all active material.

The suspension of NMP and binder material was carefully poured off, ensuring that only the precipitated material remained in the beaker. To evaporate the last traces of NMP, the resulting black mass was dried at 120 °C. This process was applied to both the anode and cathode sheets. The resulting dried black mass is a granular powder containing the liberated active material. This is done separately for the anode and cathode. The powders were stored and used for further sedimentation research.

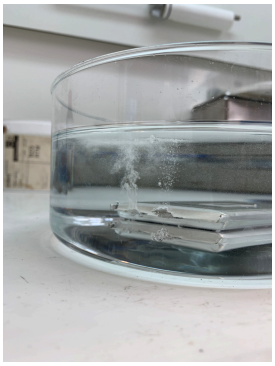

(a) Discharge of pouch cells in a salt solution. Bubbles, resulting from water electrolysis, are visible at the electrode ends, producing hydrogen and oxygen.

(b) Unrolled electrode sheets and separator extracted from the opened battery cell.

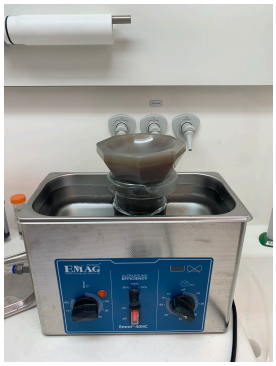

(c) Ultrasonic bath filled with de-ionised water. A beaker containing the electrode sheets and NMP facilitates the dissolution of the binder.

Figure 2.1: Consecutive steps in obtaining black mass from a Li-ion battery.

2.2. Composition and morphology of the active materials

The morphology of the anode and cathode particles was evaluated using Scanning Electron Microscopy (SEM). The powder samples were placed on a carbon tape on the SEM specimen holder and analysed using the SEM ISM IT100.

Inductively Coupled Plasma - Optical Emission Spectroscopy (ICP-OES) is performed on the samples to investigate the elemental composition of the materials. ICP-OES was conducted using the Spectro Arcos EOP model. Samples were dissolved in a solution containing 35% nitric acid (HNO_3) and subsequently mixed with hydrogen peroxide (H_2O_2) twice. The resulting mixture was allowed to stand for several days with occasional agitation. Later, the clear liquid phase was subjected to ICP-OES measurement.

As the anode and cathode samples exhibit particles of all different sizes that cannot be visualised completely, size distributions are created to characterise the particles in the samples. Scanning electron microscope (SEM) images were acquired at three distinct locations on the carbon tape, ensuring the selection of spots where individual particles are visible. Subsequently, utilising ImageJ software, automatic particle counting was performed by importing SEM images and converting the pixel-based length scale to micrometres. A defined threshold range was established to differentiate individual particles from each other and the image background.

The 'Analyse Particles' function in ImageJ was used for particle counting, listing the outlined particle areas. An average particle diameter was calculated from these particle areas, assuming a spherical shape for all particles. This process generated a particle size distribution for the samples, with analysis conducted across different images corresponding to various spots on the carbon tape within the SEM specimen holder.

In this study, the particle size distributions were analysed by merging data from three distinct locations, and each sample comprises approximately 130 particle size measurements. This ensures a comprehensive representation of the particle size spectrum.

Particle size distribution curves were created to facilitate meaningful comparisons across different samples. These curves were constructed by interpolating through the tops of the histogram bins while maintaining a consistent bin width.

Elemental composition
ICP analysis of anode and cathode powder samples provides the elemental composition of the two materials in weight percentage (wt.%). Figure 2.2 illustrates the elemental composition of both electrode materials.

Almost all the anode composition is assigned to 'Not measured' content, 97 % of the weight. Most of it can be attributed to carbon, primarily originating from graphite. The major anode component, graphite, cannot be measured directly by ICP-OES. Also, traces of lithium (1.5 wt.%) are detected, commonly measured in the anode of a cycled Li-ion battery, due to the earlier formation of a Solid-Electrolyte-Interface (SEI) and lithium dendrites [47]. 'Traces' include minimal traces of Copper, Phosphate, Sulfate, and Sulfur, constituting less than 1.5 wt.% of the anode's mass.

The cathode shows an elemental composition primarily consisting of Nickel (28%) and Manganese (23%), along with a smaller amount of Cobalt (4%). The 'Traces' category of the cathode includes a few percentage points of carbon but predominantly oxygen, reflecting the oxide nature of the cathode material. Lithium metal oxides would comprise 50% oxygen on a molar basis, corresponding to an expected 33 wt.% oxygen content, which can be assigned to the fraction that ICP-OES cannot measure. The cathode ICP-OES analysis indicates a composition consistent with an NMC cathode chemistry, featuring a lower cobalt ratio than nickel and manganese.

Appendix D provides Table D.1, which includes all the measured elemental fractions of Anode and Cathode.

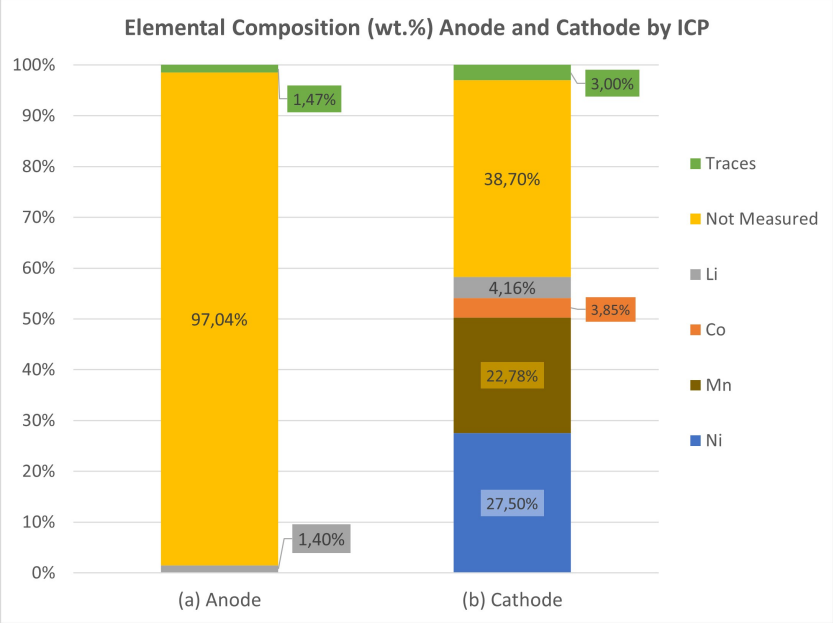

Figure 2.2: Elemental composition in weight fraction of the anode and cathode materials of the Xiaomi Powerbank after binder dissolvement. (a) The anode comprises almost only carbon material, which ICP-OES cannot measure, primarily attributed to graphite (97.04 wt.%). Also, some Lithium (1.4 wt.%) is found in the anode, typical for a used Li-ion battery. (b) The cathode comprises mostly Nickel and Manganese (28 and 23 wt.%, respectively) with some Cobalt (4 wt.%), consistent with NMC Cathode chemistry. The 'Not Measured' category (39 wt%) mostly consists of oxygen and likely a small amount of carbon. 'Traces' include elements with a fraction smaller than 0.5 wt.%. these can be found in Appendix D where Table D.1 show all the measured elements.

Particle morphology and size distribution

The morphology of both the anode and cathode materials was investigated using Scanning Electron Microscopy (SEM), revealing their particle structure, size, and shape. Figure 2.3 presents the SEM images of the dry cathode and anode powder.

The SEM images of the anode material unveil graphite particles characterised by a distinctive layered structure. These particles, with a spherical or elliptical shape, conform to the 'spheroidized' configuration typical of graphite particles employed in Li-ion batteries. The lamella-like structure arises from compacted graphite flakes [23, 64]. Additionally, the SEM images reveal the presence of loose, thin flakes surrounding the larger spheroidized particles. These thin flakes exhibit an elongated and sharply defined shape, with dimensions ranging from approximately 3 - 7 μm, while the spheroidized layered particles measure primarily between 10 and 30 μm in diameter.

While the larger primary spheroidized graphite particles are visible, there are also a lot of overlapping and touching flakes forming randomly clustered shapes. As a result, distinguishing between individual grains becomes challenging in some regions of the anode sample.

The cathode particles, mostly spherical, exhibit sizes ranging from 1 to 20 μm. Notably, the SEM images reveal these particles' distinctive porous surface structure. This observation aligns with findings in the literature focused on NMC cathode particles, where surface porosity is recognised for shortening the Li diffusion path, beneficial for the battery's power density [41]. Importantly, these particles exhibit excellent liberation, devoid of clumping or aggregation, allowing the particles to be easily recognised as individual grains on the SEM images.

As seen in the SEM images, the size of both the anode and cathode particles is not one particular size; instead, they exhibit a distribution of sizes. Figure 2.3c) shows the size distributions of dry-powder anode and cathode. As can be seen, the anode material comprises predominantly larger particles and a broader size distribution than the cathode material. The broad size distribution of the anode is due to the combination of bigger spheroidized graphite and the clustered flakes in the powder. As primarily spheroidized graphite particles are present, the average size of the counted anode particles is 16 μm. In contrast, the average cathode particle size is 7 μm, with a more narrow distribution as most cathode particles have a similar size and spherical shape.

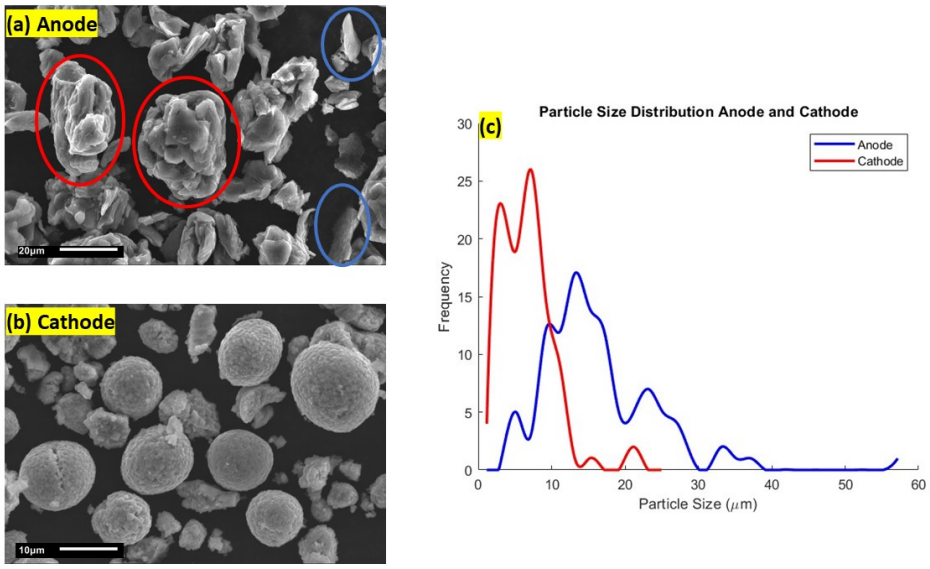

Figure 2.3: (a) SEM Image of dry powder anode. Circled in red, the bigger particles have a spherical and elliptical shape with a layered structure, surrounded by smaller thin graphite flakes, circled in blue. Also, many undefined-shaped clustered flakes are visible, making it difficult to distinguish individual grains. (b) SEM image of dry powder Cathode. The particles exhibit a typical spherical shape with a porous surface structure. (c) Particle Size Distributions of Anode and Cathode that follow from the SEM images of the dry powders. The anode exhibits a broad size range of 3 - 56 μm, while the cathode material exhibits a smaller range between 1 - 20 μm.

2.2.1. Grinding the active materials

The anode and cathode materials underwent a grinding process using a Hertsch MM2 Ball Miller. This machine has two milling jars at the front, designed to vibrate horizontally at a specified frequency, as illustrated in Figure 2.4. Each milling jar was filled with 2-3 grams of either anode or cathode dry powder. To explore the effect of milling duration on grinding performance, three different samples were prepared for both materials, corresponding to milling times of 5, 10, and 30 minutes. All milling experiments were conducted using the highest oscillating frequency setting of the miller at 100 Hz.

(a) Hertsch MM2 Ball Miller used for grinding the black mass material. At the front, two jars are tightened in the holders, which are horizontally oscillated.

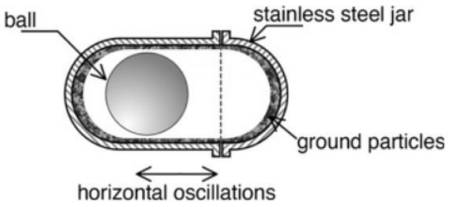

(b) Schematic of the jar at the front of the ball miller. Reproduced from Blanc et al. [10].

Figure 2.4: The ball miller consists of a cylindrical stainless steel casing with powder and a 25 mm steel ball inside. The jar oscillates horizontally, setting the ball and powder in motion. This causes impact and shear forces on the particles, thereby grinding them. The powder accumulates at the inner side walls of the jar.

Effect of grinding active material on morphology and size distribution

Grinding the materials using the ball mill significantly affects the morphology of both anode and cathode material in size and surface structure.

Figures 2.5a and 2.5b show two cathode samples after milling. The spherical NMC particles remain recognisable from the original sample before milling, exhibiting a size of approximately 8 - 15 µm. However, a notable transformation is observed in the surface structure of the spherical particles, which now predominantly comprise loosely attached, protruding flakes. These flakes are also evident as clouds surrounding the larger particles in the images. It appears that these flaky components have become detached from the larger particles. These clouds of small flakes are seen at many spots on the SEM. All the differently timed milled samples appear in this formation: the bigger spherical particles with clouds of flakes surrounding them, as also can be seen in the zoomed-out Figure 2.5

A notable transformation is observed in the anode's morphology after milling, as seen in Figure 2.5c and 2.5d. The particles are generally significantly smaller, exhibiting a more irregular, wider range of shapes and sizes with rougher surfaces than the unmilled anode material. The typical spheroidized graphite particles remain visible but are now surrounded by many smaller graphite flakes detached from the larger spherical particles. The edges of the thin plate-like sheets seem sharp and jagged, indicating that they have been sheared from the spheroidized particles and scattered. These flakes form broad clusters spread through the sample, as shown in Figure 2.5d.

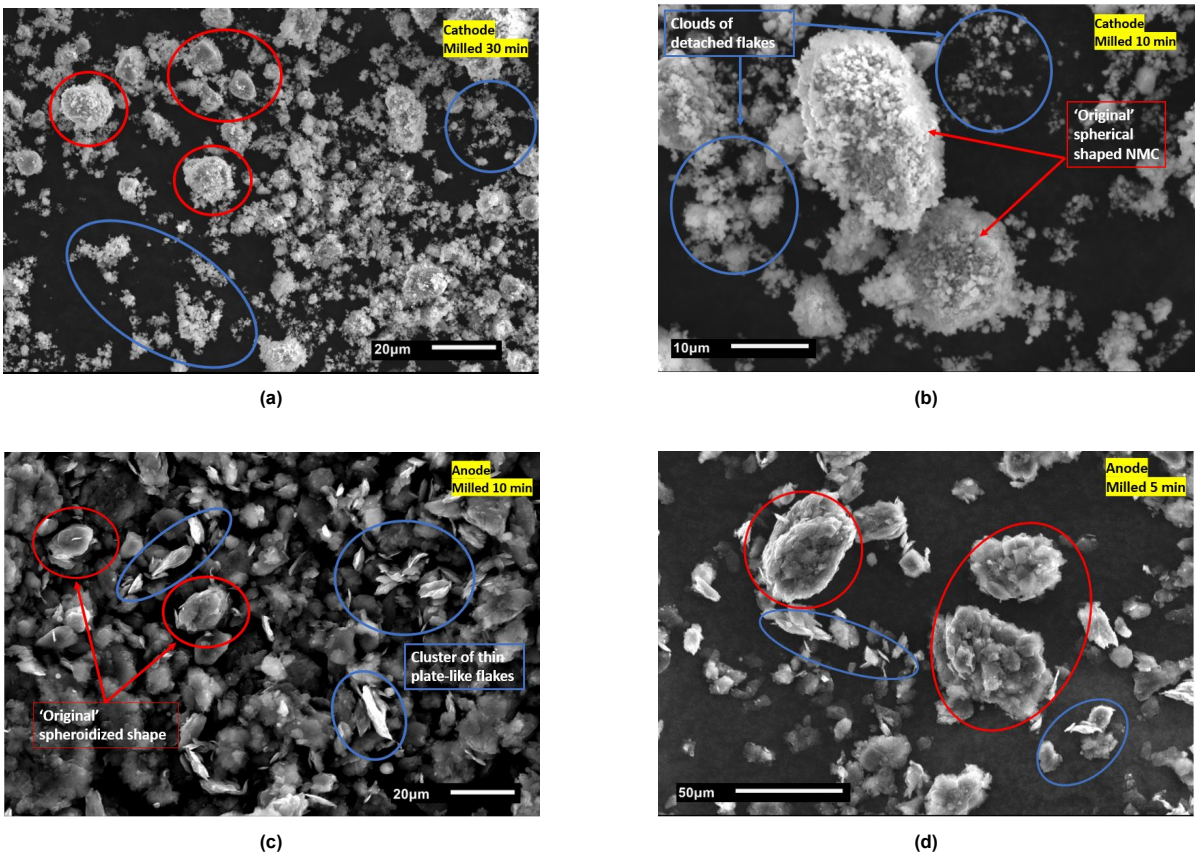

Figure 2.5: SEM images of milled anode and cathode samples. (a),(b): Cathode milled 30 and 10 min., respectively: in red, the original spherical porous cathode particles with a rougher structure, surrounded by many sheared clouds of small particles (circled in blue). (c), (d): Anode milled 10 min. and 5 min., respectively: Irregular and angular-shaped particles are visible (circled in blue) together with some 'original' spheroidized graphite particles (in red).

Figure 2.6 illustrates the different milled cathode and anode particle size distributions. The cathode distributions in Figure 2.6a show a significant shift towards smaller sizes, with most particles having a size between 0.5 and 2.5 µm. The high peak in the distribution around 0.5 µm corresponds to the clouds of small flakes visible from the SEM images. A few large original particles were counted from the images with a size of 5 - 15 µm. The zoomed-in image shows differences between the milled samples. The 5 min. sample exhibits a broader distribution containing mostly particles with sizes between 0.25 and 4 µm, while the 10 and 30 min. samples are more narrowed: they contain primarily particles with a size between 0.25 and 1 µm.

Figure 2.6b shows the anode size distributions. Like the cathode, milling similarly induces a pronounced shift towards smaller sizes with a peak between 0.1 and 0.8 µm, as seen from the zoomed-in distribution. However, the milled size distributions are broader than the cathode distributions. This corresponds to the observed anode flakes from the SEM images, exhibiting sizes between 0.25 and 10 µm, while a few original spheroidized graphite particles are observed with a size of around 10 - 25 µm.

The average particle size of the unmilled and milled samples is shown to capture the shift in size distributions for both anode and cathode. The shift in average particle size of the cathode is found from 6.6 µm to an average size of 1.1 µm for the milled cathode distributions. An even more significant shift is observed for the anode: from 16.2 µm for the unmilled anode to about 2 µm for the milled anode.

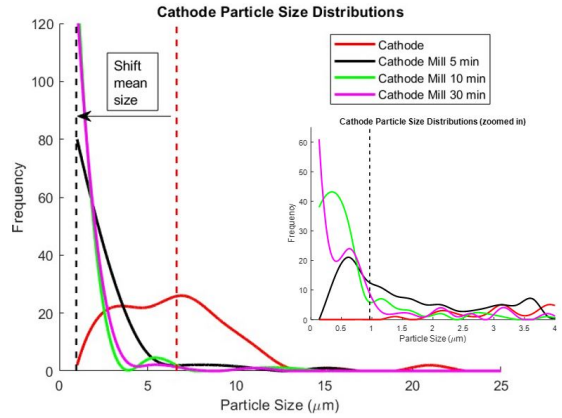

(a) Cathode: A pronounced shift towards smaller particle size due to milling is observed, corresponding to the clouds of small flakes in the milled samples. A significant shift of the average size is shown: from 6.6 μm towards a value of 1.1 μm.

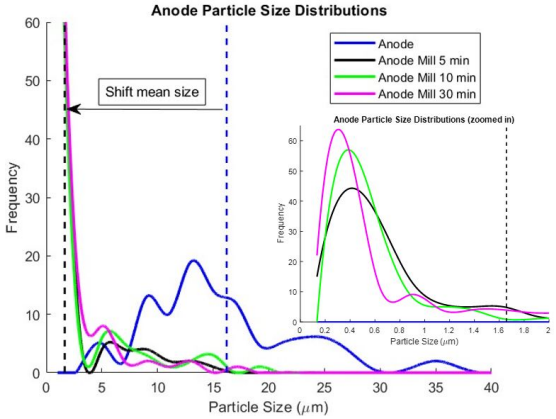

(b) Anode: Milling shifts the size distribution to small sizes, corresponding to observing small sheared graphite flakes in the SEM images. A big shift of the average value is shown: from 14.8 μm to 2 μm.

Figure 2.6: Particle Size Distributions cathode-anode for different milling times with a binwidth of 2 μm and a zoomed-in figure with binwidth of 0.25 μm.

2.3. Theoretical separation efficiency using velocity distributions

The particle analysis of the anode and cathode aims to find the potential for separation by sedimentation of the electrode materials. As separation through sedimentation is based on the differences in settling velocities (fall speed of particles in a fluid), velocity distributions for anode and cathode are calculated to see how they differentiate.

Particle velocity distributions are derived from the earlier created particle size distributions using Stokes' law for the individual settling speed of a small particle in water of a dilute suspension. As Stokes' velocity depends on particle size, the size of the individual particle was converted to the corresponding Stokes' velocity of this particle in water. By doing this calculation for all the particles of a sample, a new histogram that plots the distribution of particle velocities was created. Similar to the particle size distributions for all analysed samples, the curves of the velocity distributions were constructed by interpolating through the tops of the histogram bins while maintaining a constant bin width.

2.3.1. Overlap of velocity distributions

To assess the potential for sedimentation-based separation of (un)milled anode and cathode materials, the overlap of velocity distributions was analysed for all combinations of unmilled/milled anode and cathode samples. A greater overlap of sedimentation velocities indicates that a higher fraction of particle sizes have a similar settling velocity so that separation will be more challenging.

Analysing this overlap involves calculating the area below the minimum of the interpolated curves across the entire velocity range (v_{min} - v_{max}). If we take two particle size distributions with corresponding velocity distributions curves f(v) and g(v), we can write the integral as:

$$A_{\text{overlap}} = \int_{v_{\text{min}}}^{v_{\text{max}}} \min(f(v), g(v))\, \mathrm{d}v \tag{2.1}$$

Here, the 'Overlap Area' measures the overlap between two velocity distributions, f and g, where the curves f(v) and g(v) are constructed from the velocity histograms using the Stokes' velocities of the particle size distributions.

To evaluate the potential for sedimentation-based separation of anode and cathode, the velocity distributions corresponding to the Stokes' velocities of the size distributions were examined for all samples. The results are summarised in Table 2.1.

The matrix shows that the original, unmilled combination of anode and cathode exhibits the highest overlap in velocity distribution. As expected, milling either anode or cathode reduces this overlap, aligning with the shifts in the size distributions illustrated in Figure 2.6. This results in a corresponding shift in velocity distribution towards smaller settling rates. Therefore, the overlap area is significantly reduced by more than 50 % for combinations involving one unmilled material and the other milled, evident in both the matrix's top row and leftmost column. This reduced overlap is attributed to the distinct effects of milling on anode and cathode size distributions. In line with what was seen in the size distributions, variations in milling time for the cathode and anode do not significantly affect the overlap area. Notably, when both materials are milled, the overlap area increases, highlighting the similar impact of milling on both.

Overlap Size Area Velocity Distributions

Anode \ Cathode	No mill	Mill 5 min	Mill 10 min	Mill 30 min
No Mill	3,37	1,07	1,06	0,93
Mill 5 min	1,4	2,18	2,17	1,83
Mill 10 min	1,51	2,04	2,05	1,84
Mill 30 min	1,34	2,35	2,29	1,78

Table 2.1: Experimental Matrix of all sample combinations for anode and cathode. The calculated area overlap of the velocity distributions is presented. The colour gradient indicates the degree of overlap, ranging from the highest (red) to the smallest (green). The combination of the unmilled anode and 30-minute milled cathode exhibits the smallest overlap, suggesting the most distinct velocity distribution range and presenting the best opportunity for effective separation by sedimentation. Conversely, the combination of both unmilled materials shows the highest overlap, posing a greater challenge for separation.

To assess the practical implications of the overlap area for separating anode and cathode materials and to understand the effects of milling, we analyse the 'best' and 'worst' combinations in terms of the overlapping area. From Table 2.1, we observe that the combination of unmilled anode and cathode shows the highest overlap, indicating that this is the worst combination in terms of separation. The 'best' combination, showing the smallest distributions overlap, is the unmilled anode with 30 min. milled cathode.

Figure 2.7 illustrates the size- and velocity distributions of Anode, Cathode, and 30-minute Milled Cathode. The velocity distributions on the right highlight the calculated overlap areas of the unmilled anode and cathode in blue. The area of the unmilled anode in combination with the milled cathode is indicated in red and is much smaller, as was also shown in the calculated area size.

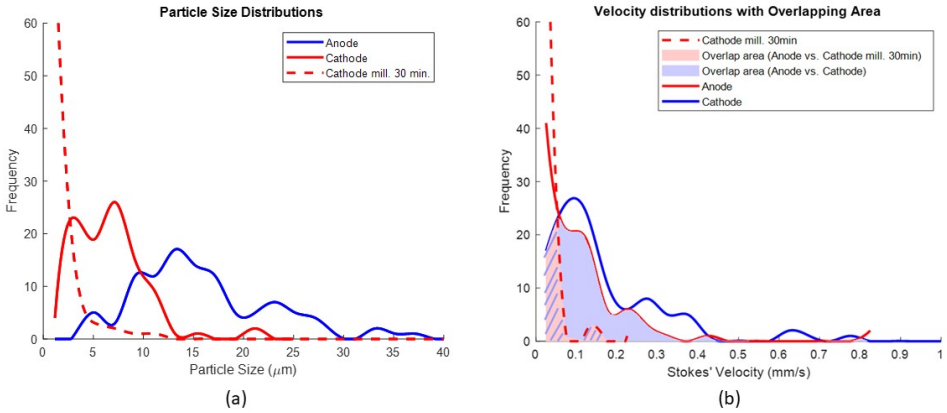

Figure 2.7: (a) Particle size distribution of unmilled Anode and Cathode, and 30 min. milled cathode, with a bin width of 2 μm. (b) Velocity distribution of unmilled Anode and Cathode and 30 min. milled cathode, with a bin width of 0.05 mm/s.

2.3.2. Estimating the theoretical separation efficiency

Using the analysed overlap of velocity distributions, the separation of anode and cathode material is quantified for the 'best' and 'worst' anode/cathode combination in terms of velocity distribution overlap, as was shown in Figure 2.7.

All particles exhibit a unique Stokes' velocity according to their particle size, resulting in a different settling rate in water. The relative velocities between the particles of the anode and cathode can be used to quantify the separation of these particles over a certain height.

Figure 2.8 shows a schematic of a sedimentation tube where anode particles (blue) and cathode particles (red) are suspended in water. For simplicity, we state that all particles can be separated that are found above a defined separation height, H_{sep}, that divides the sediment region from the supernatant.

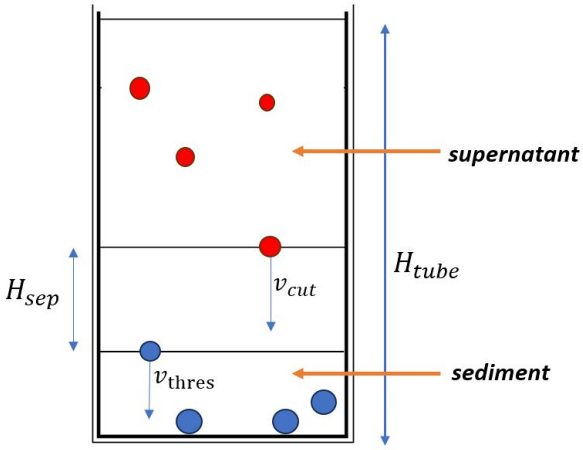

Figure 2.8: Schematic of a sedimentation tube where a mixture of anode (blue) and cathode (red) sediment in water. The tube is divided into two regions during sedimentation: the sediment at the bottom and the supernatant on top. For the model, we assume a separation height (H_{sep}) from where the two materials can be separated. We analyse what fraction of one material (red) is found in the supernatant at the moment that a 'minimum' threshold particle of the anode (blue) with velocity v_{thres} reaches the sediment.

We determine a threshold value for the particle size of the material that settles the fastest, in the schematic figure shown as the anode material with a velocity v_{thres}. This threshold particle size is used to find what fraction of the other material can be separated at a particular separation height above it when the threshold reaches the sediment. Therefore, a cut-off particle velocity, v_{cut} of the cathode material, is found for which this particle reaches the separation height. All smaller cathode particles above this separation height can be separated, as they exhibit a smaller settling velocity. The cut-off velocity can be calculated by using the velocity difference between the anode and cathode, the time it takes for the threshold particle to reach the sediment, and the defined separation height:

$$(v_{\text{thres}} - v_{\text{cut}}) * t_{\text{thres}} = H_{\text{sep}} \tag{2.2}$$

Using the size distributions of the two materials, the corresponding cut-off particle size can be calculated to find the fraction of cathode particles that are located above the separation height and, thereby, can be separated. Based on the velocity distributions, the fraction of cathode particles found in the supernatant can be used to estimate the theoretical separation efficiency of a mixture of anode and cathode material.

To quantify the potential for separation of the anode and cathode samples, we introduced a threshold value, d_{thres}, representing the minimum size of the anode sample, with a corresponding threshold velocity v_{thres}. Figure 2.9 shows again the size and velocity distributions, but now indicating the threshold values. The Standard deviation ($\mu - \sigma$) of the anode size- and velocity distribution indicates the threshold. This choice incorporates the distribution's central tendency (mean) and the spread (standard deviation) and works as a minimum value. According to the sedimentation model, 91% of the anode particles are larger and already sedimented.

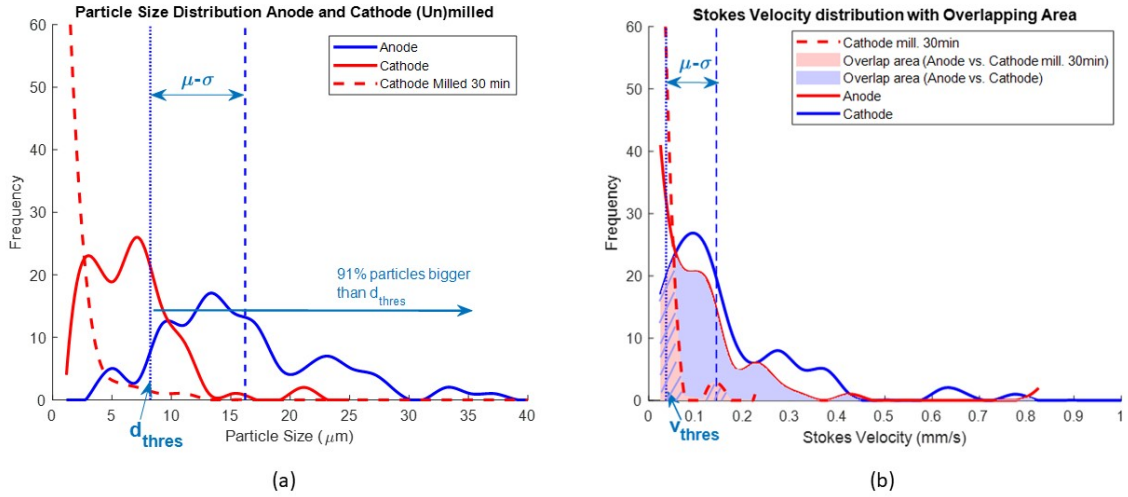

Figure 2.9: (a) Particle size distribution of unmilled Anode and Cathode, and 30 min. milled cathode, with a bin width of 2 μm. The threshold value for the anode particle size d_{thres} belongs to the smallest 9% anode particle fraction, meaning that 91% of the particles are already sedimented when this particle reaches the sediment. (b) Velocity distribution of unmilled Anode and Cathode and 30 min. milled cathode, with a bin width of 0.05 mm/s. These distributions are directly calculated from the corresponding size distributions from Figure A, using Stokes' velocities. The overlap of distributions indicates particle sizes that cannot be separated by sedimentation.

With the established threshold anode particle, Figure 2.10 presents the fraction of the cathode particles found in the supernatant after 91% of the Anode particles have reached the sediment. A comparison is made between Anode vs. Cathode and Anode vs. Cathode milled for 30 minutes. The sedimentation height varies from 50 to 1000 mm, while the chosen separation height remains constant at a chosen height of 50 mm.

The sharp increase in separation efficiency, particularly for the milled cathode, becomes evident when starting from a height of 50 mm. This is attributed to the fixed separation height of 50 mm, from where 'separation' starts, causing particles smaller than the cut-off to be found in the supernatant.

As the separation height is constant, the cathode cut-off velocity rises with increasing height. The widening distance between faster and slower (milled) particles leads to more small particles ending up in the supernatant.

The cut-off velocity of the cathode (v_{cut}) is also influenced by the separation height, which is held constant. Due to the overlap in velocity distributions, there is no velocity difference between the smallest anode particle and the cathode particle at a certain tube length just above the cut-off size. This leads to a maximum number of cathode particles in the supernatant with a smaller velocity than the minimum anode particle. As indicated by a dotted line in Figure 2.10, this maximum tube height is 625 mm for Anode & cathode and 280 mm for a suspension consisting of anode & milled cathode.

For these sedimentation heights, a theoretical maximum separation efficiency of 28% could be achieved for unmilled anode & cathode. By grinding the cathode, an efficiency of 91% could be achieved, as shown for the combination anode & milled cathode.

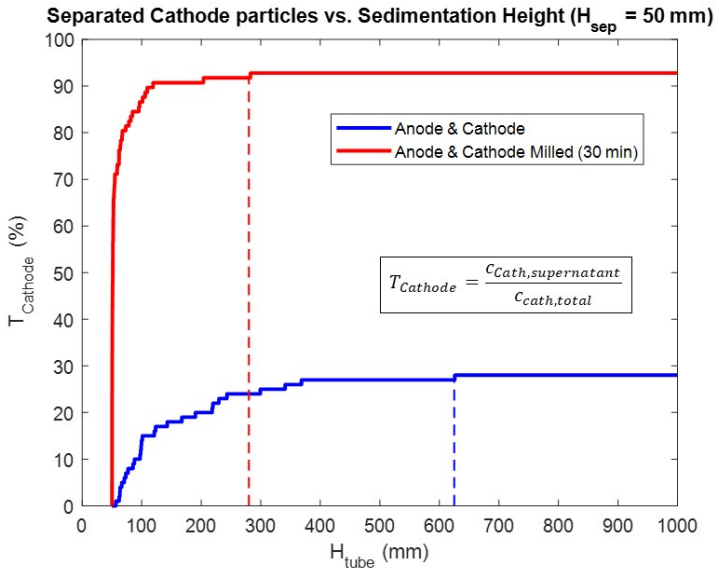

Figure 2.10: Theoretical Separation Efficiency as a function of tube length. It shows the separation of cathode particles in the supernatant after the sedimentation of 91% of the anode particles. Two combinations (best and worst case) are outlined. Milling the cathode material significantly reduces particle size, increasing the separation efficiency of cathode material: more of the milled cathode particles remain in the supernatant, while most anode particles reach the sediment, resulting in a maximum separation efficiency of 91 %. For unmilled anode and cathode, only a separation efficiency of 28 % can be achieved as a larger fraction of the cathode particles already reached the sediment together with the anode particles and, therefore, cannot be separated. The dotted vertical lines correspond to the height at which the maximum efficiency would be reached.

3

Tracking the sedimentation front of anode and cathode material

In Chapter 2, the theoretical potential for sedimentation-based separation of anode and cathode was demonstrated by examining velocity distributions and the impact of milling on these distributions.

To investigate their actual sedimentation behaviour in water and identify differences in settling, we analyse the sedimentation process of the anode and cathode samples separately. This chapter introduces a proposed method for tracking the sedimentation process of anode and cathode material in water. The experimental setup and method of analysing sedimentation velocities are described. The results are discussed in the context of the possibility of separating the anode and cathode material and the influence of milling. We will compare the results to see if they conform to Stokes' sedimentation theory.

3.1. Method for sedimentation tracking

Experimental Setup

To characterise the sedimentation, we tracked the sedimentation front of a suspension over time. A camera was used to take pictures at a selected time interval. Figure 3.1 shows the setup in the lab where a camera is focused on tubes containing different anode and cathode suspensions.

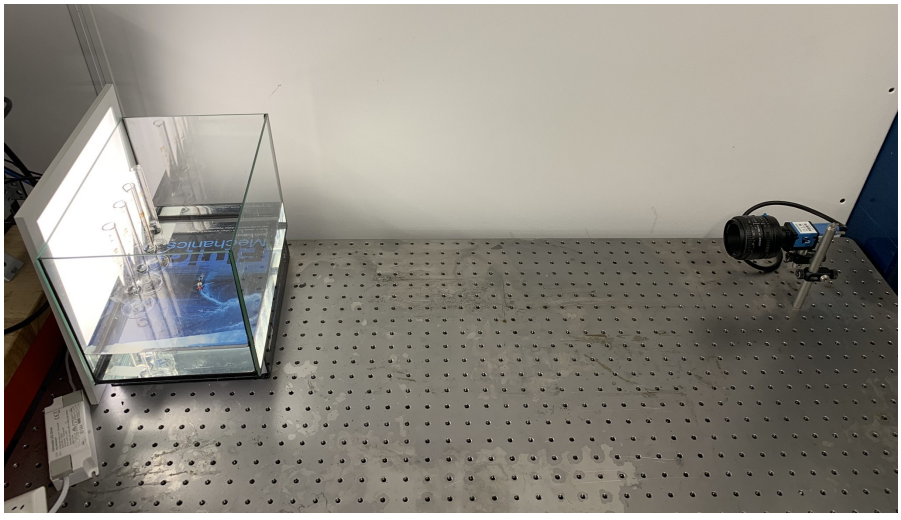

Figure 3.1: Setup of the sedimentation tracking experiments in the lab: the camera is focused on four standing tubes at a distance of approximately 60 cm. The four standing tubes are placed in a container filled with water to match the refractive index with the tubes that contain a water-based suspension with anode or cathode particles. The sedimentation process is tracked by taking pictures of the tube at predetermined time intervals.

The setup consists of a DMK 23UX174 camera with a 50 mm lens (Nikon AF 50mm f/1.8d) that takes pictures of the sedimentation tubes. These standing 10 ml glass measuring cylinders (Hirschmann) are placed approximately 60 centimetres from the camera. A 30x30 cm LED panel (4000K with dimmer driver and standard dimmer) is placed at the back to ensure contrast with the black particle suspensions. The camera is connected to the computer via a USB. IC Capture 2.5 software takes images at a given time interval and stores them. Also, the camera properties were set via this software and kept the same throughout all the experiments. The protocol for setting up an experiment to track the sedimentation process is the following:

1. Plug in the USB that connects the camera to the computer.
2. Start the IC Capture software and select the camera device.
3. Select **'Capture', 'Sequence Settings'** to choose a folder to store the images. Define the time interval of your sequence, depending on how fast the material sediments. We chose an interval between 5 seconds and 2 minutes, with a total time duration of 20 - 24 hours.
4. Select the settings **'Device', 'Properties'** to set the Exposure of the camera. Put Brightness, Contrast and Gain on 0 and Exposure on 1/30 sec.
5. Place the standing tubes in the tank in a row next to each other at the same distance from the camera and within the camera's field of view.
6. Make sure the camera is positioned right before the tubes. Change the aperture of the lens to sharpen the view of the camera.
7. Prepare the suspension: Put a weighted quantity of particle material in a glass jar with a measured amount of water for the intended concentration.
8. Mix the created suspension in the jar using a milk frother to ensure the suspension is homogeneously mixed.
9. Pour over a fraction of the suspension in a smaller glass beaker and remix the suspension.
10. Pour the well-mixed suspension into the standing tube and make sure the top of the suspension is visible in the frame of the image.
11. Select **'Snap Image'** to picture an additional image of the whole suspension right after filling the tube. This is used as a calibration image for other experiments.
12. Start the image sequence by selecting **'Sequence Timer'** (check the folder where the images are stored) and 'Start sequence'. Now, the camera takes pictures at the chosen interval, which are saved in the selected folder.

The tracking was done for around 24 hours to ensure all the particles were settled, and a complete displacement of the front was tracked. The setup allows us to see the contrast in light over the height of the tubes during sedimentation. The suspension starts to transmit more light, starting from the top, as the front of particles move down over time.

The anode and cathode material obtained from the Powerbank Li-ion battery, including the milled samples, are used for the experiments. They are introduced in Chapter 2. The measurements are conducted for all the (un)milled anode and cathode samples, where the suspension concentrations are varied between 0.25 and 2 wt.%. We were limited to these dilute suspensions as already at 1 wt. %, the suspension became opaque. At larger concentrations, a moving front of particles was barely visible. Table 3.1 shows the parameter space used for these experiments. *For example, an experiment is done for cathode material that is milled for 5 minutes having a concentration of 0.25 wt.% material in the mixed suspension.* Experiments are performed twice for each combination of material, concentration and milling for reproducibility.

Parameter	Sample
Material Type	1. Anode 2. Cathode
Concentration (wt.%)	1. 0.25 2. 0.50 3. 1.0 4. 2.0
Milling (time)	1. No milling 2. Milling (5 min.) 3. Milling (10 min.) 4. Milling (30 min)

Table 3.1: Parameter space used for sedimentation tracking experiments.

Measure the sedimentation velocity

The sequence of images from the experiments is used as input for tracking the moving front of the suspensions. The sequence was directly loaded into Matlab software to convert the images into a matrix that stores light intensity values. Figure 3.2 shows a taken picture from an experiment, which is converted into a light-intensity-based image. ImageJ software was used to obtain the pixel values from the tracked areas in the image. In Figure 3.2a, a selected area in the third tube that covers the sedimenting height range and the tube width can be seen.

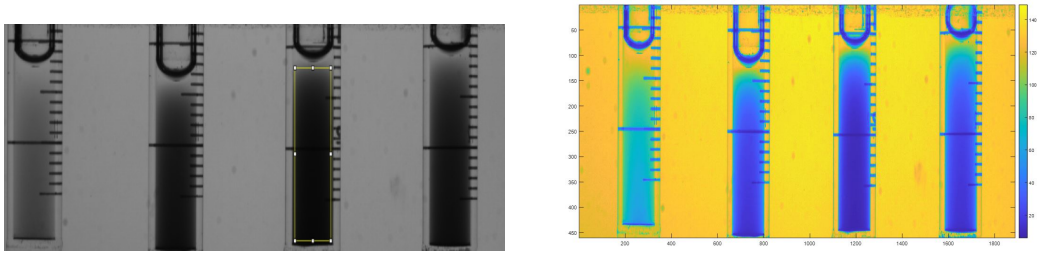

(a) Picture taken by the camera during an experiment of a 0.5 wt.% suspension of increasing milling times (left to right: unmilled, 5 min., 10 min., 30 min.).

(b) The converted image from (a) into light intensities. These values are stored over time for each tube capturing the sedimentation area.

Figure 3.2

A rectangular area was selected that covers the whole suspension surface in the tube, as shown in the third tube from the left in Figure 3.2a. Vertically, the area covers from the top, at the surface of the suspension, to the bottom of the tube. Horizontally, covering the width of the tube, the range of intensity values was averaged out. This resulted in a matrix consisting of intensity values over the sedimentation height. As the time interval between the captured images is known, an intensity plot of the sedimentation height vs. time was made to show the sedimentation process over time. An example is shown in Figure 3.3. As particles move down over time during sedimentation, the suspension starts to transmit more light from the top as a clear fluid (supernatant) region grows.

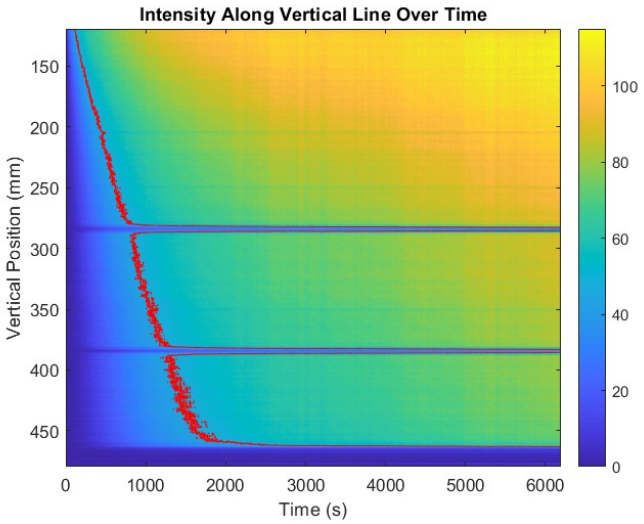

Figure 3.3: Intensity profile over time. The sedimentation process of a suspension where the light intensities are shown over the height of the tube (y-axis) and time (x-axis). At the start of the experiment, low and constant intensity values corresponding to the opaque homogeneously mixed suspension were found. Over time, higher intensities were first seen at the top of the tube as particles moved down until all particles had settled, and a constant high light intensity was seen over the tube. The small red dots correspond to the chosen threshold values. The horizontal lines crossing in the middle of the plot correspond to the black scale lines on the glass tube.

Tracking the interface velocity

The method proposed by Davis et al. [19] is applied to track the interface velocity of the moving front. As discussed in Section 1.2.5, an interface is formed during sedimentation. It separates the clear fluid from the bulk suspension, shown in Figure 3.4. This interface changes in shape throughout the sedimentation process, and therefore, the rate of fall of this interface does not have one unique value. Davis et al. (1987) argue that by focusing on the location at the interface where ϕ=0.5ϕ_0, the rate of fall of this iso-concentration plane can be used as an indicator of the overall sedimentation behaviour of the suspension [19]. This ”Interface Median Velocity” is determined by the location within the interface where the particle volume fraction equals half the initial volume fraction in the bulk suspension, as shown in Figure 3.4. It is shown that the interface median velocity of a polydisperse suspension, with a narrowly Gaussian distribution, is nearly identical to the hindered settling velocity of a monodisperse suspension with all particles having the polydisperse median particle size.

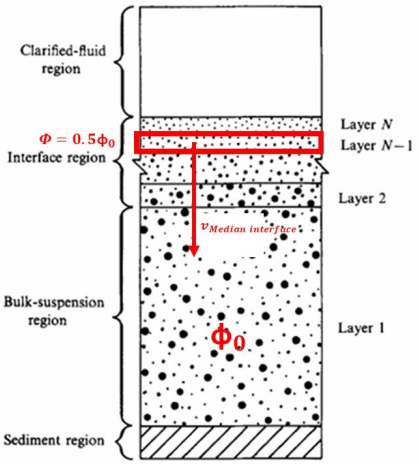

Figure 3.4: Schematic of the different regions formed during sedimentation of a polydisperse suspension in a tank with a fixed bottom and vertical side walls. The interface that separates the clear fluid region ($\phi = 0$ from the bulk suspension (ϕ_0) is, in practice, a region on its own. The median interface velocity is tracked by tracking the area layer having a volume fraction that is half the bulk volume fraction, as indicated in red.

Tracking the interface median velocity allows for a consistent comparison at different concentrations. It provides a reference point considering the changing particle size distribution and the hindered settling effect. As this median interface velocity is based on tracking the region with half the initial volume fraction of the suspension ($\phi = 0.5\phi_0$), we use the light intensity that corresponds to half the volume fraction as the corresponding threshold value to track from our intensity plot. To find this threshold value, the initial light intensity over the bulk suspension of a similar suspension (same material, same milling time) but with half the volume fraction is measured by making a calibration image just after pouring in the mixed suspension. In that way, the volume fraction is converted to a corresponding light intensity value. The threshold intensity value was obtained using again the rectangular area over the whole suspension tube from the calibration image. As there was still some variation of light intensity over the tube height, both the minimum and maximum values were used as threshold values to track over time.

The progression of the threshold value from a half-volume fraction experiment is shown in Figure 3.3. We can see that this threshold value progresses downwards over time: connecting these values, we find a line corresponding to the interface velocity. Matlab draws a regression line based on the least square method through the points, as shown in Figure 3.5. This results in two sedimentation velocities per experiment, performed for the maximum and minimum threshold values.

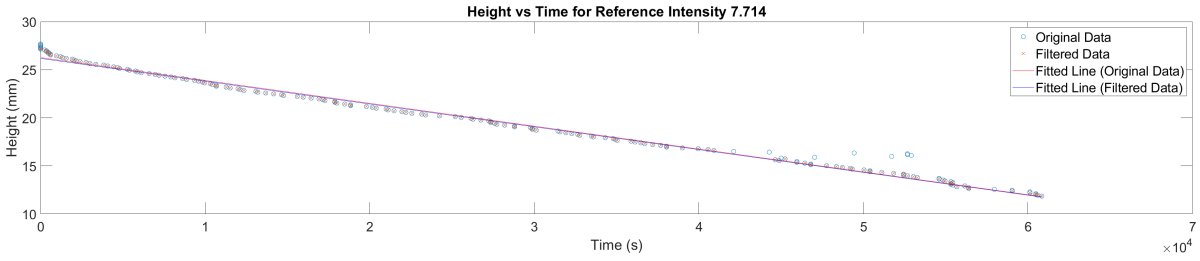

Figure 3.5: The progression of the reference intensity over time is used to track the sedimentation velocity by drawing a linear regression line through the points.

By tracking the light intensity corresponding to the bulk concentration of a suspension with half the volume fraction, we assume linearity between the light absorption and the particle concentration. According to Lambert-Beer's law, light absorbance is proportional to particle concentration, where the correlation between the two depends on the absorbtivity of the material, the tube width, and the particle size. The measured intensity is linearly related to the concentration in the dilute limit up to a particular minimal concentration. However, at higher concentrations, the linearity no longer holds. The literature showed that using Beer's law was accurate (compared with sedimentation theory) up to a volume fraction of 3 % for bidisperse suspensions [17]. However, for increasing particle concentrations, increasing deviations from Lambert-Beer are expected [49]. As we track the interface of a suspension, we measure an already low-concentrated region of the dilute suspension. So, for low-concentrated suspensions, using the linearity to track the interface will be accurate to compare the sedimentation speed over various small concentrations.

3.2. Measured sedimentation velocities

Figure 3.6 shows the measured settling rates of the different anode and cathode samples at different concentrations. The measured values at mass fractions of 0.25, 0.5, 1.0 and 2.0 wt. % are connected with a solid line to show the effect of concentration on the velocities. The differently coloured lines correspond to the differently milled samples.

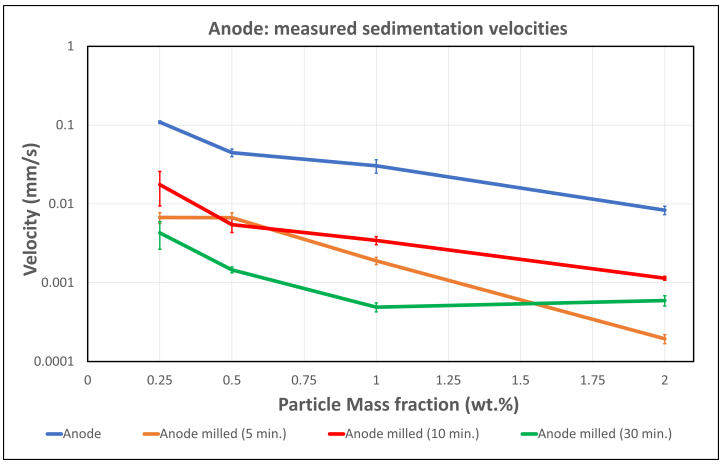

(a)

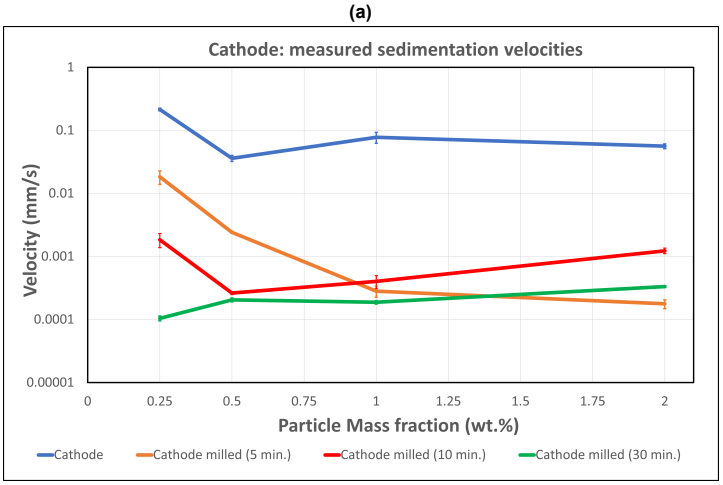

(b)

Figure 3.6: Measured sedimentation velocities from experiments for anode and cathode as a function of concentration and milling time.

Comparing the top blue line with the other coloured lines, we find that for both anode and cathode, a decrease in velocity is seen at all the concentrations. This indicates that the effect of milling the material on the sedimentation speed is strong. Looking at the anode samples in Figure 3.6a, we observe that milling for 5 minutes (yellow line) reduces the settling rate by a factor of 19 on average and for the 30 min. milled sample even up to 30 times. Overall, there is somewhat of a gradual decrease visible for the milled samples. The 30 min. milled sample exhibits the smallest velocities. Notably, the 5 min. sample shows smaller velocities compared to the 10 min. sample, differentiating more from the others at higher concentrations.

All the samples show a sort of gradual decreasing line at increasing concentrations. It can be observed that the effect of concentration on the velocity is significant for the anode material: a velocity reduction of 90% - 95% is found when comparing the 0.25 wt.% and 2.0 wt.% mass fractions of the different samples.

Notably, a significant speed decrease is measured for the highest concentrations (1.0 and 2.0 wt.%). This can be assigned to opaque suspensions at these concentrations. Therefore, very little light reached the camera detector, and hardly any light-intensity differences were measured in this darkness. It took a long time before any intensity decrease was measurable, from where the resulting velocities are much smaller than the lower concentrated suspensions. Furthermore, we find large error bars at the smallest concentrations. As those suspensions sedimented quickly, which was already noticed after a few seconds, taking the calibration image at half the volume fraction was rather difficult. Therefore, large differences in light intensity were seen through the bulk suspension from the calibration image, resulting in deviated velocities for these experiments.

These limitations were less seen for the cathode suspensions. Figure 3.6b shows the results from the measurements. It can be observed that the impact of concentration is less strong compared to the anode measurements. Only for the 5 min. milled sample, a substantial speed reduction is observed. Instead, the other samples show a relatively stable, even at some points increasing velocity over the concentrations. We find that the impact of milling is more pronounced compared to the anode samples. Milling for 5 minutes reduces velocity by a factor of 150, and the 30-minute milled sample has a 700 times lower value on average over the different concentrations. In general, the 30 min. milled sample shows the smallest velocities. However, the differently milled samples show a more similar velocity than the anode-milled material. Only for 0.25 wt.%, a notable difference in speed is visible, around a factor of 10. For larger concentrations, the samples show more similar sedimentation speeds.

3.3. Comparing sedimentation theory with measurements

As we know the particle size distributions for the different samples that we have measured, we can find how well the measurements of the anode and cathode materials strike with the sedimentation theory. Two approaches using Stokes' formula are introduced. Both are based on the volume fraction of each size class from the particle size distributions of the samples. After that, these predictions are compared with the measured velocities.

3.3.1. Methods to predict the sedimentation velocity

Average velocity from volume fraction

We can obtain the Stokes ' settling speed as a value per size class from the particle size distributions where the particles are divided into j particle classes. As each class i exhibits an average particle size a_i and frequency of counted particles f_i, we account for each particle class's volume fraction ϕ_i. The volume fraction of a size class i is calculated based on the total volume fraction (ϕ) by dividing by the total volume (the sum of all the size class particle volumes):

$$\phi_i = \frac{a_i^3 f_i}{\sum_j a_j^3 f_j} \tag{3.1}$$

The particles' volume scales with the size to the power 3 and the frequency of the particles in that size class. We can use the volume fraction and the Stokes' velocity per size class to obtain an average velocity from the size distributions. By taking the sum of the settling velocities of each size class v_i and multiplying by the corresponding volume fraction of that size class ϕ_i, we obtain the average settling velocity based on the volume fractions of the size distribution:

$$\langle v \rangle = \sum_i \phi_i v_{i,stokes} \tag{3.2}$$

The median particle size

Another approach to estimating a value for velocity from the size distributions is to use the median particle size based on the volume fractions of the size classes. It is found at 50% of the total particle volume fraction, summed up from the fractions of each size class.

As an example, the sample "Anode milled (5 min.)" is shown in Figure 3.7. It shows the histogram of the 'anode milled 5 min.' sample, corresponding to the blue bins. The counted particles are stored in size ranges to create the bins. The volume fraction of each size class is shown by the orange line and is calculated using Equation 3.1. As the volume of spherical particles is proportional to the particle size to the power three, it can be seen that the larger particles occupy a much larger fraction of the total volume compared to small particles, from which the volume fraction is barely visible. Also, the accumulation of the volume fractions is shown by the green line. At the point where 50% is reached, the corresponding particle size class is found, which is the median size. In this case, 11.375 μm. We can use this median particle size for Stokes' formula. This size is much larger than the median of the particle distribution as larger particles account for a much larger fraction (size to the power 3). As we measure the interface velocity where half the volume fraction of the bulk suspension is found, it is reasonable to compare with Stokes' formula using this median particle size.

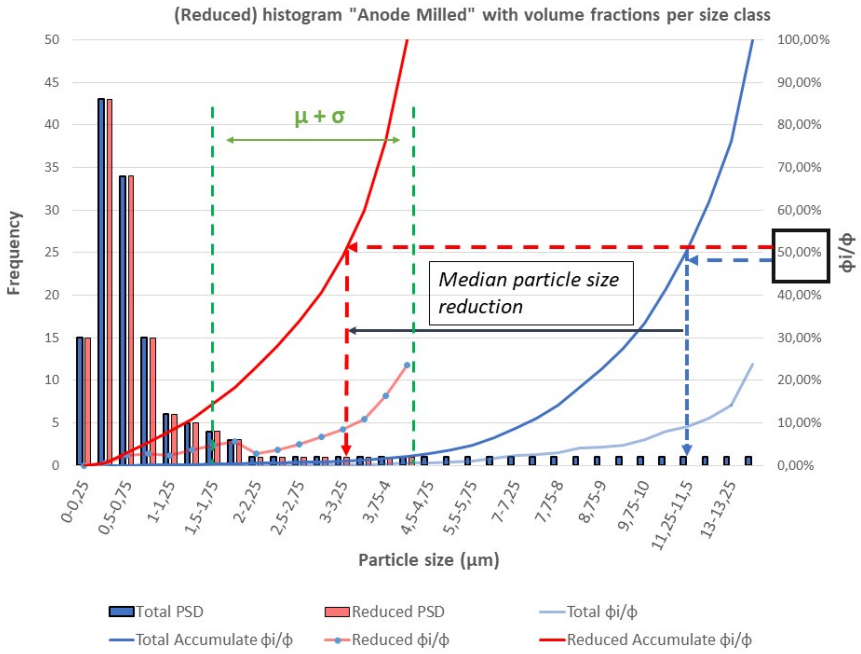

Figure 3.7: histogram of the anode 5 min. milled sample: only a few particles are found in the higher size classes (7 - 15 μm). These particles exhibit a large fraction of the local volume fraction (orange line) while they sediment 50 - 225 times faster than the mean particle size of 1.6 μm. This results in a median particle size of 11.375 μm when considering all the particles. Instead, when using the range $\mu \pm \sigma$ from the size distribution, we obtain a reduced median particle size of 3.25 μm while only excluding the 8 % outliers from the distribution. This would give a better estimate of the interface velocity that we measure.

Reduced median size for better estimation

As shown in the histogram of the milled sample, the large particles also account for a large part of the volume fraction, causing a large value for the median particle size. We can ask whether this value is a viable estimation for the speed of the moving front, as the largest fraction of particles is much smaller compared to this median size. We deal primarily with size distributions where a significant fraction of particles are concentrated in very small size ranges while only a few particles are much larger. From the histogram in Figure 3.7, it is found that 80 % is smaller than 1.5 μm, while only 8% of the particles is larger than 7 μm. This small fraction of large particles exhibits a Stokes' velocity of 50 - 225 times most particles from the size distributions. In practice, the larger particles are already sediment when we track the front of the suspension. Therefore, a better estimate for the moving front of the particles is to use a reduced size distribution where we only consider the mean ± standard deviation of the milled sample distributions. This results in a smaller median particle size that includes between 90 and 93% of the particle fraction.

This is shown in Figure 3.7 for the reduced size distribution of the "anode milled 5 min." sample (in red). From there, we find a reduced median particle size of 3.25 μm, around 3.5 times smaller than the one seen from the total distribution. Using this reduced size distribution, where we remove the outliers by taking the standard deviation as the maximum, we can find a median size that better predicts the measured values from the interface velocities. Table E.3 in Appendix E provides the size distributions and a list with the calculated median sizes of all the samples based on the volume fraction and the reduced median sizes of the milled samples.

Hindered-settling
The Masliyah-Lockett-Bassoon (MLB) correlation for a polydisperse suspension accounts for the hindered settling effect for known concentrations. The hindered-settling factor is calculated for the size ranges from the distributions and is expressed as a number between 0 and 1.

A value close to 1 means almost no hindrance effects for the particles, while a small value corresponds to a significant hindrance during sedimentation. We find a larger hindered settling for the smaller particle size classes. In a polydisperse suspension, these particles sediment slower and experience more hindrance from water displaced upward due to the larger particles settling down. These larger particles experience much less hindrance as they settle much faster. The Stokes' velocities for each size class are multiplied by this hindrance factor. This is conducted for the different concentrations for which we did the experiments. We use mass fractions to create suspensions with a known concentration for practical ease. To convert these mass fractions into particle volume fractions (ϕ), we assume an average density for the anode and cathode materials (2000 kg/m^3 and 4500 kg/m^3, respectively). The steps for converting the mass fraction to volume fraction are provided in Appendix B, together with the calculated volume fractions for anode and cathode at the used concentrations for the experiments.

Appendix F provides a list of the size distributions and volume fraction per size class for all the samples. The average velocity per concentration and the corresponding hindered-settling function are provided. The hindered-settling functions are listed per concentration for the samples in Appendix F.

3.3.2. Comparing the predicted velocities with the measurements

By utilising the methods for estimating velocity based on reduced size distributions, we can compare them with the measured values to evaluate the accuracy of the sedimentation theory for these suspensions.

Anode

Figure 3.8 displays the measured velocities from the experiments for the anode in solid lines. Additionally, the predicted velocities based on the introduced average velocity, determined by the volume fraction (equation 3.2), are shown as 'Average prediction'. The velocity corresponding to the reduced median particle size is also displayed as 'Median prediction'. They are both shown as dotted lines with marked points at zero concentrations, where no hindered settling is considered. The hindered settling effect is considered at the measured concentrations using the MLB model.

We directly observe the significant difference between the measurements and predictions at higher concentrations. The predicted values reduce at higher concentrations due to hindered settling, but at maximum by only 8 - 14% in speed, which is barely visible from the log-scaled velocity axis.

As described, a strong effect of concentration on the velocity was measured for the anode material. The anode measurements in Figure 3.8 show a reduction of 84 - 97 % at the highest concentration of 2 wt.%. This reduction is massive: according to the theory, a reduction of 95% would be expected for mass fractions of 72 wt.% (36 times higher concentration). This indicates that for anode suspensions, the established sedimentation theories on hindered settling are not feasible for predicting sedimentation rates.

However, for the smallest mass fraction at 0.25 wt.%, the measured speeds align with the predictions based on the median size. At this concentration, the unmilled sample deviates by 19 % from the measurements, while the median prediction for the milled samples falls within the standard error of the measurements. For larger concentrations, this difference grows to a ratio of 14 between the median-based predictions and the measured settling rate.

Comparing the two approaches to predicting the measurements, it is observed that the two approaches give very similar results. The predictions based on the median particle size show a little smaller velocities compared to the predictions based on the average, but the deviation is only 5 - 16 %. The velocity reduction over the concentrations is equal, as the hindered-settling functions per size class are used similarly for both approaches. This indicates that using the reduced particle size distribution for the average and median velocity gives a good representation of the average velocity of an anode suspension.

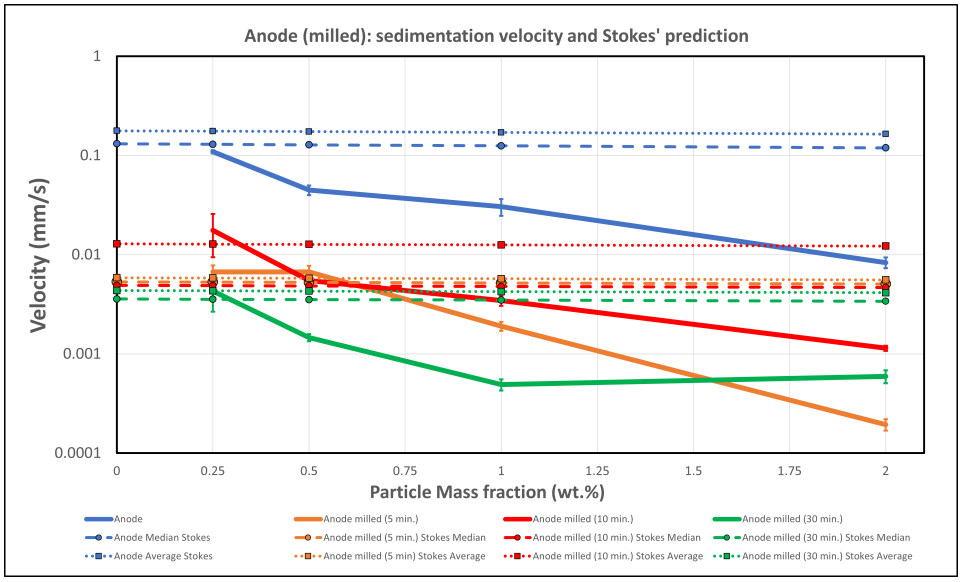

Figure 3.8: Measurements and predictions for sedimentation of the anode samples. The predictions show a much weaker effect on the velocity for larger concentrations than the measurements. A large difference between them is found and more pronounced for higher concentrations.

Cathode

Figure 3.9 shows the measurements and predictions for the cathode samples. Comparing the measurements with the predictions, we see that the unmilled sample (blue) aligns more with the expected velocity values (dotted blue line). The maximum difference is found at 0.25 wt. % where the Stokes prediction is 3 times larger compared to the average measured value. Similar to the anode, we find that the prediction conforms better to the measurements for the smallest concentrations. When sample velocities start to decrease for increasing concentrations, the deviation between prediction and measurement grows, as is seen most pronounced for the 5 min. sample. As the 5 min. milled sample decreases enormously for larger concentrations, a large difference with a ratio of up to 82 between the predictions and the measurements is found. Except for the 5 min. milled sample (orange), we see that the other milling samples are more in line with the predictions. On average, a ratio of 1.3 between the measured and predicted speed is found.

As for the anode, the theory for hindered settling gives a much weaker dependence on solid fraction than observed in the experiments and, therefore, mainly a higher velocity than measured from the experiments. However, as the influence of concentration on the settling rate for the cathode is also weaker compared to the anode, the measurements are more in line with the predicted velocities compared to the anode. For both the anode and cathode, we observe that the measurements conform to the theoretical predictions for the most dilute suspension (0.25 wt.%).

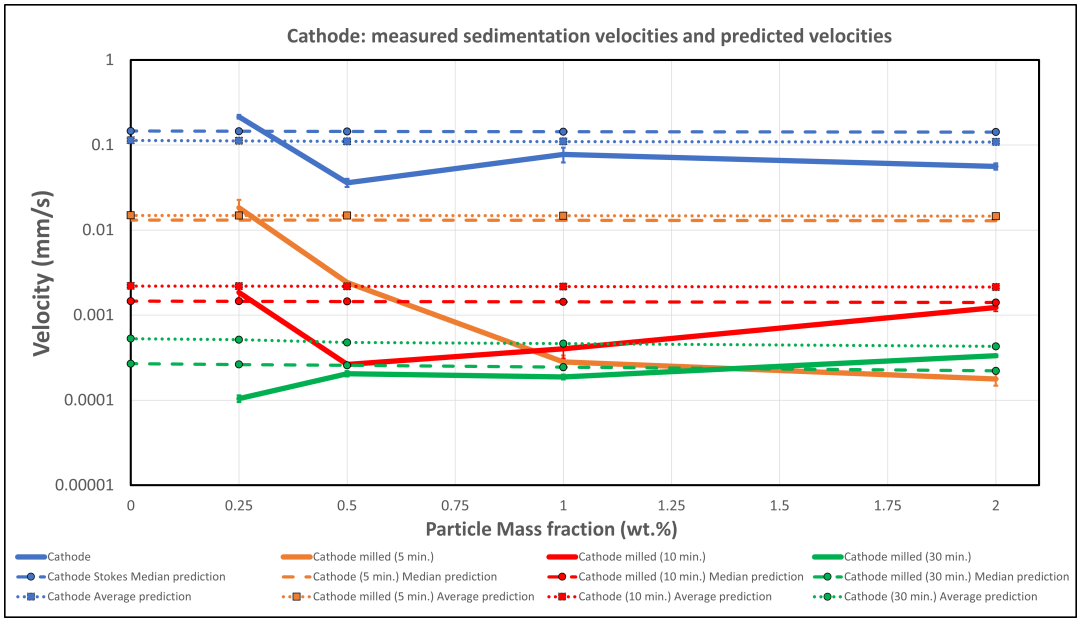

Figure 3.9: Measurements and predictions for sedimentation of the cathode samples. The measurements are mostly in line with the theory for the very dilute suspensions. More deviations are seen between the measurements and the predictions for higher concentrations.

Discussion comparing anode and cathode with theory

Comparing the anode and cathode velocity measurements with the theory, we can conclude that predicting the sedimentation speed according to an analytical model for sedimentation does not match most of the measured sedimentation velocities. Only for the very low concentrations (0.25 wt.%) the measurements are in line with the theoretical predictions for both the anode and cathode. The differences with the theory seem less pronounced for the cathode, as the effect of concentration on the velocity is less extreme compared to the anode. Substantial differences are found for the anode, which increases at higher concentrations.

From the experiments on higher concentrations (> 1 wt.%), it was seen that the anode suspensions were very opaque, and a change in light intensity was barely measurable as it reached its minimum value from what was measurable from the light contrast. Therefore, very low sedimentation speeds were measured compared to the smallest concentrations where the suspension sedimented relatively fast and a large decrease in the sedimentation speed over the concentrations was measured.

The sedimentation behaviour of these particles does not match the expected velocities according to their initial size distributions before sedimentation in water. We see that the predictions show constantly higher values for the speed than what is measured. It could be that contact with water of the anode affects the morphology of the particles and thereby changes the size distributions. However, it would be expected that graphite mostly aggregates in water, forming larger agglomerated particles that would sediment faster according to sedimentation theory [72]. NMC particles from the cathode could partly dissolve in water. Lithium could leach out, and nickel oxides are easily dissolvable in water, resulting in smaller cathode particles than we saw from the material before processing it in water [4]. This would result in a lower sedimentation velocity than expected from the initial size distribution. The effect of contact with water on these materials is further discussed in Chapter 4, where the suspension after sedimentation is analysed using Scanning electron microscopy (SEM).

4

Sediment analysis of mixed Anode and Cathode

A new method for analysing the structure of sedimented material is proposed. It involves separating horizontal layers of accumulated sediment at the bottom of a tube to determine the location of the anode and cathode material after settling by gravity in water.

The composition of the sediment as a function of height is of interest because the difference in sedimentation velocity between particles is the primary factor affecting the particle location in the sediment. The main challenge in characterising sediment structure is extracting sediment from the sedimentation tube without disrupting its accumulated structure.

This chapter presents a newly proposed method for acquiring sediment layers, which are then characterised using Inductively Coupled Plasma - Optical Emission Spectroscopy (ICP-OES), Scanning Electron Microscopy (SEM) and Thermogravimetric Analysis (TGA). The results provide information on the elemental distribution of elements throughout the sediment and how sedimentation in water affects particle morphology. The TGA analysis is conducted using a mixture of pristine graphite and lithium-iron-phosphate (LFP). It aims to evaluate the potential of this technique to characterise an anode-cathode mixture.

4.1. Obtain layers of sedimented material by freezing

A suspension of anode and cathode with a 50:50 mass ratio is homogeneously mixed and poured into a 5 ml plastic syringe. The syringe is cut open at the top, as illustrated in Figure 4.1a. The syringes have a height of approximately 40 mm and an inner diameter of 20 mm. About 0.4 grams of anode and cathode material are suspended in water, resulting in a particle mass fraction of approximately 15 wt.%. This mass fraction has been chosen for practical reasons to ensure a significant sediment height, making it easier to cut layers. The suspension is then left undisturbed for 24 hours to allow complete sedimentation. As can be seen from Figure 4.1a, after 24 hours, most of the particles are concentrated at the bottom, the sediment, while a more transparent liquid is seen at the top. The syringes are securely stored in sample holders to prevent disturbance of the sedimentation process.

After sedimentation, the syringe is placed in a freezer for 2-3 hours at -20 °C, resulting in a frozen cylindrical block of sediment inside the syringe, as shown in Figure 4.1b.

The frozen sediment block is pushed upwards through the open top by moving the syringe's plunger. To facilitate the controlled ascent of the frozen block, a minimal amount of boiled water is poured over the syringe's outer sides to melt the edges of the sediment at the wall locally. This process ensures that the sediment is pushed upward while preserving its structure. Horizontal cuts are made on the frozen sediment at measured heights using a Weller Craft knife. Firstly, the top part is cut off, which is the frozen liquid. This is typically the largest part in height, with a height of around 20 mm, containing the lowest particle fraction of around 8 wt.%.

Following this, three layers of equal height of around 2 - 3 mm are cut from the frozen sediment. After each cut, the top is locally frozen again using liquid nitrogen to maintain the sediment's structure.

The resulting frozen layers are stored separately in Petri dishes (Figure 4.1c) and are then placed in an oven at 60 °C for 2 hours to remove the water content. The resulting dried powders, depicted in Figure 4.1d, are weighted and stored for further characterisation. To ensure reproducibility and assess the reliability and consistency of this method, we characterised two similar suspensions that underwent the process of freezing and layer separation.

Traces of melted suspension can be seen around the Petri dishes in Figure 4.1c. Around 10% of the initial mass of material used in the suspension was lost after weighting the dried mass of the layers. Local melting of the frozen sediment during the layer extraction process mainly contributed to these losses. The melted liquid suspension adheres to the plastic walls of the syringe, sticks to the top of the plunger at the bottom of the sediment, and to the knife when cutting the layers.

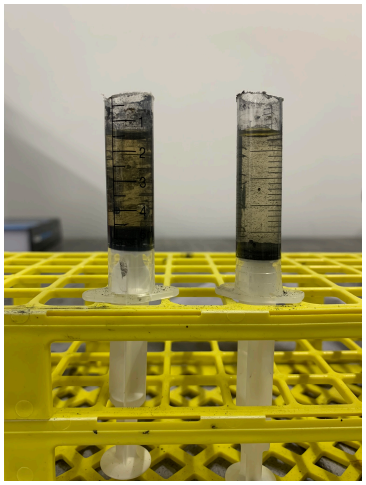

(a) Syringes containing sedimented material at the bottom and a clear fluid (supernatant) on top, after leaving them for 24 hours. The syringes are kept in place in the sample holder to ensure no disturbance of the structure of the loose sediment.

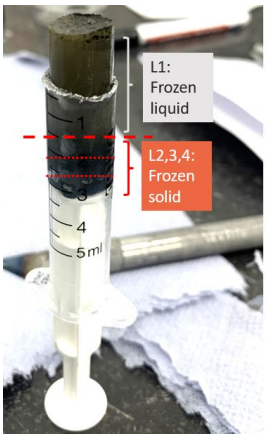

(b) The frozen sediment is pushed up to be cut off horizontally and is divided into 4 layers. The first cut is made at the interface between the frozen liquid and the frozen sediment to obtain Layer 1 as the frozen liquid. Then, the frozen sediment is divided into 3 layers (Layers 2, 3 and 4).

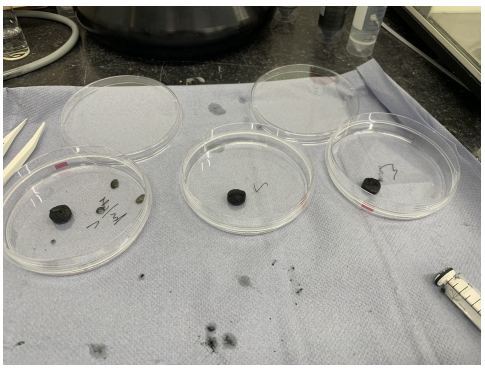

(c) The cut layers are separated and stored in Petri dishes.

(d) After drying the obtained layers in an oven, the powders are used for further characterisation.

Figure 4.1: Consecutive steps of the methodology to collect and characterise the undisturbed sediment by freezing and horizontal sectioning of layers.

4.2. Elemental composition sediment layers

Inductively Coupled Plasma-Optical Emission Spectroscopy (ICP-OES) analysis is used to characterise the horizontal sediment layers of the anode/cathode suspension. ICP was conducted using the Spectro Arcos EOP. Samples were dissolved in a solution containing 35% nitric acid (HNO_3) and subsequently mixed with hydrogen peroxide (H_2O_2) twice. The resulting mixture was allowed to stand for several days with occasional agitation. Subsequently, the clear liquid phase was subjected to ICP measurement.

This method was employed to find the anode and cathode materials distribution within the sediment. The ICP-OES analysis provides the local elemental composition of each sample layer. As seen in Chapter 2, the composition of anode and cathode consists of a large mass fraction that ICP cannot measure: in the anode due to the high carbon content and in the cathode primarily due to the present metal oxides. Comparing elemental fractions for a mixture of anode and cathode is not straightforward, as assigning an elemental fraction entirely to one of the materials is not possible. Therefore, we concentrated on the primary metal fraction of the cathode in each layer, which comprises Ni, Mn, and Co, to determine the distribution of these materials throughout the sediment. This would provide insight into the location of most of the cathode material within the sediment.

Four suspension layers were analysed: The frozen liquid (supernatant) at the top (layer 1) and three equally divided layers from the sediment at the bottom (layers 2, 3, 4).

The as-received results from ICP-OES are shown in figure 4.2, where a gradual increase of the metal fraction is observed from the top (layer 1) to the bottom (layer 4) of the sediment structure. Table 4.1 also shows the deviations of the measured metallic fractions. A small deviation over the two reproduced experiments indicates that freezing the suspensions results in a consistent elemental composition for the sediment layers. The (a.r.) ICP-OES results of the four layers of both experiments, including all fractions of the measured elements, can be found in Table D.2 in Appendix D.

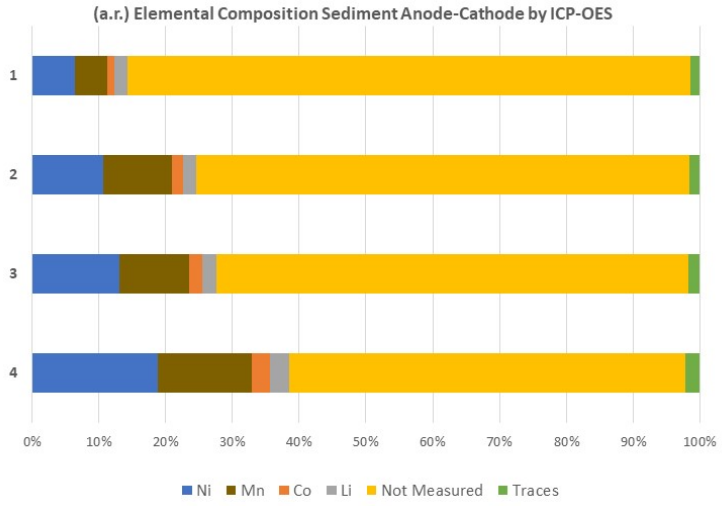

Figure 4.2: (a). Average elemental composition over two measurements by ICP-OES analysis. 'Not measured' includes mainly oxygen from the cathode and graphite (carbon) from the anode component. 'Traces' here include elements with a mass fraction of less than 0.5 wt.% and can be found in Appendix D.

	Sum Ni+Mn+Co mass fractions by ICP-OES	
Layer	Average	Standard deviation
1	11.5%	0.92%
2	22.6%	1.60%
3	25.4%	3.12%
4	35.6%	1.11%

Table 4.1: Average Ni+ Mn + Co content sediment with standard deviations from two experiments

Mass balance sediment structure

The metal compositions of the 4 suspension layers, received from ICP-OES measurements, were used to conduct a mass balance analysis of the structure of the suspension. This analysis determined the distribution of the measured elements throughout the suspension, considering each layer's mass fraction. Figure 4.3 displays the overall mass balance of the sedimented suspension, consisting of the supernatant (Layer 1, the frozen liquid) and the sediment (Layer 2, 3 and 4). The solid mass fraction of the sample layers after drying is shown in Column (a). Most particles (92 wt.% of the total particle mass) are concentrated at the bottom of the suspension. After sedimentation, the supernatant at the top appeared almost transparent, as most particles were settled. However, after drying, a significant fraction of the particles (8.4 wt.%) was still measured in layer 1. A gradual decrease in mass distribution is visible, with a larger mass fraction in the lower parts of the sediment. This can be explained by the sedimentation process, where bigger and denser particles sediment faster and, therefore, can be found at the bottom of the sediment.

Column (b) in Figure 4.3 shows the (as received) measured metal fraction (Ni + Mn + Co) of the sample layers from the ICP-OES analysis, with the metallic fractions as they where shown in Table 4.1.

The bottom layer exhibits the highest fraction of metals, which can be linked to the higher mass of this layer, as metallic compounds are much denser than the carbon and lithium content. The results show a gradual increase in the metallic fraction from top to bottom. However, the information provided in Column (b) only represents the composition in one layer without considering the fraction of this sample in the whole sediment. To gain insight into the sediment structure, it is more useful to examine the distribution of this metallic fraction across all layers, as seen in Column (c). Therefore, the metal mass fraction is multiplied by the mass fraction of each corresponding layer, resulting in the weight fraction of the metal components in the layers. Column (c) shows that a small fraction of cathode material is concentrated at the top layer and gradually increases towards the bottom, indicating a degree of separation throughout the suspension. The top layer, known as the supernatant, contains a very small amount of metallic compounds. Only 1% of the metals, consisting of Ni, Mn, and Co compounds, are concentrated in this layer. The bottom layer has the highest concentration of cathode metallic compounds with a fraction of 15.8 %. Layers 2 and 3 have intermediate concentrations, with layer 3 having slightly more metals than layer 2.

Column (c) sums up a total metallic fraction of 28 wt% throughout all the layers. This value is as would be expected from a 50:50 anode/cathode mixture where around 54 wt.% of the cathode components consist of Ni, Mn and Co, as was shown in Figure 2.2 in Chapter 2.

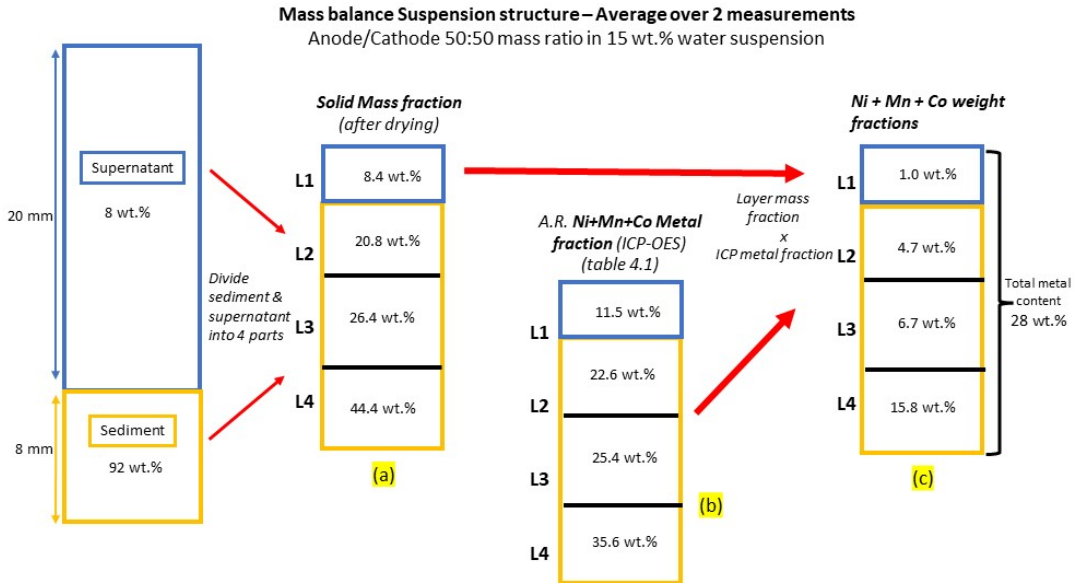

Figure 4.3: Anode-cathode mass balance sediment mixture after sedimentation: the frozen suspension is divided into 4 layers (L1, 2, 3, 4). After drying, the samples are weighed. Their mass fractions are given in Column (a). These layers are characterised by ICP analysis. The measured sum of metallic compounds attributable to cathode material is given in Column (b). Multiplying (a) and (b) gives the weight fractions of the metallic components. The total metallic fraction adds up to 28 %, which corresponds to 54% of the cathode mass, considering the 50:50 anode/cathode mass ratio.

4.3. Particle morphology throughout sediment layers

In addition to quantitative analysis by ICP-OES, Scanning Electron Microscopy (SEM) imaging is used to qualitatively study the spreading of anode and cathode material throughout the sediment layers and to analyse the particle morphology of the anode/cathode mixture after processing in water. Therefore, this section analyses and compares the top layer of the supernatant (Layer 1) and the bottom layer of the sediment (layer 4).

Figure 4.4 shows SEM images of the top layer of the sediment. Many typical spheroidized graphite particles and some spherical NMC particles are well-dispersed throughout the sample. These particles, with a size of 5 - 30 μm, were also seen in the original anode and cathode samples before processing in water. Also, a few bigger compacted agglomerated particles are present with a size of 50 - 100 μm, indicated in red. They contain mostly graphite and some clustered NMC particles.

Figure 4.5 shows images of the sediment's bottom layer (L4). The zoomed-out image in Figure 4.5a reveals numerous large and coarse blocks of compacted agglomerated particles. Those agglomerated blocks exhibit a large size of around 100 - 500 μm and mainly consist of graphite particles, as can be seen from the layered structure of those blocks, indicated in red. These compacted and large agglomerated particles were not found in the original anode and cathode samples before processing in water, indicating that contact with water somehow affects these materials. The formation of agglomerated particles in water could be explained by the hydrophobic nature of graphite [72]. A few of the compacted blocks, in Figure 4.5b zoomed in on one, show agglomeration of both graphite and NMC particles, with many smaller particles at the surface of these agglomerates. Aqueous processing of NMC particles causes the intergranular fracture of NMC cathode particles, where secondary NMC particles break into smaller irregular agglomerates or individual submicron primary particles [4]. These smaller particles could be assigned in part to NMC cathode particles. In literature, it is discussed that the dissolution of Nickel oxides and leaching of lithium into LiOH and Li_2CO_3 can leave smaller crystallised structures on the surface of NMC particles in water [31].

As indicated in blue, the compacted agglomerates are surrounded by smaller individual graphite and NMC particles, recognisable from the original anode and cathode SEM images that were shown in Figure 2.3, Chapter 2.

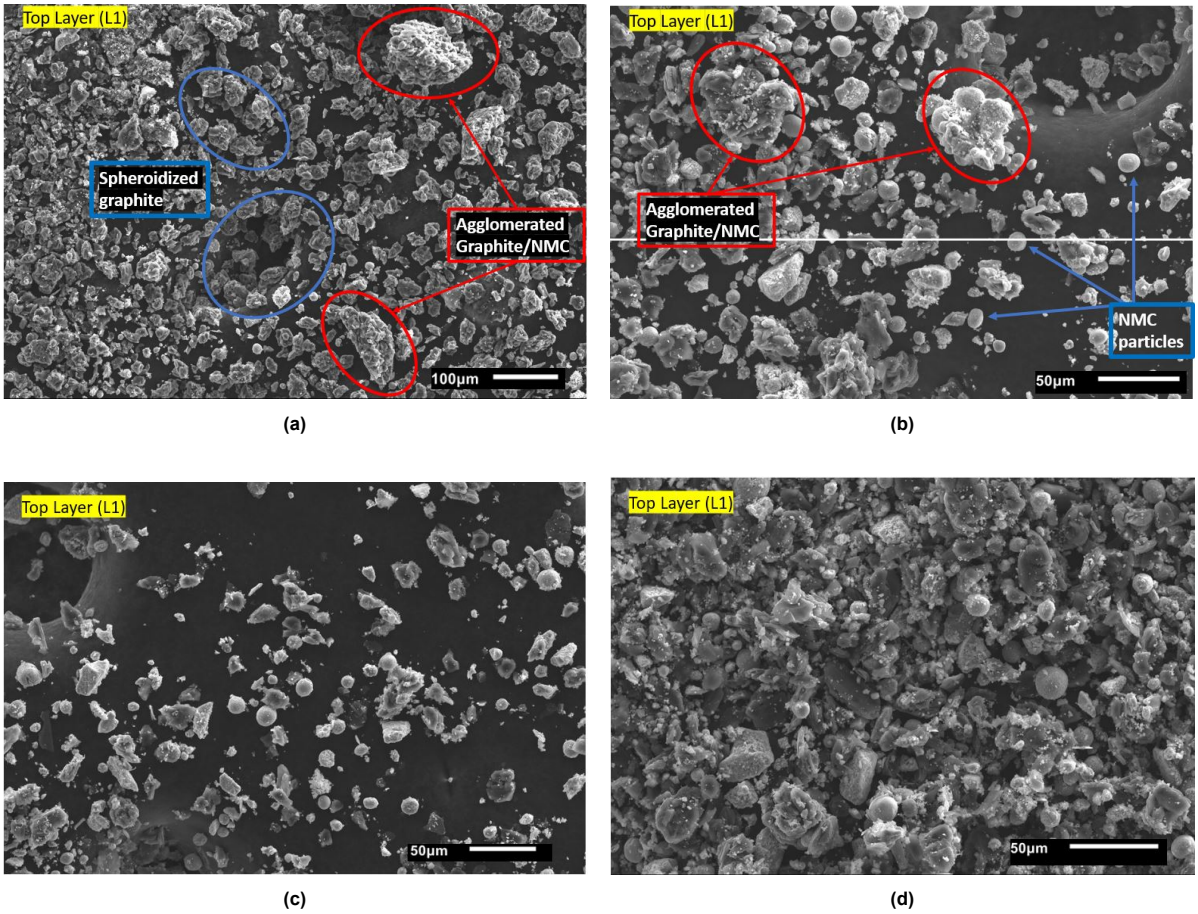

Figure 4.4: SEM images of the supernatant region (layer 1) of the sample. Mainly, original spheroidized graphite particles and NMC are found dispersed throughout the sample.

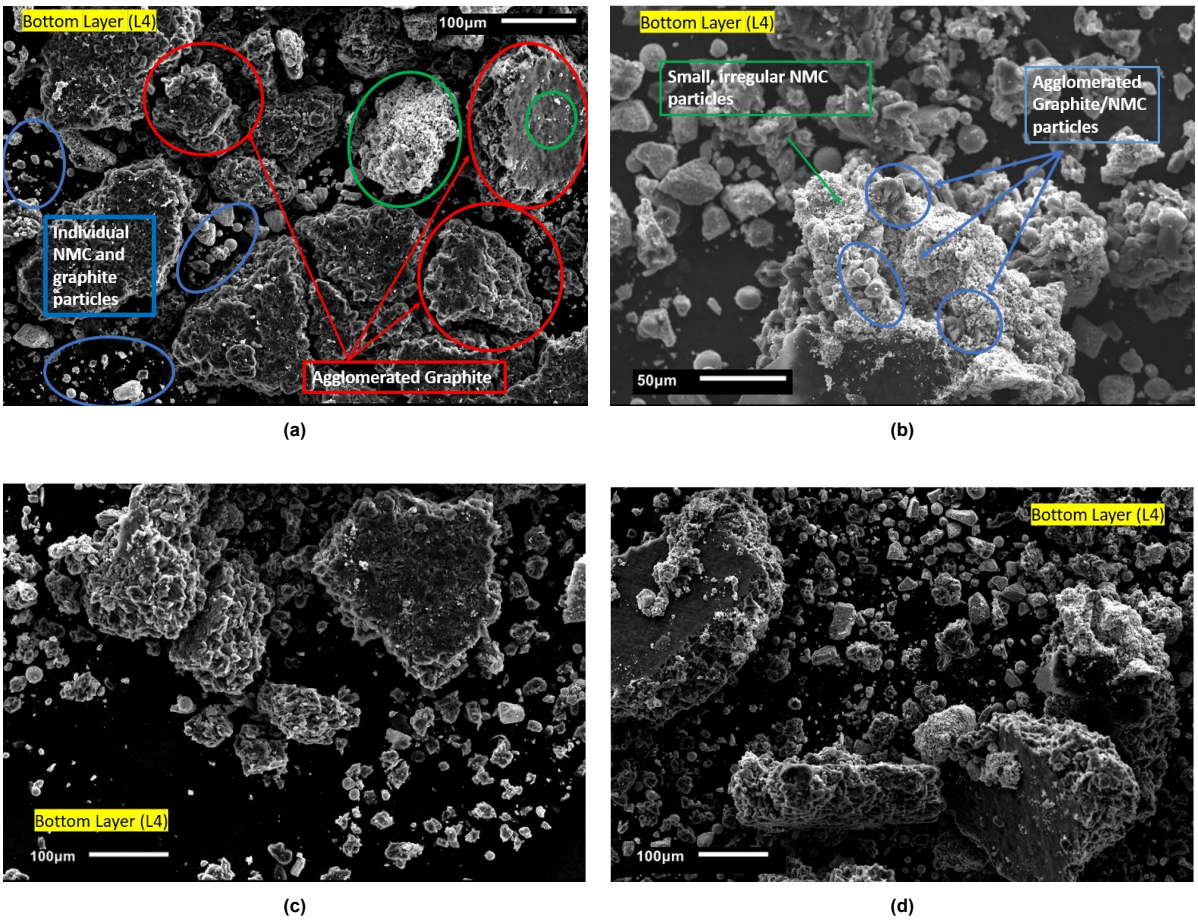

Figure 4.5: SEM images of the bottom layer (layer 4) of sediment after sedimentation. Many large compacted agglomerates are found here. Mainly, the graphite particles agglomerate, while small irregularly shaped NMC particles are located on the surface of these agglomerates, as seen in figure (b).

4.4. Discussion SEM and ICP-OES results

The mass balance and the corresponding SEM analysis showed substantial composition and particle morphology differences among the distinct sediment layers. We found that the cathode material is increasingly concentrated towards the bottom layers of the sediment, while mostly graphite particles are found in the supernatant (top layer) after sedimentation.

The mass balance of the suspension showed the distribution of the metallic fraction throughout the layers. It was seen that the supernatant (layer 1) exhibits a metallic fraction of 11.5 wt.%. When accounting for the mass fraction of this top layer (8.4 wt.%), we find that only 1.0 wt.% of the metals are concentrated in this top layer. Assuming that the cathode particle elemental composition is conserved during sedimentation and knowing that the Ni, Mn, and Co content is approximately half the mass of the cathode material (54 wt.%), it would mean that roughly 2 wt.% of the cathode material is located in layer 1. This is in line with what was seen from the SEM images of layer 1. The top layer exhibits dominantly individual graphite particles with their typical spheroidized structure and a few original cathode spherical NMC particles that are well dispersed with a size of 10 - 50 μm. It would be suggested to further process this top layer sample for direct recycling, as this top layer shows the best separation of the anode and cathode particles. One could apply a step of further separation (by centrifugation of froth flotation) to remove the small fraction of cathode particles and recover the well-defined grains of graphite and NMC.

The distribution of metallic components indicates that approximately 16% of the metallic fraction is concentrated in the bottom layer. This would roughly mean that 32 wt.% of the layer consists of cathode material. This means this layer is still thoroughly mixed with anode and cathode particles. Due to their higher density, the cathode particles could be pressed through the top layers of the sediment (layers 2 and 3) to end up at the bottom. This could explain the higher concentration of NMC metal components in this layer. The bottom layer is the most densely packed, containing almost half the total particle mass from the suspension. As seen from the SEM images, the bottom layer contains almost exclusively very coarse compacted agglomerates of mostly graphite with some clustered NMC particles. In line with sedimentation theory, we would expect that these large agglomerates are mostly found at the bottom of the sediment as they are bigger and denser and, therefore, would sediment faster. Studies on froth flotation showed the tendency to agglomerate of both graphite and NMC when suspended in water with sizes of around 30 - 100 μm, and the entrapment of smaller NMC particles inside large graphite agglomerates from suspending graphite and NMC in water [66]. From the SEM images, we also find agglomerates mainly consisting of compacted graphite with some clustered spherical NMC particles that could be entrapped inside these agglomerates. Instead, these agglomerates exhibit a much larger size of around 100 - 500 μm. Besides the agglomerated particles, some original graphite and NMC grains are visible, which are recognised from the anode and cathode samples before processing in water. The observation of significantly larger agglomerates provides valuable insights into the interaction of water with graphite and NMC particles. Furthermore, it complicates the prediction of sedimentation rates for these materials, as sedimentation is typically dependent on particle size, making it challenging to predict the behaviour of these materials in aqueous environments accurately. To recycle the grains from the bottom layer, they should be processed with intense shear to break up the agglomerated material. Leaching metals out of a compacted agglomerate would be ineffective due to mass transfer limitations, as the solvent may not penetrate the agglomerate. After that, further separation would be necessary to recover separated grains of NMC and graphite.

4.5. Sediment characterisation using Thermogravimetric Analysis (TGA)

Thermogravimetric Analysis (TGA) is another technique explored for characterising the black mass mixtures of battery materials. TGA is a well-known characterisation method that measures a sample's thermal stability and mass changes as a function of temperature and time [52].

Using TGA, we can obtain information about the thermal stability of an anode-cathode mixture under a certain gas environment. As shown by Gomez-Moreno et al. (2023), TGA analysis is a promising method for estimating the graphite content of a typical anode-cathode mixture by measuring the mass changes [27]. This method is based on the premise that under an inert environment, the metal oxides are reduced to elemental metals at high temperatures in the presence of carbon, working as a reducing agent. TGA detects mass loss as a function of increasing temperature, which can be associated with carbon degradation, assigned to the oxidation of the graphite content. A higher mass loss can typically be assigned to a larger fraction of oxides from the cathode material that is available to react with the carbon content. Measuring the mass loss of a sample containing a mixture of anode and cathode material can indicate the fractions of anode/cathode compared to similar experiments done in the literature on the TGA of these materials.

By analysing the mass loss of different samples that underwent TGA measurements and comparing them with the corresponding elemental composition from Inductively Coupled Plasma (ICP) analysis, we can see if there is a correlation between mass loss and graphite content, as proposed in the literature.

4.5.1. Methodology

Two Li-ion battery active materials are used for sediment analysis. Lithium-iron-phosphate ($LiFePO_4$, LFP) and graphite are provided by the Reactor Institute, TU Delft. These are very fine powders that are typically used as active materials in Li-ion batteries, just as the obtained materials from the opened battery. The reason for not using the obtained materials from the opened batteries is that these cannot be used for Thermogravimetric Analysis (TGA) due to safety measures.

Inductively Coupled Plasma - Optical Emission Spectroscopy (ICP-OES) is performed on the original LFP and graphite and on the four sediment samples to investigate the elemental composition of the materials.

Figure G.2 shows the elemental composition of the provided battery materials by ICP analysis. As the name suggests, LFP consists mainly of Iron and Phosphate (37 and 58 wt.% respectively), with a smaller fraction of lithium (5 wt.%). The graphite sample shows almost completely not-measurable components (97 wt.%). This part mainly consists of carbon, which cannot be measured by ICP-OES. Also, a very small fraction of other elements are found by ICP-OES, seen as small traces in the sample with fractions smaller than 0.35 wt.%. Table D.3 in Appendix D provides the total elemental composition.

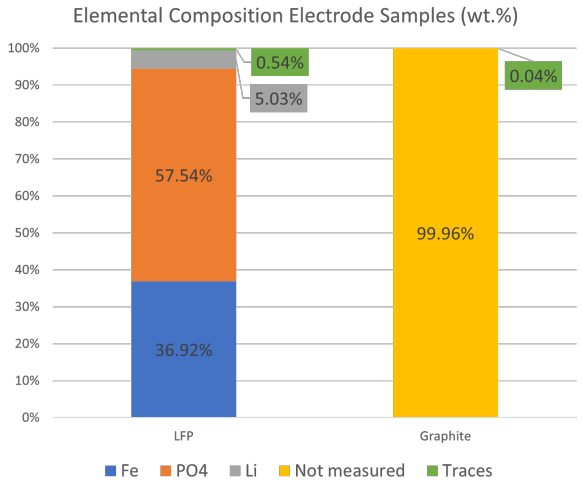

Figure 4.6: ICP-OES results of LFP and graphite, the two materials used for sediment characterisation.

A 50:50 mixture by weight of LFP and graphite is used for the characterisation of the sediment. The steps for freezing the sediment and cutting the layers are conducted as described in Section 4.1. Four layers are obtained from the frozen sediment and dried to be further characterised. Two replicated sedimentation experiments are performed. One of them is characterised by TGA, and they are both characterised by ICP analysis to obtain an average elemental composition per layer.

A TA Instruments SDT 650 machine is used for the TGA experiments, where a 20 ± 5 mg sample is placed in an alumina crucible under a nitrogen atmosphere with a 70 ml/min flow. Figure 4.7 shows the crucible filled with a powder sample placed on a beam in the TGA machine. For the TGA experiments, the heating rate is 10 °C per minute, up to 1000 °C. This maximum temperature is chosen as it is seen that the decomposition of battery materials occurs around this temperature [27]. This is followed by a thermal stabilisation for 60 minutes and, after that, cooling of the sample at a rate of 10 °C, back to room temperature. TGA measurements were performed on the four sediment layers in duplicates.

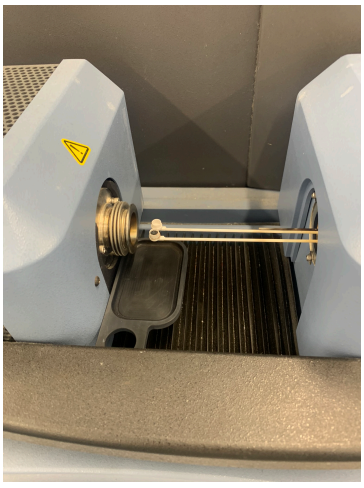

Figure 4.7: Picture of TGA machine. The crucible containing the powder sample is placed on a beam for precise weight calibration. When all settings are set, the TGA is closed, and the experiment is started. A nitrogen flow will flow along the crucibles at a 70 mL/min rate. A furnace will heat the sample with a rate of 10 °C/min.

4.5.2. Results from TGA and ICP-OES measurements

Figure 4.8 shows the TGA and ICP-OES results for the different sediment layers. The TGA plot shows the controlled temperature increase over the time of the experiment (red dotted line) in region I. For each sample layer, the two measurements are plotted as solid lines. It is observed that during the temperature increase in region I, barely any mass change is measured in all the samples. In region II, all samples start to lose weight at around 975 - 1000 °C. A steep decrease in mass change continues until the end of the isothermal. This is in accordance with previous studies [27, 46] From where the samples start to lose weight, we also find an exothermic peak measured from the Differential Scanning Calorimetry (DSC). This could be assigned to a decomposition peak where the metallic components in the samples start to reduce.

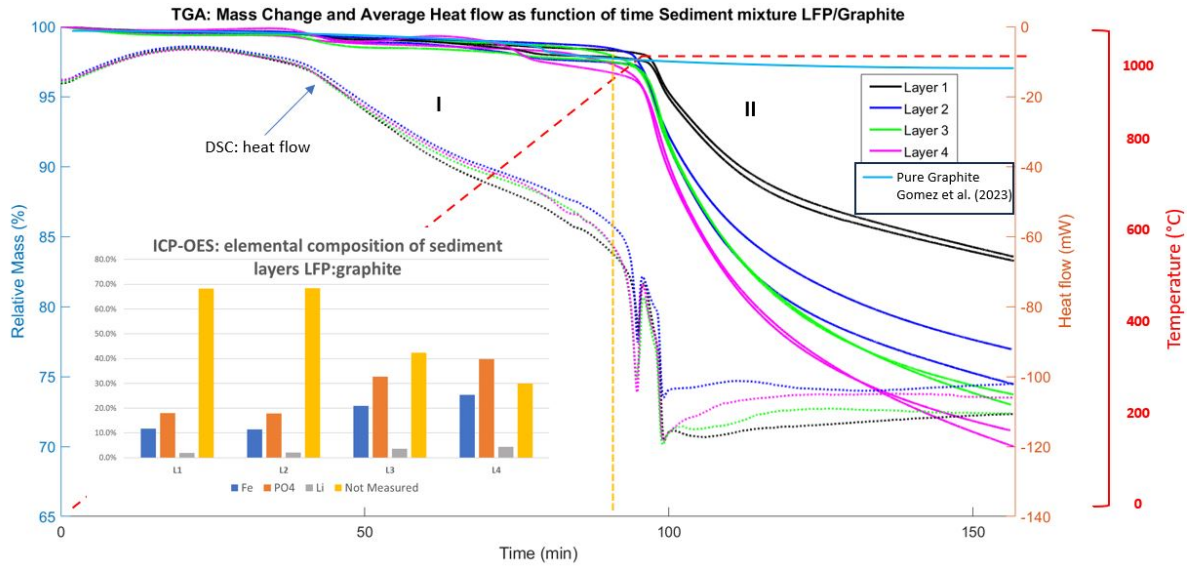

Figure 4.8: TGA plots of four analysed sediment layers. Two TGA measurements are performed for each layer. The plot's solid lines correspond to the layers' mass loss over time for the two measurements. Around 1000 °C, a substantial decrease in mass is visible, together with an exothermic peak in heat flow at that temperature. All samples show a constant and similar mass change curve but end up at a different value for the mass change. The pure graphite mass change is plotted according to Gomez et al. ([27]). The dotted lines correspond to the average measured heat flow of the samples using Differential Scanning Calorimetry (DSC). The ICP-OES results show the corresponding elemental composition of the layers.

The different layers show the same mass loss curve, but they all have different values for the measured mass change at the end of the experiment. Layer 1, which corresponds to the top layer of the sediment, shows the smallest change in mass of around 16 %. Layer 4, the bottom layer of the sediment, exhibits the largest mass loss of 30 %. Layers 2 and 3 are in between, resulting in a mass decrease of 24 and 27 %, respectively. The two measurements per sample show that their mass change curve is constant. Only for layer 2, a difference of 2.5 % between the measurements is seen, while the others show a difference of 1 % at most.

Notable differences are observed when examining the elemental composition of the different sediment layers from ICP-OES in Figure 4.8. Each sample layer is composed of a mixture of LFP and graphite material with an unknown ratio per layer. Layers 1 and 2 have a similar composition, measuring an LFP fraction of 31 wt.%. Layer 4, on the other hand, has a higher LFP fraction, accounting for around 70 wt.% of the measured sample, which is more than twice the amount found in layers 1 and 2. Layer 3 has an LFP fraction closer to the fourth layer of 57 % when adding up the Li, Fe and PO_4 weight fractions.

Comparing these ICP-OES results with the measured mass changes from the TGA, it is observed that samples 3 and 4, which have a relatively high LFP fraction, show a higher decrease in mass. Instead, samples 1 and 2 have a much smaller LFP fraction and show a smaller mass change from the TGA measurements. This might be attributed to the stability of graphite due to its larger content in layer 1 compared to layer 4. The mass change of pure graphite is plotted in the TGA plot. According to Gomez et al. [27], barely any mass loss is seen for the pure graphite, as no metal oxides are available to react with the graphite. In line with what was seen in the literature, a higher content of metal oxides (LFP) in the sample would result in a higher mass loss, as more oxides from the lithium-iron-phosphate are available to react with the carbon from the graphite. Although the deviation in mass change of sample 2 is larger than the others, it is seen closer to layer 3 than layer 1. This is in line with the mass balance from the freezing experiments added in Appendix G: most Li, Fe, and PO_4 are found in the bottom layer, and the smallest LFP fraction is found in the top layer (L1).

4.5.3. Conclusion and Discussion: Utilising TGA for Battery Material Analysis

TGA, in combination with DSC, helps to understand the thermal stability of LFP and graphite contained in the different layers. An exothermic peak was seen, indicating that the decomposition occurred. This was shown by a significant mass loss starting at around 975 °C that continues during the isothermal at 1000 °C and ranges between 16 and 30%. Reduction of iron oxides by carbon in an inert environment occurs typically at temperatures of around 900 - 1000 °C [24]. TGA, in combination with Evolved gas analysis (EGA) and Quadrupole Mass Spectrometry (QMS), should be conducted to see if gaseous components are released during the mass loss of the samples [27, 20]. Measuring CO and CO_2 evolution could indicate carbon decomposition.

The differences in mass loss measured between the samples indicate a distinction in the LFP and graphite composition proportion. It can be concluded that the samples with a higher LFP fraction show a higher mass loss from TGA experiments, while the samples with a smaller metal-oxide fraction show a smaller mass change. However, no strong relation can be found between the LFP elemental fraction and the corresponding mass change by TGA. Therefore, performing a series of TGA experiments with known ratios between the LFP and graphite would be recommended to find a correlation and compare it with the unknown sediment layers.

5

Conclusions and recommendations

5.1. Summary and conclusions

This thesis tests a circular battery manufacturing principle based on the idea that anode and cathode could be designed to have different particle sizes to allow easy separation by centrifugation.

A disassembled end-of-life Li-ion battery provided the anode and cathode materials from the battery cells. Using Scanning Electron Microscopy (SEM), images were made of the dry powder anode and cathode to analyse the size and shape of the individual grains. The cathode particles were found to be perfectly spherical. The anode (graphite) particles were a combination of spherical and elliptical shapes surrounded by thin disk-like flakes that were mainly clustered. It was seen that the size of the anode particles is slightly larger, and its distribution is broader compared to the cathode.

Grinding the materials using a ball miller significantly affects the particle size: images of milled anode and cathode show many clouds of particles of smaller size and various undefined shapes. The size distributions are narrowed considerably, and a remarkable reduction in size is observed by a factor of 6 for the cathode and 8 for the anode.

By evaluating the overlap in the distribution of the settling velocities of the two materials, we showed that milling only one of the electrode materials results in the greatest difference in settling velocity. The overlap indicates the fraction of particles with similar settling velocities and, therefore, cannot be separated. Unmilled anode, in combination with milled cathode, gave the smallest overlap between the velocity distributions and, therefore, the largest difference in settling rates. According to sedimentation calculations on the velocity distributions, only a maximum fraction of 28% of cathode particles would be separated if the anode and cathode were unmilled. In contrast, a combination of unmilled anode with 30 minutes of milled cathode gives a maximum separation efficiency of 91%. Therefore, we can conclude that a simple size reduction of the cathode grains in manufacturing circular batteries can lead to black masses of anode-cathode mixtures easily separable by sedimentation.

A relatively fast and straightforward methodology is proposed to track and quantify the sedimentation of dilute suspensions of anode and cathode materials. The method rests on measuring the light intensity. With this method, we could measure directly the settling velocity of anode and cathode materials. Unmilled anode and cathode materials exhibit relatively similar sedimentation velocities, with the cathode settling 1.5 times faster on average than the anode. Milling significantly reduces the average sedimentation velocity of both anode and cathode, with a more pronounced effect on the cathode, where the settling rate is up to a factor of 250 times smaller than the unmilled variant. In contrast, the milled anode decreases up to 60 times. This result confirms that a relatively small size reduction can lead to anode-cathode mixtures that are separable by sedimentation in liquids. This is shown by the velocity ratios between the two materials in Figure 5.1.

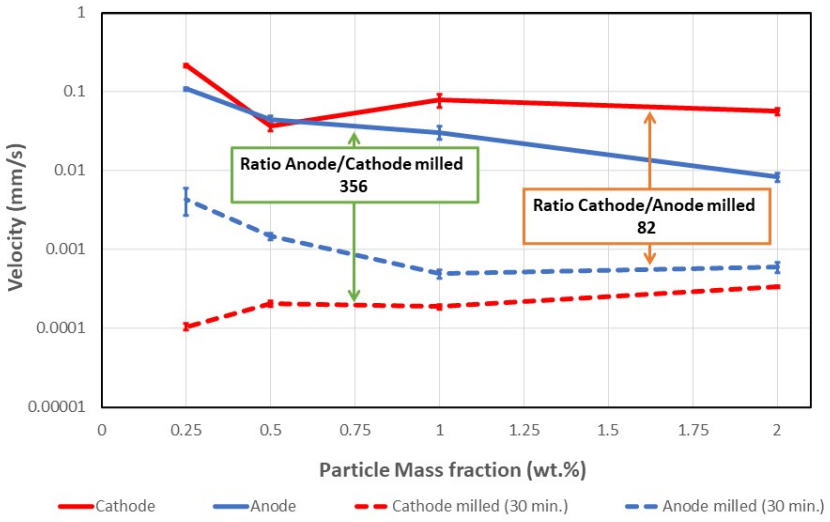

Figure 5.1: Measured sedimentation velocities of anode and cathode. The velocity ratios between the milled and unmilled samples show the impact of milling one of the materials and the potential for separating anode and cathode by milling one of the materials.

Comparing the velocities from the experiments with the corresponding Stokes' velocities, we find, for both anode and cathode, that the theory for hindered settling gives a much weaker dependence on solid fraction than observed in experiments. The anode material shows a significant difference from its predicted values. It can be concluded that using Stokes' law to forecast the sedimentation speed of anode material in a dilute suspension is inaccurate. The measured speed was seen as up to 16 times smaller than what would be expected by Stokes', with a measured speed that would correspond to a volume fraction of 36 %. An explanation for this phenomenon has not been developed and will require further research.

One of the biggest challenges in testing separation methods is proving that the separation is effective. In sedimentation, effective separation leads to stratification in the sediment layer. But how do we prove that such separation indeed took place? We were able to analyse the morphology and composition of sedimented mixed active materials by designing a completely new and consistent method. By freezing the loosely accumulated sediment, we obtained the anode and cathode material while conserving the undisturbed structure of the sediment. By cutting the frozen sediment into horizontal layers, we could efficiently characterise the sediment as a function of the sediment's vertical position.

Inductively Coupled Plasma - Optical Emission Spectroscopy (ICP-OES) measured the metallic content corresponding to the cathode fraction from the mixed anode-cathode materials. Together with SEM analysis, substantial composition and particle morphology differences among the distinct suspension layers are revealed. We can conclude that a degree of separation occurs in the suspension for the anode and cathode materials that exhibited much overlap in velocity distributions. Considering the particle mass fraction and the metal fraction of the sample layers, a gradual increase of cathode material is measured towards the bottom of the sediment. Only a small weight fraction, around 1 wt.%, is present in the top layer of the sediment. This was also seen from the SEM images, where mostly individual graphite particles were found in the top layer. In contrast, the bottom layer of the sediment was filled with mostly large and compacted agglomerates of graphite together with NMC particles, exhibiting a remarkable size of 100 - 500 μm. Thermogravimetric Analysis (TGA) showed the thermal stability of the sample layers. Differences in mass loss that occurred at high temperatures due to thermal decomposition indicate a distinction in anode and cathode fractions in the samples. In line with ICP-OES measurements, a more significant mass loss is attributed to a larger metallic fraction in the sample. Our sediment characterisation methods could be used for other methods for direct recycling, such as froth flotation, separation by density or magnetic susceptibility.

In summary, the main achievements of this project have been:

- Conduct sedimentation experiments with active materials obtained by disassembling a Li-ion battery. These are the first such experiments reported in the literature.
- Altering the particle size distributions of active materials by grinding the powders, thereby showing potential for separation of the materials by changing the velocity distributions.
- Demonstrating the impact of particle concentrations and milling time on sedimentation rates for anode and cathode materials.
- Developing a reliable method for characterising the undisturbed structure of sedimented materials

5.2. Recommendations for further research

- **Find a method to visualise graphite particles easily**
  Ideally, one would like to identify anode and cathode particles separately from a mixed suspension. A recommendation would be to find ways to visualise the graphite particles. As both anode and cathode powders exhibit a black colour, you cannot see the differences between them by eye. In a controlled environment like a sedimentation tank or tube, tagging one of the materials to identify particles through the sedimentation process would give information on how anode and cathode behave differently in settling dynamics in a mixed suspension.
- **Quantify the elemental composition**
  The quantification of anode and cathode material is related to the challenge of visualising graphite particles. Quantitative characterisation of materials from the black mass is necessary for circular batteries. The efficiency of recycling processes such as froth flotation and metallurgy are affected by the amount of graphite [63, 50]. As the black mass of a LIB consists of various forms of carbon (organic, inorganic and elemental), the distinction between them is not trivial. Organic carbon black, used as a conductive additive, is present in both the anode and cathode materials in small quantities (5-10 wt.%), making it complicated to distinguish between anode and cathode material.

  Inductively Coupled Plasma - Optical Emission Spectroscopy (ICP-OES) is a quantitative method used to measure the elemental composition of the frozen sediment layers. The limitation of this technique is the significant fraction of anode and cathode material that ICP-OES cannot measure because of the presence of oxides in cathode material and the carbon content in both anode and cathode materials. This challenges quantifying anode and cathode fractions in a typical black mass sample. It would be recommended to explore different characterisation techniques to find the composition of battery material mixtures. For example, combustion analysis or ultimate analysis can be performed to determine the carbon fraction [73, 26]. A method proposed by Gomez et al. [27] shows the correlation between mass loss and graphite fraction that can be found by performing Thermogravimetric Analysis (TGA) on a series of samples with known anode/cathode ratios. This approach was accurate, fast and straightforward for NMC-graphite and LCO-graphite model black mass mixtures.
- **Examine alternative milling methods**
  From the created particle size distributions, we observed that using the Hertsch Ball miller affects the size distribution and reduces the particle size. However, many original particles are still present after using this ball miller. The ball only shears and compacts a fraction of the particles on the side walls of the jar as it only oscillates sideways. Therefore, there was still an overlap in the particle distributions of the milled and unmilled materials. Besides, there was little information in the literature on this particular milling machine.

  Other grinding machines or techniques could be examined, with more information in literature where similar experiments are conducted on dry powders in the same size range. For example, a planetary ball mill consisting of multiple small balls in a cylinder rotating around their axis, which is installed on a disk rotating at a certain angular velocity, is used a lot for milling dry powders with a size in the range of tens of micrometres and show high milling efficiency as the multiple balls impact the particles during the process [29].

- **Better characterisation of the particle size distribution**
  In this research, the powders' particle size distributions (PSD) were made using SEM images at different local spots of a small sample. Although counting individual grains with ImageJ software from an SEM image gives a good representation of the sizes at that sample spot, it never really reflects the size distribution of the whole powder. As there is a lot of overlap of particles at the crowded spots, identifying individual particles is very difficult. The ground anode and cathode material, containing clouds of small flakes, are challenging to analyse.

  One effective method to measure the size distribution is Laser Diffraction Sensoring, used in literature [71, 64]. It is an efficient and relatively easy method to measure the PSD of multiple dry samples of a few grams to obtain an accurate size distribution of the entire material. It includes a laser light source and multi-element photodetectors to detect light-scattering signals after the powder is fed into the machine. From the measured light signals, the PSD of the samples can be determined very precisely. Complementing SEM analysis with Laser Diffraction would enhance understanding of size distribution for the (milled) anode and cathode materials.
- **Test separation by mass density rather than by settling rate**
  Traditional gravity sedimentation in water poses challenges due to the similar anode and cathode densities that are higher than the density of water, causing both to settle. An alternative approach is to use the density difference between anode and cathode for separation. A heavy liquid is used with an intermediate density between graphite (2200 kg/m^3) and NMC particles (4500 kg/m^3). Heavy liquids like Bromoform ($CHBr_3$), Diiodemethane, Sodium Polytungstate (SPT), and lithium metatungstate (LMT) offer such intermediate densities [77]. Suspending a mixture of anode and cathode in a heavy fluid would cause the graphite particles to float on top of the fluid, while the NMC particles would settle at the bottom. Figure 5.2 shows a suspension where graphite and NMC particles are separated by LMT liquid. Graphite powders floated to the surface of the LMT solution while NMC111 sunk to the bottom, confirming the difference in specific densities between these two materials.

  Another way is the use of magnetic fluids to separate by density. Using a strong magnetic field, paramagnetic liquids become heavier and can thus be used to separate materials of different densities [62]. For example, by suspending magnetic iron oxide particles, the liquid becomes paramagnetic, creating a density gradient. It is shown to separate different plastics effectively and is suitable for industrial application [55].

  The method of separation by density is promising and has been applied by the company Onto Technology, working on the direct recycling of Li-ion batteries [68]. However, some of the earlier mentioned intermediate liquids can be very viscous and toxic, making industrial application of this method and recycling of these liquids challenging [11]. Therefore, it is recommended to test different intermediate liquids and explore the application of magnetic density separation of anode and cathode materials.

Figure 5.2: A mixture of graphite and NMC powders in a lithium metatungstate (LMT) solution after settling in 2 days. Reproduced from Zhan et al. [77].

- **Sedimentation tracking of opaque suspensions**
  The method of tracking the sedimentation of suspended anode and cathode particles proposed in this thesis showed limitations. As was seen from the sedimentation tracking process, low mass-fractioned samples (> 1 wt.%) already showed very opaque suspensions. Differences in measured light intensities were barely measurable: a minimum measurable intensity was reached for the camera. Looking for other methods to measure higher concentrated suspensions would be recommended. Instead of using optical methods, one could use Magnetic Resonance Imaging (MRI) to measure the sedimentation process of anode and cathode suspensions. Balbierer et al. (2019) [7] showed that using signal intensities from the magnetic resonance of silicon oil, the spatial distribution of particles over time could be tracked. This versatile method can be used for any particle that does not provide an MRI signal, as the liquid gives the intensity and can be measured for higher particle concentration. This method can also help to understand the particle dynamics during sedimentation in water. We saw that predicting the anode velocity using Stokes' was inaccurate at high concentrations, and the processing in water affected the particles' morphology. MRI can measure spatial particle volume fractions to look for possible particle agglomeration and entrainment of particles that can help us understand why we find a large difference between measurements and Stokes' predictions.
- **Test separation of anode and cathode material using a centrifuge**
  Centrifugation is the application of sedimentation using the same principle as gravity-based sedimentation. Instead, using a centrifuge, the gravity is replaced by a centrifugal force, for which up to 80000 times the gravity can be reached [32]. This means this factor increases the measured sedimentation velocities of the anode and cathode material. As the sedimentation speeds of the particles in water are in the order of μ/s, using a centrifuge for sedimentation is more practical for large-scale applications of separating the anode and cathode.

  Wolf et al., [71] successfully separated lithium-iron-phosphate particles from carbon black using a high-speed tubular centrifuge. Figure 5.3 shows the outside of the CEPA Z11 tubular centrifuge with its dimensions. The rotating tube is a compact unit that can reach rotational speeds of up to 50000 rpm. Dilute suspensions containing a few grams of solid material can be pumped through the centrifuge at 50 - 250 ml/min. The tube can be opened at the side to obtain the accumulated sediment at the side walls. Thus, the sediment can be easily sampled at different heights for characterisation. Using this sedimentation method for the anode and cathode samples would be recommended to test whether separating the anode and cathode is possible when they have a difference in size. The process can be optimised using the proper centrifuge settings by calculating the margin particle size of the active materials, which determines the particle distribution between the sediment and centrate. The hypothesis of this margin size can then be tested by characterising the sediment's structure to see if separation took place.

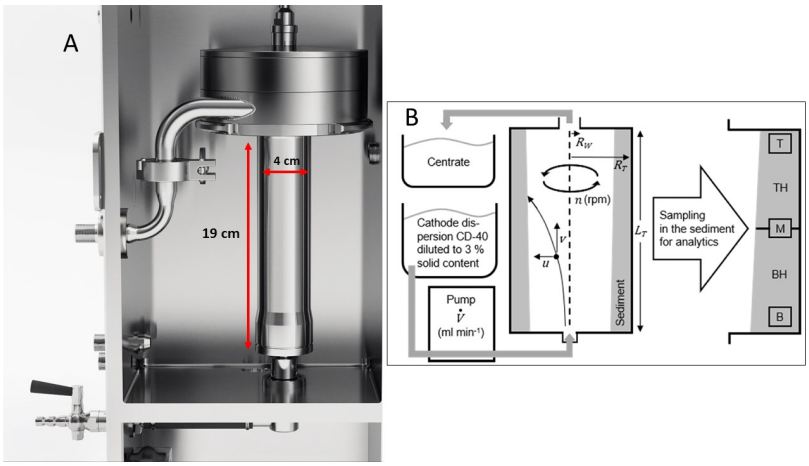

Figure 5.3: A. Outside of the CEPA Z11 tubular centrifuge with the dimensions of the rotor tube [32]. Figure B shows the schematics of a diluted suspension pumped through the rotor. Incoming particles are stratified according to their size and density. After the suspension is fully pumped through, the tube can be opened, and the accumulated sediment can be analysed at different heights. Reproduced from [71]

- **Production of circular batteries**
  It has been demonstrated that particle size has a relatively minor impact on the viscosity of an electrode slurry, provided that the size of the grains remains in the micron range [43]. For microsized particles, rheology is indeed primarily a function of solid fraction and not particle size. Therefore, one can expect that the coating of battery electrode slurries will not be affected significantly by smaller grains of electrode materials. As smaller active material particle size increases its specific surface area, the electrode's transfer kinetics and reversible capacity increase. However, a smaller particle size also causes a larger specific surface area of active material where electrolyte decomposition takes place, and this influences the electrode performance by affecting the cycle stability and cycle capacity negatively [75, 3]. Therefore, an interesting case for the battery industry would be to implement these milled active materials in electrodes and look at the effect on the performance and stability of these new electrodes. In line with the recycling of batteries, this could lead to redesigning battery electrodes so that the anode or cathode includes smaller grains and direct graphite recycling can be made much more accessible. In that way, mechanically crushing an end-of-life battery and sieving until you are left with a small fine powder fraction of active materials will make separation by sedimentation of the anode and cathode the last step to recover the separated anode and cathode material.

  Figure 5.4 shows the plot from the preliminary results in Appendix H with the particle size ratios for which separation should be possible/not possible according to our estimations. As displayed by the grey area, there is a range of size ratios for which separation would not be possible. Outside of this area, the particle ratios can be found for which the velocity difference between the anode and cathode is significant enough to be separated in water. This figure can be a helpful guideline for the design of circular batteries: a smaller grain size of the cathode material, reduced by a factor of 6, shows that the present particle sizes are stratified enough to separate the anode and cathode materials.

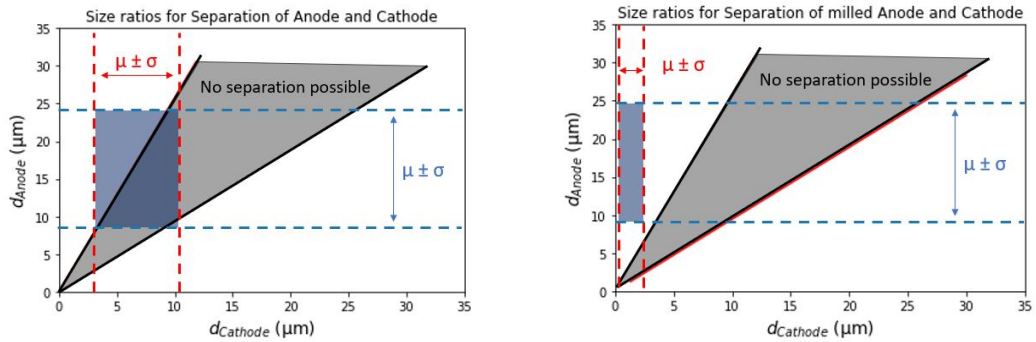

Figure 5.4: Estimation of anode and cathode sizes for which separation is possible and not possible. The outsides of the grey area correspond to sizes for which separation is possible. From the particle size distributions of the powder samples, the cross-sections of the size ranges are shown, including the mean plus minus the standard deviation of the distribution. (a) shows the unmilled anode and cathode ranges corresponding to 80% of all the particles of their distributions. (b) shows the unmilled anode and 30 min. milled cathode ranges that correspond to 92 % of the particles from the distributions.

References

[1] Hayder Ali, Hassan Abbas Khan, and Michael Pecht. *Preprocessing of spent lithium-ion batteries for recycling: Need, methods, and trends*. Oct. 2022. DOI: 10.1016/j.rser.2022.112809.

[2] "Applications of polydisperse sedimentation models_Berres_2005". In: ().

[3] Jakob Asenbauer et al. *The success story of graphite as a lithium-ion anode material-fundamentals, remaining challenges, and recent developments including silicon (oxide) composites*. Nov. 2020. DOI: 10.1039/d0se00175a.

[4] Luqman Azhari et al. "Effects of Extended Aqueous Processing on Structure, Chemistry, and Performance of Polycrystalline LiNi xMn yCo zO2Cathode Powders". In: *ACS Applied Materials and Interfaces* 12.52 (Dec. 2020), pp. 57963–57974. ISSN: 19448252. DOI: 10.1021/acsami.0c20105.

[5] Hyuntae Bae and Youngsik Kim. *Technologies of lithium recycling from waste lithium ion batteries: A review*. May 2021. DOI: 10.1039/d1ma00216c.

[6] Yaocai Bai et al. "Sustainable Direct Recycling of Lithium-Ion Batteries via Solvent Recovery of Electrode Materials". In: *ChemSusChem* 13.21 (Nov. 2020), pp. 5664–5670. ISSN: 1864564X. DOI: 10.1002/cssc.202001479.

[7] R. Balbierer et al. "Sedimentation of lithium–iron–phosphate and carbon black particles in opaque suspensions used for lithium-ion-battery electrodes". In: *Journal of Materials Science* 54.7 (Apr. 2019), pp. 5682–5694. ISSN: 15734803. DOI: 10.1007/s10853-018-03253-2.

[8] David K. Basson, Stefan Berres, and Raimund Bürger. "On models of polydisperse sedimentation with particle-size-specific hindered-settling factors". In: *Applied Mathematical Modelling* 33.4 (Apr. 2009), pp. 1815–1835. ISSN: 0307904X. DOI: 10.1016/j.apm.2008.03.021.

[9] Daniel A. Bertuol et al. "Application of spouted bed elutriation in the recycling of lithium ion batteries". In: *Journal of Power Sources* 275 (Feb. 2015), pp. 627–632. ISSN: 03787753. DOI: 10.1016/j.jpowsour.2014.11.036.

[10] Nicolas Blanc et al. "Evolution of grinding energy and particle size during dry ball-milling of silica sand". In: *Powder Technology* 376 (Oct. 2020), pp. 661–667. ISSN: 1873328X. DOI: 10.1016/j.powtec.2020.08.048.

[11] John Callahan. "A Nontoxic Heavy Liquid and Inexpensive Filters for Separation of Mineral Grains: RESEARCH METHOD PAPER". In: *Journal of Sedimentary Research (SEPM)* 57.4 (1987), pp. 765–766. URL: https://archives.datapages.com/data/sepm/journals/v55-58/data/057/057004/0765.htm.

[12] Aleksander Cholewinski et al. *Polymer binders: Characterization and development toward aqueous electrode fabrication for sustainability*. Feb. 2021. DOI: 10.3390/polym13040631.

[13] R. Clift, J. R. Grace, and M. E. Weber. *Bubbles, Drops, and Particles*. Mineola, New York: Dover, 2005.

[14] Emilia Coldwell, Hannah Rose, and Jasmine Dankworth. *Lithium iron phosphate (LiFePO4) powder for Li-ion battery cathode application*. URL: https://nanografi.com/battery-equipment/lithium-iron-phosphate-lifepo4-powder-for-li-ion-battery-cathode-application/.

[15] Emilia Coldwell, Hannah Rose, and Jasmine Dankworth. *Lithium Nickel Manganese Cobalt Oxide (LiNiCoMnO2) Powder for High Power Li-ion Battery Cathode Application, (Ni:Mn:Co=5:3:2) NMC 532*. URL: https://nanografi.com/battery-equipment/lithium-nickel-manganese-cobalt-oxide-linicomno2-powder-for-high-power-li-ion-battery-cathode-application-ni-mn-co-5-3-2-nmc-532/.

[16] *COMMITTEE AND THE COMMITTEE OF THE REGIONS Critical Raw Materials Resilience: Charting a Path towards greater Security and Sustainability 1*. Tech. rep. URL: http://info.worldbank.org/governance/wgi/..

[17] R. H. Davis and K. H. Birdsell. “Hindered settling of semidilute monodisperse and polydisperse suspensions”. In: *AIChE Journal* 34.1 (1988), pp. 123–129. ISSN: 15475905. DOI: 10.1002/aic.690340114.

[18] Robert H. Davis and Hatice Gecol. “Hindered settling function with no empirical parameters for polydisperse suspensions”. In: *AIChE Journal* 40.3 (1994), pp. 570–575. ISSN: 15475905. DOI: 10.1002/aic.690400317.

[19] Robert H. Davis and Mark A. Hassen. “Spreading of the interface at the top of a slightly polydisperse sedimenting suspension”. In: *Journal of Fluid Mechanics* 196 (Nov. 1988), pp. 107–134. ISSN: 14697645. DOI: 10.1017/S0022112088002630.

[20] Juan C. De Jesus et al. “Thermal decomposition of nickel acetate tetrahydrate: An integrated study by TGA, QMS and XPS techniques”. In: *Journal of Molecular Catalysis A: Chemical*. Vol. 228. 1-2 SPEC. ISS. Mar. 2005, pp. 283–291. DOI: 10.1016/j.molcata.2004.09.065.

[21] Robert Dominko et al. “Influence of carbon black distribution on performance of oxide cathodes for Li ion batteries”. In: *Electrochimica Acta* 48.24 (Oct. 2003), pp. 3709–3716. ISSN: 00134686. DOI: 10.1016/S0013-4686(03)00522-X.

[22] Robert Dominko et al. “The role of carbon black distribution in cathodes for Li ion batteries”. In: *Journal of Power Sources*. Vol. 119-121. June 2003, pp. 770–773. DOI: 10.1016/S0378-7753(03)00250-7.

[23] Steffen Fischer et al. “Impact of Spheroidization of Natural Graphite on Fast-Charging Capability of Anodes for LIB”. In: *Batteries* 9.6 (June 2023). ISSN: 23130105. DOI: 10.3390/batteries9060305.

[24] R J Fruehan. *The Rate of Reduction of Iron Oxides by Carbon*. Tech. rep.

[25] P.G. de Gennes, F. Brochard-Wyart, and D. Quere. *Capillarity and Wetting Phenomena: Drops, Bubbles, Pearls, Waves*. Springer New York, 2003. ISBN: 9780387005928. URL: https://books.google.nl/books?id=MxLQk8vms-kC.

[26] Gary D. Gillespie et al. “Prediction of quality parameters of biomass pellets from proximate and ultimate analysis”. In: *Fuel* 111 (2013), pp. 771–777. ISSN: 00162361. DOI: 10.1016/j.fuel.2013.05.002.

[27] Luis Arturo Gomez-Moreno, Anna Klemettinen, and Rodrigo Serna-Guerrero. “A simple methodology for the quantification of graphite in end-of-life lithium-ion batteries using thermogravimetric analysis”. In: *iScience* 26.10 (Oct. 2023). ISSN: 25890042. DOI: 10.1016/j.isci.2023.107782.

[28] Élisabeth Guazzelli, Jeffrey F. Morris, and Sylvie Pic. *A Physical Introduction to Suspension Dynamics*. Cambridge Texts in Applied Mathematics. Cambridge University Press, 2011. DOI: 10.1017/CBO9780511894671.

[29] Pedro L. Guzzo et al. “Evaluation of particle size reduction and agglomeration in dry grinding of natural quartz in a planetary ball mill”. In: *Powder Technology* 368 (May 2020), pp. 149–159. ISSN: 1873328X. DOI: 10.1016/j.powtec.2020.04.052.

[30] Christian Hanisch et al. “Recycling of lithium-ion batteries: A novel method to separate coating and foil of electrodes”. In: *Journal of Cleaner Production* 108 (Dec. 2015), pp. 301–311. ISSN: 09596526. DOI: 10.1016/j.jclepro.2015.08.026.

[31] W. Blake Hawley et al. “Lithium and transition metal dissolution due to aqueous processing in lithium-ion battery cathode active materials”. In: *Journal of Power Sources* 466 (Aug. 2020). ISSN: 03787753. DOI: 10.1016/j.jpowsour.2020.228315.

[32] *High-speed tubular centrifuge*. URL: https://cepa.de/applications/biotechnology-pharmaceuticals-chemicals/application/tubular-centrifuge-2 (visited on 02/12/2024).

[33] *Hindered settlmg m a mubspecies particle system*. Tech. rep.

[34] Kirsten Hund et al. *CLIMATE-SMART MINING FACILITY Minerals for Climate Action: The Mineral Intensity of the Clean Energy Transition*. Tech. rep. 2020. URL: www.worldbank.org.

[35] P N Kumta et al. *Synthesis of LiCoO powders for lithium-ion batteries from precursors 2 derived by rotary evaporation*. Tech. rep. 1998, pp. 91–98.

[36] Arno Kwade et al. *Current status and challenges for automotive battery production technologies*. Apr. 2018. DOI: 10.1038/s41560-018-0130-3.

[37] S. Lee et al. "Combined effect of sedimentation velocity fluctuation and self-sharpening on interface broadening". In: *Physics of Fluids A* 4.12 (1992), pp. 2601–2606. ISSN: 08998213. DOI: 10.1063/1.858449.

[38] Jianlin Li, Claus Daniel, and David Wood. *Materials processing for lithium-ion batteries*. Mar. 2011. DOI: 10.1016/j.jpowsour.2010.11.001.

[39] Yangtao Liu et al. "iScience Perspective Current and future lithium-ion battery manufacturing". In: (). DOI: 10.1016/j.isci. URL: https://doi.org/10.1016/j.isci..

[40] Arumugam Manthiram, Bohang Song, and Wangda Li. *A perspective on nickel-rich layered oxide cathodes for lithium-ion batteries*. Jan. 2017. DOI: 10.1016/j.ensm.2016.10.007.

[41] Zifei Meng et al. *Morphology controlled performance of ternary layered oxide cathodes*. Dec. 2023. DOI: 10.1038/s43246-023-00418-8.

[42] Elsayed Mousa et al. "Characterization and Thermal Treatment of the Black Mass from Spent Lithium-Ion Batteries". In: *Sustainability (Switzerland)* 15.1 (Jan. 2023). ISSN: 20711050. DOI: 10.3390/su15010015.

[43] Christine Nowak et al. "Designing Graphite-Based Positive Electrodes and Their Properties in Dual-Ion Batteries Using Particle Size-Adjusted Active Materials". In: *Energy Technology* 7.10 (Oct. 2019). ISSN: 21944296. DOI: 10.1002/ente.201900528.

[44] M. Polat, H. Polat, and S. Chander. "Physical and chemical interactions in coal flotation". In: *International Journal of Mineral Processing* 72.1-4 (Sept. 2003), pp. 199–213. ISSN: 03017516. DOI: 10.1016/S0301-7516(03)00099-1.

[45] *Principles of Continuous Flow Centrifugation*. Tech. rep.

[46] *Purge Gas Peak Temperature of Endotherm (°C) Weight Loss (%)*. Tech. rep. URL: www.tainstruments.com.

[47] Yu Qiao et al. *Recycling of graphite anode from spent lithium-ion batteries: Advances and perspectives*. Apr. 2023. DOI: 10.1002/eom2.12321.

[48] C.E. Raleigh and F.F. Aplan. "The Use of Mineral Matter Dispersants and Depressants During the Flotation of Bituminous Coals". In: *Processing and Utilization of High-Sulfur Coals V*. Ed. by B.K. Parekh and J.G. Groppo. Vol. 21. Coal Science and Technology. Elsevier, 1993, pp. 71–90. DOI: https://doi.org/10.1016/B978-0-444-81476-0.50014-4. URL: https://www.sciencedirect.com/science/article/pii/B9780444814760500144.

[49] Ulrich Riebel. "An Estimate of Some Statistical Properties of Extinction signals in dilute and concentrated suspensions of monosized spherical particles". In: *Particle & Particle Systems Characterization* 8.1-4 (1991), pp. 95–99. ISSN: 15214117. DOI: 10.1002/ppsc.19910080117.

[50] Tommi Rinne et al. "Recovering value from end-of-life batteries by integrating froth flotation and pyrometallurgical copper-slag cleaning". In: *Metals* 12.1 (Jan. 2022). ISSN: 20754701. DOI: 10.3390/met12010015.

[51] Sergej Rothermel et al. "Graphite Recycling from Spent Lithium-Ion Batteries". In: *ChemSusChem* 9.24 (Dec. 2016), pp. 3473–3484. ISSN: 1864564X. DOI: 10.1002/cssc.201601062.

[52] Nooshin Saadatkhah et al. *Experimental methods in chemical engineering: Thermogravimetric analysis—TGA*. Jan. 2020. DOI: 10.1002/cjce.23673.

[53] Aliza Marie Salces et al. "Joint recovery of graphite and lithium metal oxides from spent lithium-ion batteries using froth flotation and investigation on process water re-use". In: *Minerals Engineering* 184 (June 2022). ISSN: 08926875. DOI: 10.1016/j.mineng.2022.107670.

[54] T. V.S.L. Satyavani, A. Srinivas Kumar, and P. S.V. Subba Rao. *Methods of synthesis and performance improvement of lithium iron phosphate for high rate Li-ion batteries: A review*. Mar. 2016. DOI: 10.1016/j.jestch.2015.06.002.

[55] Silvia Serranti et al. “An innovative recycling process to obtain pure polyethylene and polypropylene from household waste”. In: *Waste Management* 35 (Jan. 2015), pp. 12–20. ISSN: 18792456. DOI: 10.1016/j.wasman.2014.10.017.

[56] Hosop Shin et al. “Electrochemical Performance of Recycled Cathode Active Materials Using Froth Flotation-based Separation Process”. In: *Journal of The Electrochemical Society* 167.2 (Jan. 2020), p. 020504. ISSN: 19457111. DOI: 10.1149/1945-7111/ab6280.

[57] Ilya A. Shkrob et al. “Chemical Weathering of Layered Ni-Rich Oxide Electrode Materials: Evidence for Cation Exchange”. In: *Journal of The Electrochemical Society* 164.7 (2017), A1489–A1498. ISSN: 0013-4651. DOI: 10.1149/2.0861707jes.

[58] Ponisseril Somasundaran, Kalyan K Das, and Xiang Yu. “Selective flocculation”. In: *Current Opinion in Colloid & Interface Science* 1.4 (Aug. 1996), pp. 530–534. ISSN: 13590294. DOI: 10.1016/s1359-0294(96)80123-3.

[59] Joe C. Stallard et al. *Mechanical properties of cathode materials for lithium-ion batteries*. May 2022. DOI: 10.1016/j.joule.2022.04.001.

[60] N. Traore and S. Kelebek. *Characteristics of Spent Lithium Ion Batteries and Their Recycling Potential Using Flotation Separation: A Review*. 2022. DOI: 10.1080/08827508.2022.2040497.

[61] Battery University. *BU-205: Types of lithium-ion*. Oct. 2022. URL: https://batteryuniversity.com/article/bu-205-types-of-lithium-ion.

[62] Bruno Van Wayenburg. *Variable-density fluid accurately separates plastics in a single process*. Tech. rep.

[63] Anna Vanderbruggen et al. “A contribution to understanding the flotation behavior of lithium metal oxides and spheroidized graphite for lithium-ion battery recycling”. In: *Colloids and Surfaces A: Physicochemical and Engineering Aspects* 626 (Oct. 2021). ISSN: 18734359. DOI: 10.1016/j.colsurfa.2021.127111.

[64] Anna Vanderbruggen et al. “Automated mineralogy as a novel approach for the compositional and textural characterization of spent lithium-ion batteries”. In: *Minerals Engineering* 169 (Aug. 2021). ISSN: 08926875. DOI: 10.1016/j.mineng.2021.106924.

[65] Anna Vanderbruggen et al. “Improving Separation Efficiency in End-of-Life Lithium-Ion Batteries Flotation Using Attrition Pre-Treatment”. In: *Minerals* 12.1 (Jan. 2022). ISSN: 2075163X. DOI: 10.3390/min12010072.

[66] Anna Vanderbruggen et al. “Lithium-Ion Battery Recycling—Influence of Recycling Processes on Component Liberation and Flotation Separation Efficiency”. In: *ACS ES and T Engineering* 2.11 (Nov. 2022), pp. 2130–2141. ISSN: 26900645. DOI: 10.1021/acsestengg.2c00177.

[67] “VANDERBRUGGENPhDthesis”. In: ().

[68] Omar Velázquez-Martínez et al. *A critical review of lithium-ion battery recycling processes from a circular economy perspective*. Dec. 2019. DOI: 10.3390/batteries5040068.

[69] Valentin Wenzel, Hermann Nirschl, and Dorit Nötzel. “Challenges in Lithium-Ion-Battery Slurry Preparation and Potential of Modifying Electrode Structures by Different Mixing Processes”. In: *Energy Technology* 3.7 (July 2015), pp. 692–698. ISSN: 21944296. DOI: 10.1002/ente.201402218.

[70] Denis Werner, Urs Alexander Peuker, and Thomas Mütze. “Recycling chain for spent lithium□ion batteries”. In: *Metals* 10.3 (Mar. 2020). ISSN: 20754701. DOI: 10.3390/met10030316.

[71] Andreas Wolf et al. “Centrifugation based separation of lithium iron phosphate (LFP) and carbon black for lithium-ion battery recycling”. In: *Chemical Engineering and Processing - Process Intensification* 160 (Mar. 2021). ISSN: 02552701. DOI: 10.1016/j.cep.2021.108310.

[72] Qiu Yangshuai et al. “Dispersion and agglomeration mechanism of flaky graphite particles in aqueous solution”. In: *Journal of Dispersion Science and Technology* 38.6 (June 2017), pp. 796–800. ISSN: 15322351. DOI: 10.1080/01932691.2016.1198703.

[73] J. C. Yeomans and J. M. Bremner. “Carbon and nitrogen analysis of soils by automated combustion techniques”. In: *Communications in Soil Science and Plant Analysis* 22.9-10 (June 1991), pp. 843–850. ISSN: 15322416. DOI: 10.1080/00103629109368458.

[74] Jierong Ying, Changyin Jiang, and Chunrong Wan. “Preparation and characterization of high-density spherical LiCoO 2 cathode material for lithium ion batteries”. In: *Journal of Power Sources* 129.2 (Apr. 2004), pp. 264–269. ISSN: 03787753. DOI: 10.1016/j.jpowsour.2003.10.007.

[75] K Zaghib et al. *Effect of particle size on lithium intercalation rates in natural graphite*. Tech. rep.

[76] Ruiting Zhan, Zachary Oldenburg, and Lei Pan. “Recovery of active cathode materials from lithium-ion batteries using froth flotation”. In: *Sustainable Materials and Technologies* 17 (Sept. 2018). ISSN: 22149937. DOI: 10.1016/j.susmat.2018.e00062.

[77] Ruiting Zhan and Lei Pan. “A cycling-insensitive recycling method for producing lithium transition metal oxide from Li-ion batteries using centrifugal gravity separation”. In: *Sustainable Materials and Technologies* 32 (July 2022). ISSN: 22149937. DOI: 10.1016/j.susmat.2022.e00399.

[78] Hao Zhang et al. *Graphite as anode materials: Fundamental mechanism, recent progress and advances*. Apr. 2021. DOI: 10.1016/j.ensm.2020.12.027.

A

Typical grains from LIB materials

Grain type	Function	Average particle size [μm]	Particle size deviation [μm]	Average particle density [kg/m^3]	Particle density deviation [kg/m^3]	Re in air	Re in water	Average Stokes velocity in air [m/s]	Average Stokes velocity in water [m/s]	References
LFP	Cathode active material	1.5	0.50 - 6.0	3.3	3.0 - 3.6	$2.3 \cdot 10^{-5}$	$4.2 \cdot 10^{-6}$	$2.1 \cdot 10^{-4}$	$2.8 \cdot 10^{-6}$	[71, 14, 54]
LCO	Cathode active material	10	5.5 - 45	4.8	4.5 - 5.1	$9.9 \cdot 10^{-3}$	$2.1 \cdot 10^{-3}$	$1.4 \cdot 10^{-2}$	$2.4 \cdot 10^{-4}$	[35, 74]
NMC	Cathode active material	10	6.0 - 20	4.5	4.0 - 5.0	$9.3 \cdot 10^{-3}$	$1.9 \cdot 10^{-3}$	$1.3 \cdot 10^{-2}$	$1.9 \cdot 10^{-4}$	[63, 59, 15]
Graphite	Anode active material	18	8.0 - 30	2.25	2.2 - 2.3	$2.7 \cdot 10^{-2}$	$4.0 \cdot 10^{-3}$	$2.1 \cdot 10^{-2}$	$2.2 \cdot 10^{-4}$	[78, 63, 51]
Carbon black	Conductive Additive	0.05	0.01 - 0.1	1.7	1.5 - 1.9	$4.4 \cdot 10^{-10}$	$4.8 \cdot 10^{-11}$	$1.3 \cdot 10^{-7}$	$9.5 \cdot 10^{-10}$	[71, 22, 21]

Table A.1: Typical components in Li-ion batteries with their typical grain size and density. The calculated Reynolds numbers show that Stokes' is applicable as an estimation of the velocity in air and water.

B

Derivations

B.1. Stokes' law

During sedimentation, particles undergo interaction with the fluid. Particles experience a drag force from the fluid while settling under the influence of gravity force. For small, spherical particles in a viscous fluid, the drag force, F_d, due to the interaction of the particle with the fluid can be approximated by:

$$F_d = 3\pi\mu dv \tag{B.1}$$

In this equation, μ is the dynamic viscosity of the fluid, d is the diameter of the spherical particle and v is the flow velocity relative to the particle, or the particle velocity when the fluid is at rest. At settling speed, the particle experiences a gravity force that is compensated by the buoyancy force of the fluid. The excess force F_g can be written as:

$$F_g = (\rho_p - \rho_f)g\frac{\pi d^3}{6} \tag{B.2}$$

Here, ρ_p and ρ_f are the densities of the particle and fluid respectively. g is the gravitational acceleration and $\frac{\pi d^3}{6}$ is the mathematical expression for the volume of a sphere.

Reaching the terminal velocity, the drag force and buoyancy force are balanced by the gravitational force, so equations B.1 and B.2 are set equal to each other. By doing so, the terminal velocity of a single particle is given by:

$$v_s = \frac{g}{18\mu_f}(\rho_p - \rho_f)d_p^2 \tag{B.3}$$

B.2. Mass fraction to volume fraction

Having particles suspended in a fluid with known masses and densities, we can write the particle's mass fraction as:

$$\phi_{\mathsf{m}} = \frac{m_{\mathsf{p}}}{m_{\mathsf{p}} + m_f}$$

For the volume fraction, we can write:

$$\phi_v = \frac{V_p}{V_p + V_f}$$
$$\phi_v = \frac{m_p/\rho_p}{m_p/\rho_p + m_f/\rho_f}$$

The total density of fluid and particles is the density of the whole suspension. Then we can write for the volume fraction:

$$\phi_v = \frac{m_p/\rho_p}{(m_p + m_f)/\rho_{\mathsf{susp}}}$$
$$= \phi_m \left[\frac{\rho_{\mathsf{susp}}}{\rho_p}\right]$$

Using the expression for the density of a suspension:

$$\rho_{\mathsf{susp}} = \phi_v \rho_p + (1 - \phi_p)\rho_f$$

Then we end up with an expression for the volume fraction as a function of mass fraction and densities of particles and fluid:

$$\phi_v = \frac{\phi_m \rho_f}{\rho_p + \phi_m(\rho_f - \rho_p)}$$

B.3. Mass and volume fractions of anode and cathode

Table B.1: Anode, ρ = 2000 kg/m^3)

Mass frac. (%)	Volume frac. (%)
0,25%	0,125%
0,50%	0,251%
1,00%	0,503%
2,00%	1,010%

Table B.2: Cathode, ρ = 4500 kg/m^3

Mass frac. (%)	Volume frac. (%)
0,25%	0,056%
0,50%	0,112%
1,00%	0,224%
2,00%	0,451%

C

Li-ion Battery Dismantling Steps

In this chapter, the steps are described to obtain the liberated anode and cathode material (without binder material) from a Li-ion battery (Xiaomi MI PLM06ZM Powerbank) with a prismatic shape, containing two pouch cells.

Opening a Li-ion battery involves very strict safety measures that need to be taken into account. The electrolyte contains solvents that are released when exposed to the atmosphere, like gaseous and harmful HF. Also, the coated active materials on the electrode are light-weighted, and tiny pieces (in the form of powder) may not be inhaled. Therefore, during all these steps, a half-type respirator must be warned while dismantling and further steps in a closed fume hood.

1. Remove the outer hard plastic casing by cutting it open and cutting the wires that connect the pouch cells with the BMS. Do this carefully, as the electrode strips at the ends of the cells may not touch each other, as contact can cause short-circuiting of the electrodes.
2. Discharge completely the pouch cells by immersing the pouch cells in a salt solution containing 10 wt.% Potassium Carbonate (K_2CO_3). The cells can be safely opened when a potential smaller than 2 Volts is measured between the electrodes of the cells.
3. Cut open the plastic casing of the pouch cell with a small knife. Make sure not to cut through the compacted electrodes inside of the cells.
4. When the casing is removed, the rolled-up electrode sheets and separator sheets can be rolled out and separated from each other. Make sure there is no contact between the two electrode sheets to prevent short-circuiting.

Now, the sheets of current collector foil coated with black active material are collected for further treatment to remove the binder and thereby let the active material detach from the current collector foils. This is done separately for the anode and cathode sheets.

5. The rolled out electrode sheet is cut in small pieces of 5x5 cm and collected in a sieve. This sieve is placed on top of a fitting beaker and filled with liquid NMP, until the electrode pieces are fully immersed in the liquid.
6. This beaker with a sieve is placed in an ultrasone bath inside the fume hood where it is heated at 70 °C for two hours. Stir the foils inside the sieve every 30 minutes to make sure all sheets are exposed well to dissolve the binder material. After a while, it can be seen that the foils loose their black color and get their material color: silver (aluminum cathode sheet) and brown/reddish (copper anode sheet).
7. After two hours, remove the beaker from the bath and pour a small amount of NMP through the sieve.
8. Remove the foils from the sieve and collect them in a petri dish. Put it in an oven at 60 °C for 12 hours to evaporate traces of NMP.

9. The beaker contains a liquid ’black mass’ that is put aside to let the active material precipitate.
10. After 24 hours when all the active material is precipitated, pour over the liquid (containing NMP with dissolved binder) in another beaker and dispose the NMP in the organic halogenated waste.
11. Put the beaker with precipitated black mass and some of the liquid on a hot plate at 120 °C to evaporate the last portion of NMP.
12. After all liquid is dried out, scrape out the powder of anode or cathode black mass and collect it in a little pot.

D

ICP-OES results

D.1. Anode and Cathode materials from opened battery

	Al	B	Ca	Co	Cr	Cu	Fe	K	Li	Mg	Mn	Na	Ni	PO4	SO4	S	Ti	Not Measured
Anode	0,01%	0,00%	0,01%	0,09%	0,00%	0,19%	0,00%	0,01%	1,40%	0,00%	0,00%	0,06%	0,00%	0,53%	0,49%	0,16%	0,00%	97,04%
Cathode	0,69%	0,03%	0,01%	3,85%	0,00%	0,01%	0,80%	0,01%	4,16%	0,17%	22,78%	0,16%	27,50%	0,25%	0,65%	0,22%	0,00%	38,70%

Table D.1: ICP-OES results of anode and cathode samples used for experiments

#1	Al	B	Ca	Co	Cr	Cu	Fe	K	Li	Mg	Mn	Na	Ni	PO4	SO4	S	Ti	Not Measured
Layer 1	0,10%	0,01%	0,01%	0,96%	0,00%	0,07%	0,40%	0,00%	2,16%	0,09%	4,47%	0,05%	4,98%	0,18%	0,31%	0,10%	0,002%	72,30%
Layer 2	0,28%	0,01%	0,01%	1,63%	0,00%	0,07%	0,47%	0,00%	2,17%	0,10%	12,64%	0,04%	11,41%	0,19%	0,31%	0,10%	0,002%	70,56%
Layer 3	0,07%	0,01%	0,01%	1,85%	0,00%	0,08%	0,34%	0,00%	2,15%	0,09%	9,68%	0,05%	12,75%	0,18%	0,32%	0,11%	0,001%	72,30%
Layer 4	0,72%	0,01%	0,01%	2,78%	0,00%	0,12%	0,47%	0,01%	2,96%	0,11%	12,66%	0,06%	19,27%	0,29%	0,32%	0,11%	0,001%	60,10%

#2	Al	B	Ca	Co	Cr	Cu	Fe	K	Li	Mg	Mn	Na	Ni	PO4	SO4	S	Ti	Not Measured
Layer 1	0,20%	0,01%	0,01%	1,23%	0,01%	0,08%	0,43%	0,00%	1,45%	0,05%	4,53%	0,04%	6,88%	0,21%	0,28%	0,09%	0,002%	84,50%
Layer 2	0,22%	0,01%	0,01%	1,48%	0,01%	0,11%	0,50%	0,00%	1,74%	0,07%	8,20%	0,04%	9,76%	0,21%	0,29%	0,10%	0,002%	77,26%
Layer 3	0,29%	0,01%	0,01%	1,97%	0,01%	0,09%	0,94%	0,00%	2,06%	0,09%	11,09%	0,03%	13,55%	0,22%	0,29%	0,10%	0,002%	69,25%
Layer 4	0,43%	0,01%	0,01%	2,71%	0,01%	0,11%	0,68%	0,00%	2,80%	0,12%	15,36%	0,04%	18,48%	0,24%	0,31%	0,10%	0,002%	58,58%

Table D.2: ICP-OES results of two freezing experiments, resulting in 4 sediment layers, from layer 1 (supernatant) up to layer 4 (bottom sediment).

D.2. LFP and graphite

Here the ICP-OES results are shown of the LFP and graphite samples, delivered by the Reactor Institute, TU Delft.

	Al	B	Ca	Co	Cr	Cu	Fe	Li	Mg	Mn	Ni	Zn	PO4	SO4	Ti	V	Not Measured
Graphite	0.001%		0.008%				0.014%	0.002%				0.000%	0.004%	0.006%			99.965%
LFP	0.02%	0.01%	0.00%	0.00%	0.00%	0.00%	39.71%	5.41%	0.00%	0.04%	0.00%	0.00%	61.90%	0.12%	0.00%	0.35%	0.00%

Table D.3: ICP-OES results of LFP and graphite samples

#1	Al	Ca	Fe	Li	Mn	PO4	SO4	Ti	V	Not Measured
1	0.02%	0.01%	16.59%	2.30%	0.02%	25.46%	0.06%	0.00%	0.15%	55.39%
2	0.01%	0.01%	10.31%	1.48%	0.01%	16.36%	0.05%	0.00%	0.11%	71.65%
3	0.02%	0.00%	23.94%	3.31%	0.03%	37.39%	0.07%	0.00%	0.22%	35.01%
4	0.02%	0.00%	26.99%	3.72%	0.03%	42.27%	0.10%	0.00%	0.25%	26.59%

#2	Al	Ca	Fe	Li	Mn	PO4	SO4	Ti	V	Not measured
1	0.00%	0.01%	6.78%	1.52%	0.01%	10.61%	0.03%	0.00%	0.06%	80.99%
2	0.00%	0.01%	12.48%	2.71%	0.01%	19.42%	0.05%	0.00%	0.12%	65.20%
3	0.00%	0.00%	17.98%	3.92%	0.02%	28.01%	0.07%	0.00%	0.17%	49.83%
4	0.00%	0.00%	23.73%	5.15%	0.03%	37.42%	0.08%	0.00%	0.22%	33.36%

Table D.4: ICP results of two freezing experiments Lithium-iron-phosphate (LFP) and Graphite, resulting in 4 sediment layers, from layer 1 (supernatant) up to layer 4 (bottom sediment).

E

Particle size distributions

Table E.1: Particle size distributions Anode

Non-milled		**Milled 5 minutes**		**Milled 10 minutes**		**Milled 30 minutes**	
Size (μm)	Frequency	Size (μm)	Frequency	Size (μm)	Frequency	Size (μm)	Frequency
2-3	1	0-0.25	19	0.25-0.5	56	0-0.25	15
4-5	3	0.25-0.5	43	0.5-0.75	35	0.25-0.5	63
5-6	2	0.5-0.75	34	0.75-1	12	0.5-0.75	14
6-7	1	0.75-1	15	1-1.25	7	0.75-1	9
7-8	1	1-1.25	6	1.25-1.5	6	1-1.25	4
8-9	7	1.25-1.5	5	1.5-1.75	1	1.25-1.5	4
9-10	6	1.5-1.75	4	1.75-2	1	1.5-1.75	4
10-11	5	1.75-2	3	2-2.25	1	1.75-2	3
11-12	5	2-2.25	1	2.5-2.75	1	2-2.25	3
12-13	8	2.25-2.5	1	2.75-3	1	2.25-2.5	3
13-14	11	2.5-2.75	1	3-3.25	2	2.5-2.75	2
14-15	10	2.75-3	1	3.5-3.75	1	2.75-3	2
15-16	4	3-3.25	1	4.25-4.5	1	3-3.25	1
16-17	6	3.25-3.5	1	4.5-4.75	1	3.25-3.5	1
17-18	6	3.75-4	1	4.75-5	1	3.75-4	1
18-19	2	4.25-4.5	1	5-5.25	1	4-4.25	1
19-20	3	4.5-4.75	1	5.75-6	2	4.5-4.75	2
20-21	2	5-5.25	1	6-6.25	1	4.75-5	1
21-22	3	5.5-5.75	1	6.25-6.5	1	5-5.25	1
22-23	4	6.25-6.5	1	6.5-6.75	1	5.25-5.5	1
23-24	2	7-7.25	1	7-7.25	1	5.5-5.75	2
24-25	4	7.25-7.5	1	7.75-8	1	6.25-6.5	1
25-26	2	7.75-8	1	8.25-8.5	1	6.75-7	1
26-27	3	8.5-8.75	1	8.75-9	1	8-8.25	1
27-28	1	8.75-9	1	9.75-10	1	9.25-9.5	1
28-29	1	9-9.25	1	10.75-11	1	10-10.25	1
33-34	1	9.75-10	1	12.75-13	1	12-12.25	1
34-35	1	10.75-11	1	13.75-14	1	12.5-12.75	1
35-36	1	11.25-11.5	1	15-15.25	3	16.5-16.75	1
37-38	1	12-12.25	1				
		13-13.25	1				
		15.5-15.75	1				

Table E.2: Cathode particle size distributions

Non-milled		Milled 5 minutes		Milled 10 minutes		Milled 30 minutes	
Size (μm)	Frequency	Size (μm)	Frequency	Size (μm)	Frequency	Size (μm)	Frequency
1-2	4	0.25-0.5	14	0-0.25	38	0-0.25	60
2-3	10	0.5-0.75	21	0.25-0.5	41	0.25-0.5	24
3-4	16	0.75-1	14	0.5-0.75	32	0.5-0.75	21
4-5	17	1-1.25	11	0.75-1	8	0.75-1	17
5-6	9	1.25-1.5	8	1-1.25	8	1-1.25	3
6-7	14	1.5-1.75	7	1.25-1.5	4	1.25-1.5	2
7-8	16	1.75-2	5	1.5-1.75	3	1.5-1.75	2
8-9	15	2-2.25	5	1.75-2	1	1.75-2	1
9-10	7	2.25-2.5	3	2-2.25	2	2-2.25	1
10-11	4	2.5-2.75	3	2.5-2.75	2	2.25-2.5	1
11-12	9	2.75-3	4	2.75-3	2	2.5-2.75	1
13-14	3	3-3.25	5	3-3.25	1	3-3.25	1
14-15	3	3.25-3.5	5	3.75-4	1	3.25-3.5	1
21-22	4	3.5-3.75	7	4.25-4.5	1	3.75-4	1
		3.75-4	1	4.5-4.75	1	4.25-4.5	1
		4-4.25	1	5.25-5.5	1	5.75-6	1
		4.5-4.75	1	5.75-6	1	7.25-7.5	1
		4.75-5	1	7.75-8	1		
		5-5.25	1	11.25-11.5	1		
		5.25-5.5	1				
		5.5-5.75	1				
		6.25-6.5	1				
		7-7.25	1				
		8.25-8.5	1				
		8.75-9	1				
		11.25-11.5	1				
		14.5-14.75	1				

E.1. Statistics PSD's and (reduced) median particle sizes

The median particle sizes, based on the volume fraction of the samples, are listed for all the samples together with the corresponding Stokes' velocity. The reduced median size is also listed for the milled samples that are used to predict the sedimentation velocities. The particle fractions are the number of particles included in the mean ± the standard deviation of the distributions.

Table E.3: Size distribution statistics with median and reduced median size and their corresponding Stokes' velocity

Material	Mean size (μm)	$\mu \pm \sigma$	Particle fraction $\mu \pm \sigma$	Median size (μm)	Stokes' velocity (mm/s)	Reduced Median size (μm)	(Reduced) Stokes´ velocity (mm/s)
Anode no mill	16.2	8.27 - 24.15	78%	17.625	0.169299141		0.1688192
Anode mill 5min	1.69	0 - 4.60	93%	11.375	0.070517891	3.125	0.005322266
Anode mill 10 min	1.70	0 - 4.50	93%	12.5	0.08515625	2.875	0.004504766
Anode mill 30 min	1.51	0 - 4.06	90%	10.125	0.055871016	2.625	0.003755391
Cathode no mill	6.62	3.17 - 10.08	75%	8.675	0.143550105		0.146042969
Cathode mill 5 min	1.66	0 - 3.40	91%	11.375	0.246812617	2.625	0.013143867
Cathode mill 10 min	0.96	0 - 2.15	91%	11.375	0.246812617	0.875	0.00146043
Cathode mill 30 min	0.85	0 - 1.44	93%	10.625	0.215338867	0.425	0.000391667

F

Size distributions for average velocity

This appendix contains all the used size distributions for calculating the average and median velocities as a function of the concentrations. The (reduced) size distributions are shown together with the average values per size class. From there, the Stokes' velocity and the volume fractions per size class are calculated. The velocity(0) is calculated by multiplying the Stokes' velocity with the volume fraction of that size class. The sum (stated below the table) corresponds to the average velocity of the zero concentration. The hindered settling functions are provided for the concentrations. By multiplying the provided velocities with the hindered settling, the average velocity of that concentration can be calculated by summing the values. They are displayed below the columns.

F.1. Anode

Table F.1: Anode Unmilled

						Volume fraction							
						0.125%		0.25%		0.5%		1.0%	
Size ranges (μm)	Average size (μm)	Frequency	Stokes' velocity (mm/s)	ϕ_1	Velocity_0 (mm/s)	Hindered settling	Velocity component	Hindered settling	Velocity component	Hindered settling	Velocity component	Hindered settling	Velocity component
2-3	2.5	1	0.001703125	2.25567E-05	3.84168E-08	0.749149903	2.878E-08	0.500775564	1.92382E-08	0.0113987	4.37902E-10	-0.93825341	-3.60447E-08
4-5	4.5	3	0.005518125	0.000394652	2.17774E-06	0.919126817	2.00162E-06	0.839030686	1.82719E-06	0.6811523	1.48337E-06	0.374531374	8.15631E-07
5-6	5.5	2	0.008243125	0.000480367	3.95972E-06	0.944211957	3.73882E-06	0.888950274	3.52E-06	0.7799944	3.08856E-06	0.56827175	2.2502E-06
6-7	6.5	1	0.011513125	0.000396456	4.56445E-06	0.958639624	4.37566E-06	0.917661421	4.18862E-06	0.8368432	3.81973E-06	0.679701125	3.10246E-06
7-8	7.5	1	0.015328125	0.00060903	9.33529E-06	0.967691649	9.03368E-06	0.935675007	8.7348E-06	0.8725105	8.14514E-06	0.749612741	6.99785E-06
8-9	8.5	7	0.019688125	0.006205973	0.000122184	0.973741247	0.000118976	0.947713746	0.000115795	0.8963475	0.000109519	0.79633568	9.72995E-05
9-10	9.5	6	0.024593125	0.007426379	0.000182638	0.977983089	0.000178617	0.956155036	0.00017463	0.9130615	0.00016676	0.829096743	0.000151424
10-11	10.5	5	0.030043125	0.008355895	0.000251037	0.981071756	0.000246285	0.962301504	0.000241573	0.9252317	0.000232268	0.852951485	0.000214123
11-12	11.5	5	0.036038125	0.010977882	0.000395622	0.9833903	0.000389051	0.966915421	0.000382533	0.9343673	0.000369657	0.870858325	0.000344531
12-13	12.5	8	0.042578125	0.022556675	0.000960421	0.985174989	0.000946183	0.970466963	0.000932057	0.9413995	0.00090414	0.884642033	0.000849629
13-14	13.5	11	0.049663125	0.039070506	0.001940363	0.986577973	0.00191432	0.97325891	0.001888476	0.9469276	0.001837384	0.895477717	0.001737552
14-15	14.5	10	0.057293125	0.044010779	0.002521515	0.987700822	0.002490502	0.975493387	0.002459721	0.9513519	0.002398848	0.904149832	0.002279827
15-16	15.5	4	0.065468125	0.021503549	0.001407797	0.988613439	0.001391767	0.977309501	0.001375853	0.9549479	0.001344373	0.911198262	0.001282782
16-17	16.5	6	0.074188125	0.038909722	0.002886639	0.989365211	0.002855941	0.97880553	0.002825459	0.95791	0.002765141	0.917004426	0.002647061
17-18	17.5	6	0.083453125	0.046421636	0.003874031	0.989991827	0.003835259	0.980052501	0.003796753	0.9603791	0.003720538	0.921843981	0.003571252
18-19	18.5	2	0.093263125	0.018281012	0.001704944	0.990519603	0.001688781	0.98110278	0.001672726	0.9624587	0.001640938	0.925920162	0.001578642
19-20	19.5	3	0.103618125	0.032112945	0.003327483	0.990968285	0.00329743	0.981995658	0.003267574	0.9642266	0.003208448	0.929385467	0.003092514
20-21	20.5	2	0.114518125	0.024874057	0.00284853	0.991352921	0.002823899	0.982761086	0.002799425	0.9657421	0.002750946	0.932356132	0.002655845
21-22	21.5	3	0.125963125	0.043041925	0.005421695	0.991685145	0.005376615	0.983422215	0.005331816	0.9670512	0.005243057	0.934922005	0.005068862
22-23	22.5	4	0.137953125	0.065775263	0.009073903	0.991974065	0.009001077	0.983997167	0.008928695	0.9681896	0.008785259	0.937153425	0.008503639
23-24	23.5	2	0.150488125	0.037470426	0.005638854	0.992226892	0.005595023	0.984500295	0.005551454	0.9691858	0.005465097	0.939106089	0.005295482
24-25	24.5	4	0.163568125	0.084920647	0.013890311	0.992449398	0.013785431	0.984943082	0.013681166	0.9700625	0.01347447	0.940824567	0.013068346
25-26	25.5	2	0.177193125	0.047874647	0.008483058	0.992646243	0.008420676	0.985334805	0.008358653	0.9708382	0.008235677	0.942344862	0.007993966
26-27	26.5	3	0.191363125	0.080596081	0.015423118	0.992821227	0.015312399	0.985683024	0.015202305	0.9715277	0.014983986	0.943696318	0.01455474
27-28	27.5	1	0.206078125	0.030022934	0.00618707	0.992977471	0.006143621	0.985993951	0.006100414	0.9721433	0.006014719	0.94490304	0.005846181
28-29	28.5	1	0.221338125	0.033418706	0.007396834	0.993117558	0.007345925	0.986272726	0.007295295	0.9726953	0.007194865	0.94598498	0.006997294
33-34	33.5	1	0.305813125	0.054273705	0.016597611	0.993640134	0.016492053	0.987312655	0.016387032	0.9747544	0.016178594	0.950020997	0.015768079
34-35	34.5	1	0.324343125	0.059280565	0.019227244	0.99371836	0.019106465	0.987468325	0.018986294	0.9750626	0.018747766	0.950625156	0.018277901
35-36	35.5	1	0.343418125	0.064586256	0.022180091	0.993790068	0.022042354	0.987611025	0.021905302	0.9753451	0.021633244	0.951178983	0.021097236
37-38	37.5	1	0.383203125	0.076128777	0.029172785	0.993916658	0.028995317	0.98786294	0.028818713	0.9758439	0.028468086	0.952156679	0.027777062
							<v> = 0.181135855		<v> = 0.179813143		<v> = 0.178498004		<v> = 0.175890314

F.2. Cathode

Table F.2: Anode Milled 5 min.

						Volume fraction							
						0.125%		0.25%		0.5%		1.0%	
Size ranges (μm)	Average size (μm)	Frequency	Stokes' velocity (mm/s)	ϕ_i	Velocity_0 (mm/s)	Hindered settling	Velocity component	Hindered settling	Velocity component	Hindered settling	Velocity component	Hindered settling	Velocity component
0-0,25	0.125	15	8.26E-05	8.52E-06	7.03E-10	0.139486369	9.80654E-11	-0.71246	-5.0089E-10	-2.3908356	-1.7E-09	-5.64688	-4E-09
0,25-0,5	0.375	43	0.00639	7.66E-05	4.9E-07	0.899951256	4.40744E-07	0.800871	3.9222E-07	0.6055956	2.97E-07	0.226433	1.11E-07
0,5-0,75	0.625	34	0.023392	0.000213	4.98E-06	0.960788447	4.78464E-06	0.921938	4.59117E-06	0.845310096	4.21E-06	0.696297	3.47E-06
0,75-1	0.875	15	0.028318	0.000417	1.18E-05	0.977549714	1.15508E-05	0.955293	1.12878E-05	0.911353886	1.08E-05	0.82575	9.76E-06
1-1,25	1.125	6	0.024074	0.00069	1.66E-05	0.984447355	1.63474E-05	0.969019	1.60912E-05	0.938532401	1.56E-05	0.879022	1.46E-05
1,25-1,5	1.375	5	0.036629	0.00103	3.77E-05	0.987938929	3.72869E-05	0.975967	3.68351E-05	0.95229012	3.59E-05	0.905989	3.42E-05
1,5-1,75	1.625	4	0.048369	0.001439	6.96E-05	0.989947101	6.89099E-05	0.979963	6.82149E-05	0.960202843	6.68E-05	0.921499	6.41E-05
1,75-2	1.875	3	0.055728	0.001916	0.000107	0.991207043	0.000105836	0.982471	0.000104903	0.965167345	0.000103	0.931229	9.94E-05
2-2,25	2.125	1	0.027041	0.002461	6.65E-05	0.99204908	6.60192E-05	0.984146	6.54933E-05	0.968485192	6.45E-05	0.937733	6.24E-05
2,25-2,5	2.375	1	0.037752	0.003074	0.000116	0.992639497	0.0001152	0.985321	0.000114351	0.970811592	0.000113	0.942293	0.000109
2,5-2,75	2.625	1	0.050972	0.003755	0.000191	0.993069406	0.000190094	0.986177	0.000188775	0.972505543	0.000186	0.945613	0.000181
2,75-3	2.875	1	0.066967	0.004505	0.000302	0.993392121	0.000299676	0.986819	0.000297694	0.973777128	0.000294	0.948106	0.000286
3-3,25	3.125	1	0.086	0.005322	0.000458	0.99364053	0.000454802	0.987313	0.000451906	0.974755924	0.000446	0.950024	0.000435
3,25-3,5	3.375	1	0.108335	0.006208	0.000673	0.99383581	0.000668384	0.987702	0.000664259	0.975525378	0.000656	0.951532	0.00064
3,75-4	3.875	1	0.163969	0.008184	0.001342	0.994119125	0.00133395	0.988266	0.001326096	0.976641712	0.00131	0.95372	0.00128
4,25-4,5	4.375	1	0.235983	0.010432	0.002462	0.994310981	0.002447683	0.988648	0.002433741	0.977397676	0.002406	0.955202	0.002351
					<v> = 0.005857		<v> = 0.005820965		<v> = 0.00578463		<v> = 0.005713		<v> = 0.00557

Table F.3: Anode Milled 10 min.

						Volume fraction							
						0.125%		0.25%		0.5%		1.0%	
Size ranges (μm)	Average size (μm)	Frequency	Stokes' velocity (mm/s)	ϕ_i	Velocity_0 (mm/s)	Hindered settling	Velocity component	Hindered settling	Velocity component	Hindered settling	Velocity component	Hindered settling	Velocity component
0-0,25	0.125	15	8.26E-05	8.52E-06	7.03E-10	0.139486369	9.80654E-11	-0.71246	-5.0089E-10	-2.3908356	-1.7E-09	-5.64688	-4E-09
0,25-0,5	0.375	43	0.00639	7.66E-05	4.9E-07	0.899951256	4.40744E-07	0.800871	3.9222E-07	0.6055956	2.97E-07	0.226433	1.11E-07
0,5-0,75	0.625	34	0.023392	0.000213	4.98E-06	0.960788447	4.78464E-06	0.921938	4.59117E-06	0.845310096	4.21E-06	0.696297	3.47E-06
0,75-1	0.875	15	0.028318	0.000417	1.18E-05	0.977549714	1.15508E-05	0.955293	1.12878E-05	0.911353886	1.08E-05	0.82575	9.76E-06
1-1,25	1.125	6	0.024074	0.00069	1.66E-05	0.984447355	1.63474E-05	0.969019	1.60912E-05	0.938532401	1.56E-05	0.879022	1.46E-05
1,25-1,5	1.375	5	0.036629	0.00103	3.77E-05	0.987938929	3.72869E-05	0.975967	3.68351E-05	0.95229012	3.59E-05	0.905989	3.42E-05
1,5-1,75	1.625	4	0.048369	0.001439	6.96E-05	0.989947101	6.89099E-05	0.979963	6.82149E-05	0.960202843	6.68E-05	0.921499	6.41E-05
1,75-2	1.875	3	0.055728	0.001916	0.000107	0.991207043	0.000105836	0.982471	0.000104903	0.965167345	0.000103	0.931229	9.94E-05
2-2,25	2.125	1	0.027041	0.002461	6.65E-05	0.99204908	6.60192E-05	0.984146	6.54933E-05	0.968485192	6.45E-05	0.937733	6.24E-05
2,25-2,5	2.375	1	0.037752	0.003074	0.000116	0.992639497	0.0001152	0.985321	0.000114351	0.970811592	0.000113	0.942293	0.000109
2,5-2,75	2.625	1	0.050972	0.003755	0.000191	0.993069406	0.000190094	0.986177	0.000188775	0.972505543	0.000186	0.945613	0.000181
2,75-3	2.875	1	0.066967	0.004505	0.000302	0.993392121	0.000299676	0.986819	0.000297694	0.973777128	0.000294	0.948106	0.000286
3-3,25	3.125	1	0.086	0.005322	0.000458	0.99364053	0.000454802	0.987313	0.000451906	0.974755924	0.000446	0.950024	0.000435
3,25-3,5	3.375	1	0.108335	0.006208	0.000673	0.99383581	0.000668384	0.987702	0.000664259	0.975525378	0.000656	0.951532	0.00064
3,75-4	3.875	1	0.163969	0.008184	0.001342	0.994119125	0.00133395	0.988266	0.001326096	0.976641712	0.00131	0.95372	0.00128
4,25-4,5	4.375	1	0.235983	0.010432	0.002462	0.994310981	0.002447683	0.988648	0.002433741	0.977397676	0.002406	0.955202	0.002351
					<v> = 0.005857		<v> = 0.005820965		<v> = 0.00578463		<v> = 0.005713		<v> = 0.00557

Table F.4: Anode Milled 30 min.

						Volume fraction							
						0.125%		0.25%		0.5%		1.0%	
Size ranges (μm)	Average size (μm)	Frequency	Stokes' velocity (mm/s)	ϕ_i	Velocity_0 (mm/s)	Hindered settling	Velocity component	Hindered settling	Velocity component	Hindered settling	Velocity component	Hindered settling	Velocity component
0-0.25	0.125	15	8.48E-05	8.52E-06	7.22E-10	0.360212	2.6E-10	-0.27321	-1.9719E-10	-1.52112037	-1.1E-09	-3.942145564	-2.84527E-09
0.25-0.5	0.375	63	0.009611	7.66E-05	7.37E-07	0.924476	6.81E-07	0.849676	6.25893E-07	0.702230627	5.17E-07	0.415846946	3.06323E-07
0.5-0.75	0.625	14	0.009888	0.000213	2.11E-06	0.969617	2.04E-06	0.939507	1.97778E-06	0.880098706	1.85E-06	0.764486347	1.60934E-06
0.75-1	0.875	9	0.017443	0.000417	7.28E-06	0.982054	7.15E-06	0.964257	7.01819E-06	0.929103177	6.76E-06	0.86054006	6.2633E-06
1-1.25	1.125	4	0.016477	0.00069	1.14E-05	0.987172	1.12E-05	0.974442	1.10746E-05	0.949269626	1.08E-05	0.900068336	1.02293E-05
1.25-1.5	1.375	4	0.030083	0.00103	3.1E-05	0.989763	3.07E-05	0.979597	3.03648E-05	0.959477849	2.97E-05	0.920077485	2.85199E-05
1.5-1.75	1.625	4	0.049656	0.001439	7.15E-05	0.991253	7.08E-05	0.982563	7.02161E-05	0.965349087	6.9E-05	0.931585705	6.65732E-05
1.75-2	1.875	3	0.057211	0.001916	0.00011	0.992188	0.000109	0.984423	0.000107909	0.969032746	0.000106	0.938806047	0.000102909
2-2.25	2.125	3	0.083282	0.002461	0.000205	0.992813	0.000203	0.985666	0.000202021	0.971494588	0.000199	0.943631506	0.000193405
2.25-2.5	2.375	3	0.116269	0.003074	0.000357	0.993251	0.000355	0.986538	0.000352617	0.973220775	0.000348	0.947015008	0.00033849
2.5-2.75	2.625	2	0.104658	0.003755	0.000393	0.99357	0.000391	0.987173	0.000387989	0.974477687	0.000383	0.949478682	0.000373174
2.75-3	2.875	2	0.137498	0.004505	0.000619	0.993809	0.000616	0.987649	0.000611747	0.975421202	0.000604	0.951328068	0.000589249
3-3.25	3.125	1	0.088288	0.005322	0.00047	0.993994	0.000467	0.988016	0.000464263	0.976147469	0.000459	0.952751623	0.000447692
3.25-3.5	3.375	1	0.111218	0.006208	0.00069	0.994139	0.000686	0.988305	0.000682353	0.976718403	0.000674	0.953870713	0.000658579
3.75-4	3.875	1	0.168333	0.008184	0.001378	0.994349	0.00137	0.988723	0.001362018	0.977546722	0.001347	0.955494302	0.001316244
					<v> = 0.004346		<v> = 0.004319		<v> = 0.004292193		<v> = 0.004239		<v> = 0.004133241

Table F.5: Cathode Unmilled

						Volume fraction							
						0.056%		0.112%		0.224%		0.451%	
Size ranges (μm)	Average size (μm)	Frequency	Stokes' velocity (mm/s)	ϕ_i	Velocity_0 (mm/s)	Hindered settling	Velocity component	Hindered settling	Velocity component	Hindered settling	Velocity component	Hindered settling	Velocity component
1-1.5	1.25	1	0.000851563	3.15E-05	2.6808E-08	0.92324223	2.47504E-08	0.846822	2.27017E-08	0.694991	1.86314E-08	0.391364	1.04917E-08
1.5-2	1.75	1	0.001669063	8.64E-05	1.4418E-07	0.959741651	1.38376E-07	0.919657	1.32597E-07	0.840009	1.21113E-07	0.680695	9.81429E-08
2-2.5	2.25	5	0.002759063	0.000918	2.5328E-06	0.974761989	2.46886E-06	0.949631	2.40521E-06	0.899688	2.27872E-06	0.799761	2.02562E-06
2.5-3	2.75	3	0.004121563	0.001006	4.1448E-06	0.982365259	4.07168E-06	0.964803	3.99889E-06	0.929897	3.85421E-06	0.860033	3.56464E-06
3-3.5	3.25	7	0.005756563	0.003873	2.2296E-05	0.986738264	2.20005E-05	0.97353	2.1706E-05	0.947271	2.11205E-05	0.894697	1.99483E-05
3.5-4	3.75	7	0.007664063	0.00595	4.5601E-05	0.98948192	4.51209E-05	0.979005	4.46432E-05	0.958172	4.36932E-05	0.916446	4.17905E-05
4-4.5	4.25	9	0.009844063	0.011136	0.00010962	0.991315544	0.000108671	0.982664	0.000107723	0.965458	0.000105837	0.930982	0.000102057
4.5-5	4.75	6	0.012296563	0.010365	0.00012745	0.99260124	0.000126506	0.985229	0.000125566	0.970566	0.000123697	0.941173	0.000119951
5-5.5	5.25	6	0.015021563	0.013994	0.00021021	0.993537411	0.000208856	0.987098	0.000207503	0.974286	0.000204809	0.948594	0.000199409
5.5-6	5.75	1	0.018019063	0.003064	5.5215E-05	0.994240158	5.48967E-05	0.9885	5.45798E-05	0.977078	5.39491E-05	0.954165	5.2684E-05
6-6.5	6.25	9	0.021289063	0.035416	0.00075398	0.994781095	0.000750043	0.989579	0.000746121	0.979227	0.000738315	0.958453	0.000722652
6.5-7	6.75	3	0.024831563	0.014871	0.00036928	0.995206337	0.00036751	0.990428	0.000365745	0.980916	0.000362233	0.961824	0.000355182
7-7.5	7.25	8	0.028646563	0.049139	0.00140765	0.995546671	0.001401385	0.991107	0.001395136	0.982269	0.001382694	0.964522	0.001357713
7.5-8	7.75	6	0.032734063	0.045017	0.00147359	0.995823284	0.001467432	0.991659	0.001461295	0.983368	0.001449077	0.966714	0.001424537
8-8.5	8.25	7	0.037094063	0.063355	0.00235009	0.996051145	0.002340805	0.992114	0.002331552	0.984273	0.002313126	0.968521	0.002276106
8.5-9	8.75	6	0.041726563	0.064788	0.00270338	0.996241072	0.00269322	0.992493	0.002683087	0.985028	0.002662906	0.970026	0.002622351
9-9.5	9.25	3	0.046631563	0.038271	0.00178462	0.99640104	0.001778197	0.992812	0.001771792	0.985663	0.001759034	0.971294	0.001733391
9.5-10	9.75	2	0.051809063	0.029879	0.00154799	0.996537035	0.001542632	0.993083	0.001537286	0.986204	0.001526636	0.972372	0.001505225
10.5-11	10.75	2	0.062981563	0.040047	0.00252225	0.996754314	0.002514064	0.993517	0.002505898	0.987067	0.00248963	0.974095	0.002456911
11-11.5	11.25	4	0.068976563	0.091799	0.00633196	0.996841885	0.006311967	0.993692	0.00629202	0.987415	0.006252275	0.974789	0.006172328
11.5-12	11.75	3	0.075244063	0.078443	0.00590237	0.996918517	0.005884182	0.993845	0.005866039	0.987719	0.005829884	0.975396	0.00575715
13-13.5	13.25	1	0.095681563	0.037494	0.00358753	0.997098659	0.003577119	0.994204	0.003566734	0.988435	0.003546038	0.976824	0.003504384
14.5-15	14.75	1	0.118571563	0.051724	0.00613304	0.997226692	0.006116033	0.99446	0.006099062	0.988944	0.006065233	0.977839	0.005997129
21-21.5	21.25	2	0.246101563	0.309333	0.07612732	0.997504027	0.075937305	0.995013	0.075747667	0.990046	0.075369512	0.980038	0.074607638
					<v> = 0.1135723		<v> = 0.113254649		<v> = 0.112937714		<v> = 0.112305972		<v> = 0.111034237

Table F.6: Cathode Milled 5 min.

						Volume fraction							
						0.056%		0.112%		0.224%		0.451%	
Size ranges (μm)	Average size (μm)	Frequency	Stokes' velocity (mm/s)	ϕ_i	Velocity_0 (mm/s)	Hindered settling	Velocity component	Hindered settling	Velocity component	Hindered settling	Velocity component	Hindered settling	Velocity component
0-0.25	0.125	31	2.98047E-05	6.39855E-05	1.90707E-09	0.71862932	1.37048E-09	0.438512563	8.36274E-10	-0.11797	-2.2498E-10	-1.2306	-2.34685E-09
0.25-0.5	0.375	21	0.000268242	0.001170316	3.13928E-07	0.966747152	3.03489E-07	0.93363697	2.93095E-07	0.867843	2.7244E-07	0.736228	2.31123E-07
0.5-0.75	0.625	14	0.000745117	0.003612087	2.69143E-06	0.986596578	2.65535E-06	0.973246922	2.61942E-06	0.946708	2.548E-06	0.893574	2.40499E-06
0.75-1	0.875	11	0.00146043	0.007787659	1.13733E-05	0.992065298	1.12831E-05	0.984159869	1.11932E-05	0.968437	1.10143E-05	0.936925	1.0656E-05
1-1.25	1.125	8	0.00241418	0.012037538	2.90608E-05	0.9943158	2.88956E-05	0.988650793	2.8731E-05	0.977378	2.84034E-05	0.954765	2.77462E-05
1.25-1.5	1.375	7	0.003606367	0.019230751	6.93531E-05	0.995455	6.90379E-05	0.990924091	6.87237E-05	0.981904	6.80982E-05	0.963795	6.68422E-05
1.5-1.75	1.625	5	0.005036992	0.022673586	0.000114207	0.996110209	0.000113762	0.992231574	0.000113319	0.984508	0.000112437	0.968989	0.000110665
1.75-2	1.875	5	0.006706055	0.034830838	0.000233578	0.996521292	0.000232765	0.993051899	0.000231955	0.986141	0.00023034	0.972248	0.000227095
2-2.25	2.125	5	0.008613555	0.05070338	0.000436736	0.996796024	0.000435337	0.993600133	0.000433941	0.987233	0.00043116	0.974425	0.000425567
2.25-2.5	2.375	3	0.010759492	0.04247195	0.000456977	0.996988661	0.000455601	0.993984543	0.000454228	0.987998	0.000451492	0.975952	0.000445987
2.5-2.75	2.625	5	0.013143867	0.09557582	0.001256236	0.997128927	0.001252629	0.994264448	0.001249031	0.988555	0.001241859	0.977064	0.001227423
2.75-3	2.875	6	0.01576668	0.150679754	0.002375719	0.99723422	0.002369149	0.994474562	0.002362593	0.988974	0.002349524	0.977899	0.002323213
3-3.25	3.125	6	0.01862793	0.193504656	0.003604591	0.997315269	0.003594914	0.994636297	0.003585257	0.989296	0.003566006	0.978541	0.003527242
3.25-3.5	3.375	9	0.021727617	0.365640206	0.00794449	0.997378983	0.007923668	0.99476344	0.007902889	0.989549	0.00786146	0.979046	0.007778025
					<v> = 0.016535328		<v> = 0.016490001		<v> = 0.016444773		<v> = 0.016354615		<v> = 0.016173096

Table F.7: Cathode Milled 10 min.

						Volume fraction							
						0.056%		0.112%		0.224%		0.451%	
Size ranges (μm)	Average size (μm)	Frequency	Stokes' velocity (mm/s)	ϕ_i	Velocity_0 (mm/s)	Hindered settling	Velocity component	Hindered settling	Velocity component	Hindered settling	Velocity component	Hindered settling	Velocity component
0-0,25	0.125	38	2.98047E-05	0.01309848	3.90396E-07	0.888303123	3.4679E-07	0.7771	3.03377E-07	0.556171516	2.17E-07	0.114401393	4.47E-08
0,25-0,5	0.375	41	0.000268242	0.03815794	1.02356E-05	0.985599797	1.00882E-05	0.971258	9.94138E-06	0.942748	9.65E-06	0.885672754	9.07E-06
0,5-0,75	0.625	32	0.000745117	0.137878736	0.000102736	0.993383531	0.000102056	0.98679	0.000101379	0.973674119	0.0001	0.947374463	9.73E-05
0,75-1	0.875	8	0.00146043	0.094584813	0.000138134	0.995528029	0.000137517	0.99107	0.000136901	0.98219458	0.000136	0.964373913	0.000133
1-1,25	1.125	8	0.00241418	0.201027197	0.000485316	0.996410538	0.000483574	0.992831	0.000481836	0.985700943	0.000478	0.971369572	0.000471
1,25-1,5	1.375	4	0.003606367	0.045879149	0.000165457	0.996857263	0.000164937	0.993722	0.000164418	0.987475858	0.000163	0.974910763	0.000161
1,5-1,75	1.625	3	0.005036992	0.151459791	0.000762902	0.997114196	0.0007607	0.994235	0.000758504	0.988496696	0.000754	0.976947471	0.000745
1,75-2	1.875	1	0.006706055	0.116335183	0.00078015	0.997275398	0.000778025	0.994557	0.000775904	0.989137178	0.000772	0.978225317	0.000763
					<v> = 0.002445321		<v> = 0.002437243		<v> = 0.002429186		<v> = 0.002413		<v> = 0.002381

Table F.8: Cathode Milled 30 min.

						Volume fraction							
						0.056%		0.112%		0.224%		0.451%	
Size ranges (μm)	Average size (μm)	Frequency	Stokes' velocity (mm/s)	ϕ_i	Velocity_0 (mm/s)	Hindered settling	Velocity component	Hindered settling	Velocity component	Hindered settling	Velocity component	Hindered settling	Velocity component
0-0.25	0.125	60	1.28E-05	0.005841	7.46039E-08	0.820338606	6.12E-08	0.641475604	4.78566E-08	0.286136752	2.13E-08	-0.42435378	-3.1658E-08
0.25-0.5	0.375	21	0.000115	0.055193	6.34506E-06	0.978048184	6.21E-06	0.956188419	6.06708E-06	0.912744137	5.79E-06	0.825811068	5.23982E-06
0.5-0.75	0.625	24	0.000319	0.292028	9.32549E-05	0.99066495	9.24E-05	0.981365444	9.15172E-05	0.962872728	8.98E-05	0.925824256	8.63377E-05
0.75-1	0.875	13	0.000626	0.43405	0.000271671	0.994140998	0.00027	0.988301971	0.000268493	0.976683667	0.000265	0.95337891	0.000259006
1-1.25	1.125	3	0.001035	0.212888	0.000220264	0.99557147	0.000219	0.991156509	0.000218316	0.98236718	0.000216	0.964718273	0.000212493
					<v> = 0.00059161		<v> = 0.000588		<v> = 0.000584442		<v> = 0.000577		<v> = 0.000563045

G

Mass balance LFP-Graphite

Figure G.1 shows the mass balance of the LFP-Graphite sediment that is analysed by ICP-OES and TGA analysis in section 4.5. Figure G.2 shows the corresponding ICP-OES measurements with the standard deviations of the summed Li, Fe, and PO4 content over the two reproduced experiments.

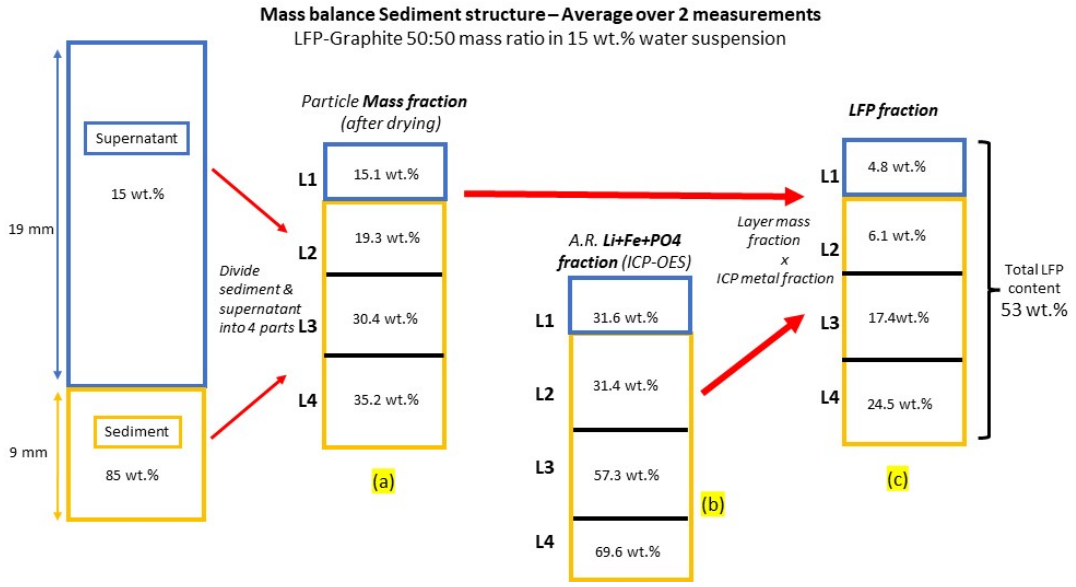

Figure G.1: LFP-Graphite mass balance sediment mixture after sedimentation: the frozen suspension is divided into 4 parts. After drying, the samples are weighed. Their mass fractions are given in Column (a). These layers are characterised by ICP-OES analysis. The measured sum of metallic compounds attributable to cathode material is given in Column (b). Multiplying (a) and (b) for each layer gives the metal fractions in the frozen suspension in Column (c). The sum of these is the total metal fraction in the suspension, which corresponds to half the LFP mass, considering the 50:50 Graphite/LFP mass ratio.

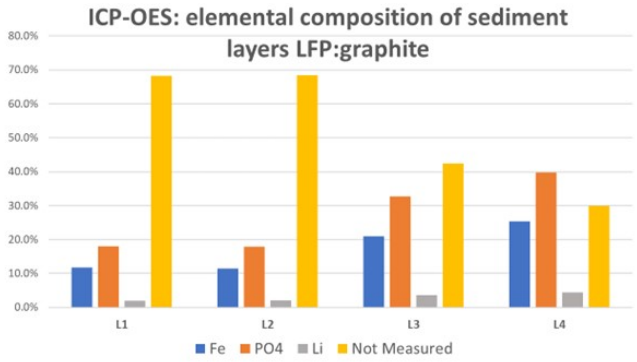

(a)

Li + Fe + PO4 Mass fractions: Average and Deviation		
Layer	Average Value (wt.%)	Standard Deviation (wt.%)
1	31.6%	6.7%
2	31.4%	3.2%
3	57.3%	7.4%
4	69.6%	3.3%

(b)

Figure G.2: ICP-OES results LFP-Graphite

H

Preliminary results

This chapter introduces an estimation for the sedimentation of typical LIB particles made as a preliminary study after the literature.

An analysis is done for the size ratios of anode and cathode material where separation is possible, using the sedimentation principle.

H.1. Model size ratios for effective separation

Combining the sedimentation theory and the found data of the different grains from lithium-ion batteries, a model can be made to indicate whether effective separation of the anode and cathode material by sedimentation is possible.

In this model, we will assume particles falling in a tank of a certain length containing water. Because we know the settling velocities of different grain types, we can determine the time it takes to travel a certain distance L and, when taking two species, the relative distance between them, as one travels faster than the other. From here, we want to know for which size ratio of two particle species, separation is possible.

For simplicity, we state that:

Separation is possible if the minimum distance between the two particles is half of the length of the tank, after the fastest settling particle has reached the bottom.

We can write the mathematical expression as: 'Effective' Separation is possible when:

$$x = |v_1 - v_2| t_{\text{max}} \geq \frac{1}{2} L \tag{H.1}$$

x is the relative distance after settling of the fastest particle. v_1 and v_2 are the settling velocities of the two different species. t_{max} is the time the fastest settling particle takes to 'settle'. As we stated that settling means reaching the bottom and the distance is length L, we can generally say:

$$t_{\text{max}} = \frac{L}{\text{max}(v_1, v_2)} \tag{H.2}$$

We use equation H.1 as saying that effective separation is possible, if not: separation is not possible, meaning: $x \leq \frac{1}{2} L$. As the size of the particles is hidden in the Stokes equation for the settling velocities, we can check for different grain sizes of the particles if separation is possible, according to our statement of effective separation. As there are different sedimentation models introduced with different expressions for the settling velocity, the statement is reviewed for the different models. The two particle species are anode and cathode material, as we want to separate them.

Two particles of anode and cathode material are used to calculate their settling velocity for varying particle size to indicate the size ratios of the two particle classes where effective separation is possible. As an example, we take graphite as anode material and $LiCoO_2$ (LCO) as cathode material, what we would like to separate. Firstly, the individual particle Stokes velocity is used for the statement, then the Richardson-Zaki expression is used for varying particle volume fractions, and lastly a combination of Richardson-Zaki and MLB is reviewed.

1. Size ratios: Stokes Single particle Firstly, the statement of effective separation (H.1) is examined for two individual particles with the Stokes velocity modeled as the settling velocities of both particles, according to equation 1.1. By varying the particle sizes between 0 and 30 μm for both species, we evaluate the separation statement for the sizes. Figure H.1 is obtained and three different areas can be observed in the plot, which are separated by linear lines starting at the origin. The three areas correspond to three possible outcomes of the sedimentation process.

- Area I: Effective separation is possible and the graphite particle is the fastest settling particle
- Area II: Effective separation is not possible, the settling rates of the particles are too close to each other
- Area III: Effective separation is possible and the cathode particle is the fastest settling particle

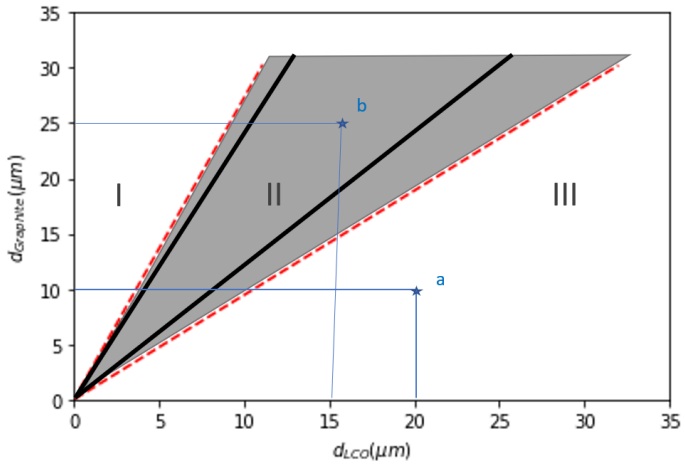

Figure H.1: Plot where the particle size of graphite and LCO are varied on the x- and y-axis respectively. The dark lines correspond to the average particles: meaning the average density of the grains, while the red ones correspond to the extreme values of the maximum and minimum densities of the grains. These lines create different areas, that can be interpreted as different sedimentation behavior. Area I and III correspond to combinations of grain sizes where separation is possible. Area II, dark coloured, shows the grain sizes where separation is not possible.

From here the size ratios of the two particle species can easily be determined. For example, dotted as points in Figure H.1, point a corresponds to grains LCO and graphite with a size of $d_{\text{LCO}} = 20\mu m$ and $d_{\text{graphite}} = 10\mu m$, so a size ratio of $d_{\text{graphite}}/d_{\text{LCO}} = 0.5$. Point a is located in area III, so effective separation is possible. Thus we can say, for all combinations of particles with a size ratio of 0.5, effective separation is possible. In a similar way, these linear lines of size ratios are located either between the red lines (area II), or outside (area I and III).

Point b corresponds to two different grain sizes, having a size ratio of $d_{\text{graphite}}/d_{\text{LCO}} = 1.7$. This point is located in area II, so it can be concluded that for all size combinations with a size ratio of 1.7, effective separation is not possible.

2. Size Ratios: Richardson and Zaki In practical applications, the sedimentation of just two particles with sizes in the order of a few microns is not typically encountered. Therefore, it is more interesting to explore different volume fractions of particle suspensions and examine how the size ratios at which sedimentation occurs depend on the volume fraction. The Richardson-Zaki correlation can be employed for monodisperse and slightly polydisperse systems, utilizing the hindered settling function as defined in Equation 1.4. To utilize this correlation for the settling velocity of two distinct particles, we must consider the distinct regions that arise within a polydisperse suspension, as introduced in subsection 1.2.5. For simplicity, we take for both particle volume fractions the same value, so $\phi_1 = \phi_2$. In this system, the two settling fronts can be modeled with their respective settling rates, owing to the variation in volume fraction.

Figure 1.7a provides an illustration of these regions. If particle 1 is the faster settling particle and particle 2 the slower one, the settling rates are modeled according to the regions in the suspension:

- Region 1 corresponds to the polydisperse region, where ϕ represents the total volume fraction of both graphite and LCO particles. The Settling velocity for front a is then: $v_1 = v_{1,0}(1-\phi)^n$, with $v_{1,0}$ as the single Stokes velocity of particle 1 and ϕ as the total particle volume fraction of the mixture.
- Region 2 corresponds to the monodisperse region, where ϕ represents solely the volume fraction of the lighter and smaller particles, so $\phi/2$. The settling velocity for front b is then: $v_2 = v_{2,0}(1-\phi/2)^n$, with $v_{2,0}$ as the single Stokes velocity of particle 2 and $\phi/2$ as the particle volume fraction of particle 2 only.

To model the size ratios and examine where sedimentation is possible, these two regions can be used as the two settling fronts with their settling velocity, corresponding to the faster settling particles and slower ones.

We examine for a total particle volume fraction from $\phi = 0$ until $\phi = 0.2$, due to the fact that R-Z is not usable for too dense polydisperse particle suspensions. Similar to Figure H.1, the grain sizes are varied from 0 to 30 μm, and now the different coloured lines correspond to the different volume fractions.

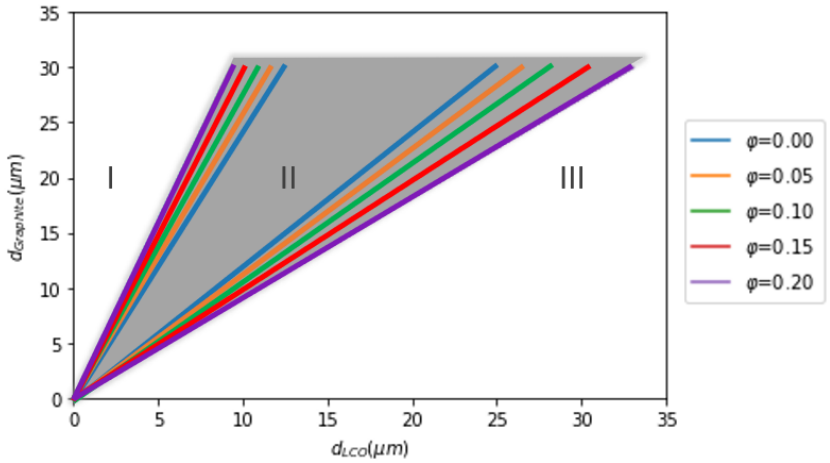

Figure H.2: where the particle size of graphite and LCO are varied on the x- and y-axis respectively for different particle volume fractions (ϕ), according to the Richardson-Zaki correlation. Three areas are observed. Area I and II correspond to grain sizes where separation is possible. The darker coloured area II correspond to no separation possible. This area increases for increasing particle volume fraction.

As can be seen in figure H.2, the blue lines corresponds to a particle volume fraction $\phi = 0$ (= $\phi_f = 1$) and these are the same lines as the black lines in figure H.1, as these correspond to the Stokes' single particle velocities. As can be seen, the area where effective separation is not possible (area II), expands for increasing particle volume fraction, so less size ratios of the grains are usable for separation as the suspension becomes denser.

The interaction between multiple particles and fluid seems to have a big impact on the sedimentation process. A bad assumption in this model is that the Richardson-Zaki is used for calculating the bidispersed mixture of region 1, therefore the MLB is a possible better approximation for higher volume fractions.

3. Size Ratios: R-Z and MLB Lastly, the MLB model can be applied for the sedimentation process in a tank of water. As explained, this model can be applied for more dense polydispersed suspensions, so using this approach for the lower front at region 1 in the system should be more logical, as seen in figure 1.7a. For the two settling velocities of components 1 and 2, they are now modeled as:

- The Settling velocity for front 1 is chosen as the velocity of the fastest settling particle 1 from equation 1.8, as the region 1 is a bidispersed mixture.
- The settling velocity for front 2 is: $v_2 = v_{2,0}(1-\phi/2)^n$, with $v_{2,0}$ as the single Stokes velocity of particle 2, as region 2 is monodispersed, only consisting of lighter, slower settling particles.

We examine for a total particle volume fraction from $\phi = 0$ until $\phi = 0.4$ for a very packed suspension, as the MLB equation can also be used for more dense, bidispersed suspensions.

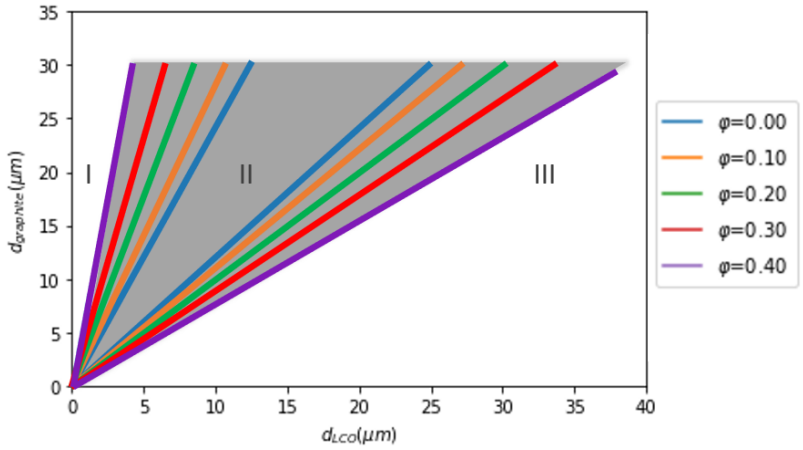

Figure H.3: Plot where the particle size of graphite and LCO are varied on the x- and y-axis respectively for different particle volume fractions (ϕ), according to the Richardson-Zaki and MLB correlation. Three areas are observed. Area I and II correspond to grain sizes where separation is possible. The darker coloured area II correspond to no separation possible. This area increases for increasing particle volume fraction.

Again, the three areas are visible, and now area II expands even more, as the particle volume fraction is now increased up to $\phi = 0.4$. Similar to figure H.2, the size ratios for which no separation is possible increases with the particle volume fraction.

Size ratios for effective separation For the three different models that were applied to a sedimentation tank for graphite and LCO particles, we could get a size diagram showing the areas where separation is possible and not possible.

	Size ratios $d_{\text{graphite}}/d_{\text{LCO}}$		
Particle volume fraction ϕ	1. Stokes	2. R-Z	3. R-Z/MLB
0.00	$\leq 1.21, \geq 2.41$	$\leq 1.21, \geq 2.41$	$\leq 1.21, \geq 2.41$
0.05	-	$\leq 1.06, \geq 2.57$	$\leq 1.15, \geq 2.62$
0.10	-	$\leq 0.92, \geq 2.75$	$\leq 1.10, \geq 2.85$
0.15	-	$\leq 0.79, \geq 2.95$	$\leq 1.05, \geq 3.15$
0.20	-	$\leq 0.67, \geq 3.19$	$\leq 1.00, \geq 3.51$
0.30	-	-	$\leq 0.94, \geq 4.62$
0.40	-	-	$\leq 0.78, \geq 7.05$

Table H.1: Size ratios graphite and LCO particles for which separation is possible. For the three applied models. Models 2 and 3, where the volume fraction of the suspension is considered, show that the range of size ratios where separation is possible gets smaller for higher volume fractions.

In Table H.1, the size ratios for which separation is possible according to the applied model are arranged per particle volume fraction. These are the size ratios that exclude Area II in the ratio diagrams (figure H.1, H.2 and H.3). The columns from left to right present the three introduced models: using the single Stokes' velocity, Richardson-Zaki for both regions and a combination of R-Z and MLB for the different regions.